UCLA
UCLA Electronic Theses and Dissertations

Title
Laser-Generated Shockwaves for the Disruption of Bacterial Biofilms

Permalink
https://escholarship.org/uc/item/86w3017k

Author
Navarro, Artemio

Publication Date
2013

Peer reviewed|Thesis/dissertation

UNIVERSITY OF CALIFORNIA

Los Angeles

Laser-Generated Shockwaves
for the Disruption of Bacterial Biofilms

A dissertation submitted in partial satisfaction

of the requirements for the degree

Doctor of Philosophy in Mechanical Engineering

by

Artemio Navarro

2013

<div align="center">

Abstract of the Dissertation

Laser-Generated Shockwaves
for the Disruption of Bacterial Biofilms

by

Artemio Navarro

Doctor of Philosophy in Mechanical Engineering

University of California, Los Angeles, 2013

Professor Vijay Gupta, Chair

</div>

The goal of this thesis was to explore the use of laser-generated shockwaves as a potential methodology to treat bacterial infected surfaces as they are a major burden on the healthcare industry. A modified version of the Laser Spallation Technique (LST) was built to measure the intrinsic adhesion strength of *S. epidermidis* biofilms (*RP62A*) grown on polystyrene surfaces. Previously, the LST was used to successfully measure the adhesion strengths of mammalian cells. The system is based on a Q-switched, Nd:YAG pulsed laser with an output wavelength of $1,064\ nm$ and a pulse width between $2-6\ ns$ that ablates titanium-coated soda-lime glass slides (under confinement), thereby causing unipolar compressive waves. The modified LST successfully measured the adhesion strength of *S. epidermidis* biofilms grown on polystyrene, under static growth conditions, to be $22.75 \pm 0.16\ MPa$. High strain rates of $1.544 \times 10^5\ s^{-1}$ and $1.41 \times 10^6\ s^{-1}$ in glass and in biofilm, respectively, were calculated, and total strains of $0.3\ \%$ in glass and $3\ \%$ in the *S. epidermidis* biofilm are reported and are below published failure strains. Current techniques that measure biofilm material properties vary significantly due to viscoelastic effects of biofilms under lower strain rates. Due to the high strain rates and only purely compressive/tensile loading, the adhesive failure in the biofilm is an intrinsic strength measurement.

With motivation to use these glass modified shockwaves on infected wounds, studies were implemented to evaluate the effect of the shockwaves on porcine samples ex vivo.

<div align="center">

ii

</div>

Due to the impedance mismatch of the glass slides with the coupling medium (water), a compressive train of shockwaves are created. Peak stresses varying from $21 - 266.5 \ MPa$ of the shockwave, with subsequent stress pulses with 18% less peak stress, reached the pigskin surface and caused no qualitative structural damage. This is a very important result as other studies have used similar stress profiles, as a single shockwave, to deliver drugs through the skin and biofilm structures.

Finally, a low-cost, high-speed imaging system was developed and characterized to capture shockwave-induced phenomenon, i.e. cavitation. Unlike other techniques including extracorporeal shockwave (ESW) therapy, which has a tensile component in the stress profile and thus causing cavitation-induced damage in biological structures, laser-generated shockwaves are purely compressive and will only have tensile components at interfaces, depending on the impedance of each layer. Cavitation bubbles were successfully imaged at the glass/water interface which propagated toward the biofilm and caused localized delaminations.

The dissertation of Artemio Navarro is approved.

Warren S. Grundfest

William S. Klug

Laurent G. Pilon

Zachary D. Taylor

Vijay Gupta, Committee Chair

University of California, Los Angeles

2013

Para mi familia...

Table of Contents

List of Figures

List of Tables

Vita

2002	California Academy of Mathematics and Science School
	Carson, California
2006	B.S. Mechanical Engineering,
	University of California, Berkeley
2009	M.S. Mechanical Engineering,
	University of California, Los Angeles

CHAPTER 1

Introduction

Bacteria have been extensively studied for many years as individual cells in a planktonic "free-flowing") state. Many of today's antibiotics in fact have been developed as the antibiotic was applied to these individual microbes in suspension [2]. However, these bacterial spores do not naturally grow in these nutrient-rich suspensions developed and studied in laboratories. In fact, bacteria tend to naturally grow and adhere to surfaces in a more sessile ("fixed") community of cells encased in self-produced exopolysaccharide matrix known as a biofilm [3,4]. The formation and growth of these bacterial communities allowed them to survive harsh environmental conditions and have had both positive and negative impacts toward humans [5]. In the medical field, biofilms have been found on medical implants, catheters and even wound surfaces, thereby increasing infections of patients and further increasing the costs of medical care [4]. In order to develop mechanical methods of understanding biofilm growth, biofilm properties must be properly measured and reported.

1.1 Motivation of Present Study

By measuring biofilm material properties, techniques could be developed to better understand biofilm development in nature. Certain material properties needed include: elastic modulus, tensile strength, shear strength, adhesive and cohesive failures strengths. To this date, there does not exist a technique that allows for the direct measurement of the adhesion strength of biofilms under tension. This is due to the fact that the biofilm will reach cohesive failure first. The use of the Laser Spallation Technique (LST) method, previously used to find the adhesion strength of thin-films, is explored to not only mea-

sure biofilm adhesion strengths, but the technique is also used as a potential therapeutic tool that can both deliver drugs and detach biofilms off surfaces.

Ultimately, the use of laser-generated shockwaves (LGS) are explored as a potential treatment modality for infected wounds. In this more realistic model, it is of critical importance to understand the effect mechanical effects of LGS on tissue. Thus it is imperative to locally target biofilm structures while preserving underlying healthy tissue.

1.2 Objectives of the Present Study

The aims of this study were:

1. Investigate the use of glass-modified shockwaves to disrupt biofilms in a "Top-Down" approach by using the Laser Spallation Technique to quantify adhesion strengths.

2. Determine damage thresholds of glass-modified shockwaves on porcine skin.

3. Investigate stress-wave induced phenonmenon in coupling medium (water) by developing a novel, low-cost highspeed imaging system.

1.3 Document Organization

Due to the multiple disciplines in this study, Chapter 2 will be dedicated to providing a better understanding of biofilms, their effects in medicine and to also present the modified Laser Spallation Technique used to quantify adhesion strengths of thin films. Chapter 3 will explore the use of glass-modified stress waves on bacterial biofilms grown on polymeric surfaces. Adhesion strength measurements will be provided. Chapter 4 will discuss the effect of the glass modified laser generated stress waves on porcine samples and establish damage thresholds. Then, Chapter 5 will present a novel, low-cost high speed imaging system to capture the shockwave induced phenomenon. Finally, Chapter 6 will conclude with results and recommendations.

CHAPTER 2

Background

2.1 Introduction

This chapter will provide the reader with general background needed to better understand the content presented in this thesis. Bacterial biofilms are described in greater detail, and how biofilms present a challenge to the health industry. To this end, treatment modalities used to rid of biofilms are presented. The remainder of the chapter will describe the Laser Spallation Technique (LST) and how it is used to both generate and measure stresses as it will ultimately be used as a measurement tool for biofilm adhesion strengths.

2.2 Bacterial Biofilms

Bacterial biofilms are complex organizations of microorganisms that adhere to surfaces or interfaces byway of a hydrated matrix or extracellular polymeric substance (EPS) that these cells secret [6]. Bacterial cells were normally studied under controlled *in vitro* models whereby the cells were allowed to grow in suspensions full with nutrient-rich media. These controlled experiments allowed for a better understanding of cell pathogenesis, leading to vaccines and antibiotics [2]. However, there is greater interest in cell studies in their natural environment. Biofilms have been found growing on medical implants, including catheters and implants, and tissue, thus leading to difficult to manage infections [4, 5, 7, 8]. They have also caused infections on human surfaces including teeth and urinary tracts [9, 10]. Moreover, biofilms were also found on metals and toxic chemicals [11]. Not all biofilms, however, are detrimental to society. In fact, biofilm growth is critical both in bioremediation and biological wastewater treatment systems [12].

The bacteria within the biofilm matrix have been shown to be less susceptible to antimicobrial compounds and host defenses [13,14]. The recalcitrant nature of bacteria is partly due to persister cells within the biofilm [15]. Antibiotics have shown no effect and these persister cells are non-dividing. The extracellular matrix that the bacteria secret act as a diffusion barrier to smaller molecules [6,14]. Also, the EPS is mostly composed of water that is tightly bound and protects cells from rapid dessication [16]. This physical barrier does not allow access of cells deeply embedded in the biofilm nutrients and vitamins, thus leading to metabolically inactive cells. This is similar to the stationary phase in bacterial in laboratory where cells grow reach and equilibrium state where the rate of cell division will be equal to cell death [5].

2.2.1 Structure and Formation

Bacterial biofilms are mainly composed of four components: (i) cells, (ii) exopolysaccharides, (iii) water and (iv) DNA, RNA. In fact, $95 - 99\%$ of the biofilm matrix is composed of mostly water and $2 - 5\%$ can be composed of DNA and RNA depending on environmental conditions [2,3,17]. Biofilms typically consist of less than 10% of dry mass by embedded microorganisms while more than 90% of the structure are biopolymers known as extracellular polymeric substances (EPS) [18]. These biopolymers act as scaffolds or three-dimensional support structures that protect against natural biocides, antibiotics, ultraviolet radiation, immune defences, protozoans, dessication, changes in pH [12]. They also serve as "anchors" whereby the EPS prevents biofilms from detaching due external shearing flows [4].

Biofilm formation occurs in four major stages: (i) Planktonic, (ii) Monolayer, (iii) Microcolonies, and (iv) Biofilm [19]. During the Planktonic ("free-flowing") stage, cells are either suspended in bulk fluid and transported to surfaces or interfaces. The second stage or "Monolayer" stage is achieved as the bacteria initially attach to surfaces by way of physiochemical interactions and must overcome natural forces at the atomic level. These opposing forces include electrostatic interactions, van der Waals forces and

hydrodynamic interactions. In fact, some cells like *E. coli* have developed flagella that allow them to traverse surfaces to reach more favorable conditions. The "Monolayer" stage is a reversible attachment and if the conditions favor the bacteria, they would then irreversibly attach and form the next stage. In the "Microcolonies" stage, cells are fixed and will continuously divide and secrete exopolysaccharides that will allow them to bind to each other thereby allowing cohesive attachment, and also allow them to adhere to the surface. Eventually, the cells will mature and form the fourth "Biofilm" stage. Here, cells will mature and develop 3-dimensional "mushroom-like" structures and will approach a saturation stage where the cell number of new replicated cells will equal the number the amount of dying cells. This is due to the limitation of nutrients. As result, cells that are deep within the biofilm structure become quiescent or no longer metabolically active. The cells that are closer to the outer boundaries of the biofilm structure genetically modify and disperse and are allowed to further colonize localized areas with more favorable conditions.

2.3   Biofilm Treatments in Medicine

Infected wounds due to trauma or surgery impose a major burden on the US healthcare system. Treatment of infected wounds, both surgical and traumatic, cause prolonged hospitalization, can lead to sepsis, and dramatically increase the cost of patient care. Approximately $750,000$ surgical site infections (SSI) occur every year in the United States and result in hospital expenses exceeding $1.6 billion and with 3.7 million extra days of hospital stay [20]. In fact, SSI affect 2 out of 100 of all patients undergoing surgical procedures and are a major cause of morbidity and expense in the surgical population [21]. One of the main mechanisms that enable bacteria to persist in vivo is through the generation of biofilms. Biofilms consist of a three-dimensional matrix layer rich with polymeric substances such as polysaccharides, nucleic acids, and proteins that provide a protective and nurturing environment for bacteria to proliferate and reside in [3, 22]. They allow the bacteria to mechanically adhere to the wound surface, thereby preventing ingress of white blood cells and antibodies. Biofilms also provide a chemical

barrier to antibiotics and help maintain nutritional/hydration levels. Bacteria present in mature biofilms are resistant to $50 - 5000$ times the concentrations of antimicrobial agents that are necessary to kill planktonic cells of the same organism [22, 23]. Several species of bacteria including genuses Staphylococcus and Acinetobacter, persist in traumatic wounds despite treatment with topical antibiotics, wound irrigation, and surgical debridement. Moreover these infections are becoming increasingly difficult to manage due to the emergence of bacterial strains that exhibit antibiotic resistance [24–30]. Normal wound healing is characterized by 3 overlapping phases: inflammatory, proliferative and remodeling. If the bodys vascular and cellular responses during the inflammatory phase are inadequate to overcome surface microorganisms, the wound becomes predisposed to infection, delaying angiogenesis, tissue granulation and reepithelialization in subsequent stages, making them chronic. Chronic Wounds are characterized by the formation of a coagulum, accumulation of necrotic debris and leaked protein-containing fluids that serve as a rich medium for bacterial growth. Several advances in wound care have resulted in the current synergistic approach to treat wounds with wound debridement coupled to negative-pressure wound dressings, high pressure irrigation and topical antibiotics [31–35]. However, debridement is often painful, time-consuming and must be repeated frequently, since bacterial proliferation resumes immediately after the procedure is finished. From this, one can conclude that successful infectious-wound management requires dislodging and/or destroying biofilm to make the bacteria more vulnerable and reduce bioburden to less than 105 organisms per gram of tissue for the normal healing process to continue [36]. Therefore, studying more effective biofilm disruption techniques holds a promising value in reducing the bacterial bio-burden, thereby limiting one of the major contributing factors in persistent wound infections.

2.3.1 Chemical Methods

Traditional treatments for wound management include systemic and topical antibiotics, surgical and enzymatic wound debridement, a variety of dressing formulations, and negative-pressure wound drainage systems.

Several classes of chemical compounds have shown promise in combating biofilms when used in conjunction with traditional antimicrobials. The vast majority of these compounds exert their anti-biofilm properties through disruption of quorum sensing signaling [37], a common means of intercellular communication in bacterial communities. Surface preparation of medical devices, sutures, fibers, catheters, and other implants with antimicrobials potentially could minimize initial microbial colonization. However, this method of biofilm prevention and therapy was not found to be successful in the long term [38, 39]. In vitro experiments performed by Oxley et al. [40] demonstrated that topical antibiotics did not eradicate bacteria due to the presence of a persistent biofilm. Bacteria in a biofilm are highly resistant to systemic antibiotics. One strategy for dealing with highly resistant bacteria is to use high doses of topical antibiotics. Desrosiers et al. [41] reported use of a topical antibiotic in a 1000-fold concentration producing a several log reduction of viable bacteria in *S. aureus* biofilms isolated from patients with chronic rhinosinusitis. In contrast, Chiu et al. [39] demonstrated the persistence of mucosal *Pseudomonas* biofilms even in the face of high concentrations of topical tobramycin in a rabbit model. Topical therapies have previously been recommended for some chronic infections such as sinusitis with varying success rates. A prospective, placebo-controlled trial of nebulized tobramycin for the treatment of chronic sinusitis refractory to medical and surgical therapy did not show any benefit of tobramycin over placebo [42]. Desrosiers et al. [43] demonstrated that pressurized irrigation and citric acid/zwitterionic surfactant was superior to either treatment alone for disruption of bacterial biofilms. While all these approaches have shown some promise, the clinical impact of these methods remains under investigation.

2.3.2 Negative-pressure wound therapy (NPWT)

Negative-pressure wound therapy is performed using vacuum through a special sealed dressing to promote healing in chronic wounds. The vacuum draws out interstitial fluid from the wound increasing blood inflow to the wound area and improving capillary circulation at the edges of the wound. The first study investigating the effects of NPWT

on the bacterial load showed a decrease in bacterial load around 4 to 5 days compared to control. Three studies thereafter reported opposite results. A retrospective clinical study by Weed et al. [44] in 26 wounds of varying etiology reported that bacterial colonization increased significantly with NPWT. In a randomized trial, Braakenburg et al. [45] reported swab cultures showing increased bacteriologic colonization in patients treated with NPWT (P=0.06). Finally in another randomized trial, Moues et al. [46] compared NPWT with conventional moist gauze therapy in 54 patients reporting no quantitative reduction in the number of bacteria between the two treatments. Although they did report a significant increase in *Staphylococcus aureus* and a significant decrease in gram-negative bacilli species in patients treated with NPWT. Nonetheless, NPWT has been shown successful in treating wounds when used in conjunction with debridement, high pressure irrigation and adjuvant antibiotics in pressure ulcers [35], infected median sternotomy wounds [31] and high energy soft tissue injuries [34]. However, none of the studies reported any bacteriologic sampling data. To summarize, there is no scientific evidence that proves that NPWT reduces bacterial load [47].

2.3.3 Mechanical Methods

Two approaches to mechanical disruption of biofilms have been explored. One uses low-intensity ultrasound at frequencies of $0.75 - 3\ MHz$, and the other uses stress wave pulses with sharper rise times and high in peak stress amplitudes to generate shockwaves.

2.3.3.1 Therapeutic Ultrasound

Therapeutic ultrasound techniques use power densities below $500\ mW/cm^2$ when calculated by averaging the beam power over its area and pulse repetition period, and $100\ mW/cm^2$ when averaged over the pulse duration time. Studies have shown that under these frequencies and intensities, ultrasound interacts with cell membranes through non-thermal effects, including cavitation and microstreaming [48]. Cavitation is the process by which air-bubbles expand and compress due to the pressure field caused by the acoustic waves. Microstreaming caused by pressure gradients is the process by which

fluids move along membranes. These mechanical effects have been shown to increase angiogenesis (new blood vessel formation), a process that is essential for wound healing [49]. Here, Young et al. showed that when two groups (one control) were exposed to ultrasound at frequencies of 0.75 MHz and 3.0 MHz for 5 min (pulsed 2 ms on and 8 ms off) a day at an intensity of 100 mW/cm^2, corresponding to a total energy flux of about 30 J/cm^2 per day or 150 J/cm^2 for the five-day period, they reported greater formation of new blood vessels within five days after application. Therapeutic Ultrasound has also been shown to be effective in new bone formation and treatment of diabetic foot ulcers [50, 51]. Such beneficial effects along with low cost of equipment seem likely to suggest the potential of this modality for disrupting biofilms. However, this has not been the case. It has been shown that ultrasound delivery can have a positive role in supporting bacterial biofilms at lower frequencies. Specifically, Pitt et al. [52] showed increased production of *Pseudomonas aeruginosa* and *Staphylococcus epidermidis* bacteria on surfaces when the bacteria were exposed to an ultrasonic wave intensity of 2 W/cm^2 at a frequency of 70 KHz for 48 hours. The pulse duration was 100 milliseconds and repeated every 500 milliseconds. Carmen et al. [53] hypothesize that the ultrasound at these frequencies increased permeability, increasing diffusion of essential nutrients, which in turn enhanced bacterial growth. In contrast, Qian et al. [54] showed that increased permeability caused an increase in the antimicrobial efficacy of antibiotics establishing that low-intensity ultrasound (500 KHz with a power density of 10 mW/cm^2) when coupled with an antibiotic could be used to kill bacteria. However by itself, low-intensity ultrasound could not disrupt the biofilm.

2.3.4 Shockwave Therapy

2.3.4.1 Extracorporeal Shock Wave Therapy

Extracorporeal Shock Wave Therapy (ESWT) has been the standard technique to fragment renal calculi ("kidney-stones") by lithotripters [55]. ESWT are characterized by peak compressive pressures of up to 100 MPa and negative pressures of $5 - 10$ MPa whereby these pressure profiles travel through fluid and tissue mediums and their me-

chanical effects are due to impedance mismatches [56]. The effect of the negative pressure causes cavitation bubbles to form that have secondary effects such as the generation of secondary shockwave fronts that play a major role to the disintegration of the kidney-stones [57]. ESWT technology has been implemented for the management of wound care and has been explored for its ability to stimulate the regeneration of tissue [58,59] and to increase bone formation and healing of overlying soft tissues in cases involving nonunion and delayed bone healing [60]. Moreover, ESWT was explored for its ability to increase angiogenesis and ultimately wound healing effects [61–63]. Thus utilizing mechanical shockwaves could probe beneficial as a treatment modality.

The antibacterial effects caused by ESWT have been documented. Gerde-smeyer et al. showed reduced growth of *Staphylococcus aureus* when the bacteria colonies were subjected to 4000 impulses at 2 Hz with a pulse energy flux of 59 mJ/cm^2 [64]. Other studies [65–67] concluded on antibacterial effects of high energy shockwaves on plank-tonic microorganisms. These studies only support antibacterial effects of ESWT directly on cells in suspension.

ESWT has also been used to remove biofilms from surfaces [68]. These results showed that though some of the biofilm was removed from from the surface of teeth, there was no effect on the viability of the collected bacteria. A fundamental understanding of the stress waves generated to the effect on bacterial cells and tissue is needed. ESWT stress waves have both compressive and tensile pressures as it propagates.

2.3.4.2 Laser-Generated Shockwaves

Laser-generated shockwave (LGS) technology is not new to the medical field. Unlike ESWT which has a tensile component in its stress profile that leads to cavitational phenomenon, LGS are uniplor compressive waves. It is currently used in cataract surgery for extraction and photolysis of the lens and for prevention of secondary cataract formation [69]. Unlike standard ultrasonic energy, this laser emulsification of cataract produces no clinically significant heat at the incision site, thus avoiding any sclera burns during cataract surgery [70]. Previous studies have shown that cell-permeability can be obtained

by using LGS to deliver macromolecules and genes through the cell plasma membrane and even skin [71–74]. In fact, LGS has been shown to ehance the permeability of bacterial biofilms [75, 76]. Cell permeability byway of LGS is determined on parameters such as the rise time, pulse duration, and number of pulses [77] and are yet to be determined in order to have a greater effect on biofilms. The effect of shockwave rise time will determine the permeability of cells. In fact, Doukas et al. [78] showed that stress wave gradient had a greater effect on cell viability than the peak stress of the wave.

Krespi et al. [79] used laser-generated stress waves to disrupt *Pseudomonas biofilms* in vitro on various targets such as culture plates, stainless steel screws, sutures and tympanostomy tubes. Nd:YAG laser pulses between 4 ns and 8 ns duration and 8 mJ and 12 mJ energies were focused via an optical fiber onto a Ti target immersed in a low-streaming liquid inside a hollow cylindrical probe. The generated stress waves were made to impinge areas on which a biofilm was grown. It was reported that 10 to 20 stress waves, each with an amplitude of $0.8 - 1\ GPa$ were needed to break away chunks of the biofilm from these substrates. Their results showed that the biofilm can be pried off from the surface without any visual damage to the underly host structure and that with each stress pulse, the biofilm becomes more permeable [80]. The permeability of the biofilm structure would allow the addition of antibiotics to the coupling medium. In fact, when shockwaves are coupled with antibiotics, there is a reduction in bacterial viability [81, 82]. These pressure values reported were not directly measured but inferred and no stress wave profiles were reported. A study by Nigri et al. [83] has shown that there is no direct effect of LGS on the viability of the microbial cells within. The stress profiles reported had pulse durations of 300 ns and rise times of 30 ns. It is suggested that LGS with fast rise times increase the permeability of the cell membrane without killing the cells.

Properly controlled shockwaves can have beneficial effects on cellular function. Till this date there have been no studies which establish any parameters that control detachment and disruption of the biofilm at the local scale.

2.3.4.3 Summary

A variety of methods have being implemented in trying to rid biofilms from biomaterials and also wound surfaces. They have varied from chemical methods, antibiotic mechanical methods including pulsed ultrasound. Laser-generated shockwaves are explored for their ability to create enough mechanical stress to mechanically delaminate the biofilm from surfaces and to effectively deliver drugs. This study explores the use of specific laser-generated shockwaves to study the efficacy on bacterial biofilms and quantify adhesion strength measurements. By understanding the adhesion strength of bacterial biofilms, techniques can be developed in order to ultimately develop technologies that would ultimately rid of biofilms off surfaces.

2.4 Current state of knowledge of Biofilm Mechanics

A fundamental understanding of mechanical properties of biofilms is needed in order to understand how biofilms respond to mechanical forces in the natural environment. To this end, it is also an important parameter in understanding how strongly biofilms grow on surfaces. If these mechanical properties are more properly understood, tools can be developed to rid of these films with defined adhesion strength parameters. In fact, laser-generated shockwaves have been successfully used to measure the adhesion strengths of mammalians to different surfaces [84, 85]. Biofilms can be regarded as soft materials that exhibit viscoelastic properties [86]. Therefore biofilms a a time-dependent response under externally applied mechanical forces.

2.4.1 Measurement tools and their limitations

Many measurement tools have been used to characterize biofilm properties. Cense et al. [1] provided a general overview of some measured mechanical properties of biofilms and are reported in Table 2.1. There are large discrepancies between the the mechanical properties measured. In fact, they differ about 2 orders of magnitude. The reason for this disparity is partly due to the loading-type of each measuring defice. Rheometers are

used to quantify adhesion strength under shearing forces while micro-indenters are used to extract elastic moduli as these devices provide compressive forces. Even if similar devices are used, there still exists differences in published material properties due to the fact that biofilms will grow differently under various conditions. The conditions of growth will also determine biofilm growth. Biofilms can either grow under dynamic conditions, or under continuous shearing forces, like those experienced in biofilm reactors. Biofilms growth will differ when grown in static conditions. Aravas and Laspidon [87] suggested that discrepancies in measurements are due to loading type. In fact, some compression tests show a stiffening effect due to the closure of the biofilms or the compression of the bacterial exopolysaccharide matrix. Spinning-disk rheometers [88, 89] measure mechanical deformations under shearing stresses. The extracted parameters of the biofilm, however, are measured and averaged over a large area of the plate. There is also variance in strain due to radial dependency. Microjet impingement utilize hydrodynamic forces that impinge biofilm structures and shear off cells [90–92] [92]. However, shearing forces caused by microjets can go above the cohesive strength of cells, thereby rupturing them. Thus the mechanisms of loading are mixed. Microindentors provide improved local measurements over a $\sim 20\ mm$ area [1]. Failure was measured by applying shear forces until disruption of biofilm is achieved. Mechanical properties are measured by pressing into material and measuring resistive force.

2.4.2 Strain-Rate Dependence

Tensile forces are required to delaminate the biofilm from the surface. Only 1 study utilizes purely tensile forces to extract biofilm mechanical properties, including cohesive strength, under varying strain rates utilizing a microindentor device [97]. Strain rates between $0.013 - 9.10\ s^{-1}$ are explored. Results show that the maximum failure strength, elastic modulus, and toughness increase with increasing strain rate between $0.013 - 0.130\ s^{-1}$. This partly explains why published material properties vary greatly. In a viscoelastic model, viscous effects becomes more important at longer time scales or lower strain rates. The study, however, presents cohesive failure of the biofilm since they are

Table 2.1: Review of mechanical properties different biofilm material properties. These values are inspired by Cense et al. [1]. ($G \equiv Shear\ Modulus$, $E \equiv Young's\ Modulus$, $\eta \equiv Viscous\ Coefficient$

Authors	Species	Method	$G\ [Pa]$	$E\ [Pa]$	$\eta\ [Pa \cdot s]$
Stoodley et al. (1999) [93]	mixed	visual	27 ± 1	40 ± 8	–
Klapper et al. (2002) [94]	P. aeruginosa	visual	65 ± 21	–	–
Shaw et al. (2004) [89]	S. mutans	rheometer	$10 - 1000$	–	$10^4 - 10^6$
Towler et al. (2003) [95]	mixed	rheometer	$0.3 - 45$	–	$10 - 7000$
Vinogradov et al. (2004) [88]	S. mutans	rheometer	1900 ± 3800	–	$(2.8 \pm 6.4)\ 10^5$
Körstgens et al. (2001) [96]	P. aeruginosa	compression	–	6500 ± 500	–

weaker than the adhesive forces of the biofilm. Utilizing the Laser Spallation Technique as a measurement tool proves to be more beneficial as it is capable of generating very high strain rates of up to $10^7 s^{-1}$.

2.5 The Basic Laser Spallation Technique (LST)

Laser pulses impinging upon a thin metallic surface generate stress waves within the material. The laser energy ablates the thin metallic film, thereby causing a rapid thermal expansion of the film resulting in a compressive wave propagating through the substrate. The laser fluence, pulse width, and the substrate material properties contribute to the temporal characteristics of the stress wave. Gupta et al. [98–103] optimized laser-generated stress wave profiles for measuring the tensile strength of a thin film interfaces. Because of the high strain-rate loading ($\sim 10^7 s^{-1}$), all inelastic effects are suppressed during interface decohesion, and thus, the measured strengths are intrinsic and related directly to the atomic microstructure and chemistry of the interfacial region. This was exemplified [104, 105] by measuring the tensile strengths of Nb/sapphire interfaces whose structure and chemistry were characterized using high resolution transmission electron microscopy and modified by a combination of heat treatment and deposition of 5 to 40 Å thick interlayers of Cr and Sb. Similarly the effects of the Nb deposition mode (RF vs. DC), grain scale substrate roughness, and substrate orientation (prismatic vs. basal) were systematically studied [106], with the sensitivity of the experiment in capturing the influence of the substrate orientation realized in terms of unique spallation patterns that in turn could be directly related to interfacial atomic arrangement. Thus, atomic-scale tailoring of the interfacial region for either maximizing or reducing adhesion can be accomplished. Using this technology, interfacial strengths in the range of 0.1 GPa (14.5 ksi) to 2.5 GPa (362 ksi) have been measured in a variety of engineering systems (paints, multilayer electronic devices, engines, tribology) involving metal, ceramic and polymeric coatings deposited on metal, semiconductor and ceramic substrates.

In the Laser Spallation Technique experiment, a 3 $\sim$ 6 nanosecond (ns) long Nd:YAG laser pulse is impinged over a 3 mm diameter area on a 0.5 μm aluminum (Al) film sandwiched between the back surface of a substrate disc and a 50 to 100 μm thick layer of waterglass (SiO_2) [U.S. Patent 5, 438, 402] as shown in Figure 2.1. The melting-induced expansion of Al under confinement generates a compressive stress wave (with sub-nanosecond rise-time) directed towards the test coating, which is deposited on the
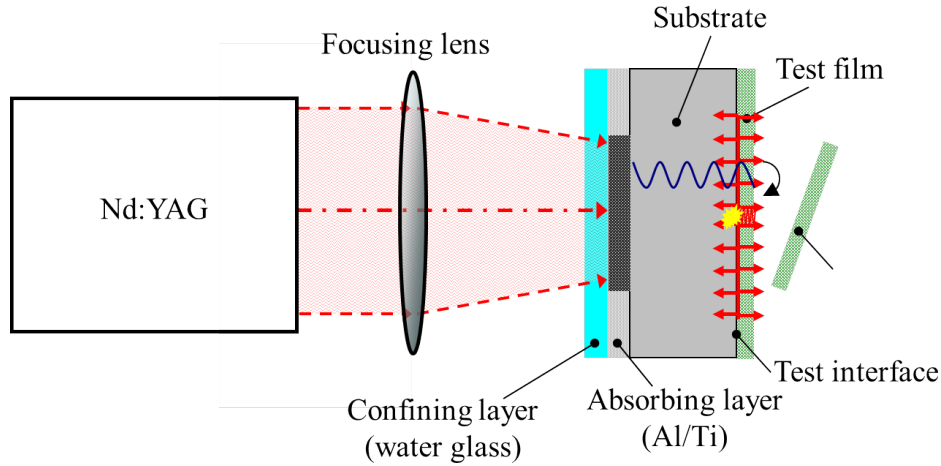
Figure 2.1: The schematic experimental setup of the basic Laser Spallation Technique.

substrate's front surface. The compression stress pulse reflects into a tensile wave from the coating's free surface and leads to its spallation (complete removal) at a sufficiently high amplitude. Thus the required minimum laser energy to cause the spallation is determined as the minimum energy required to generate a stress pulse with sufficient peak stress that overcomes the adhesive strength of a material interface. The LS technique also incorporates a state-of-the art displacement interferometer to measure the free surface displacement as the wave propagates toward the free surface. The displacement can be ultimately used to relate to the input stress generated into the substrate. The next section will discuss new modifications to the LS technique and details of the displacement interferometer and subsequent calculation of input stresses.

2.5.1 Modified Laser Spallation Technique: "Top-Down" setup

The samples involved in the study incorporate liquid coupling layers that are needed to couple the shockwaves toward biological samples. The previous system was limited in that it only allows for horizontal application of the laser energy. The new "Top-Down" setup was designed to allow for the application of the high-energy ND:YAG pulse from the top, while a more compact displacement interferometer is placed under the sample to measure the surface displacement. This newer setup allows for more precise and rapid application of the laser pulse and also on the acquisition of the surface displacement.

17
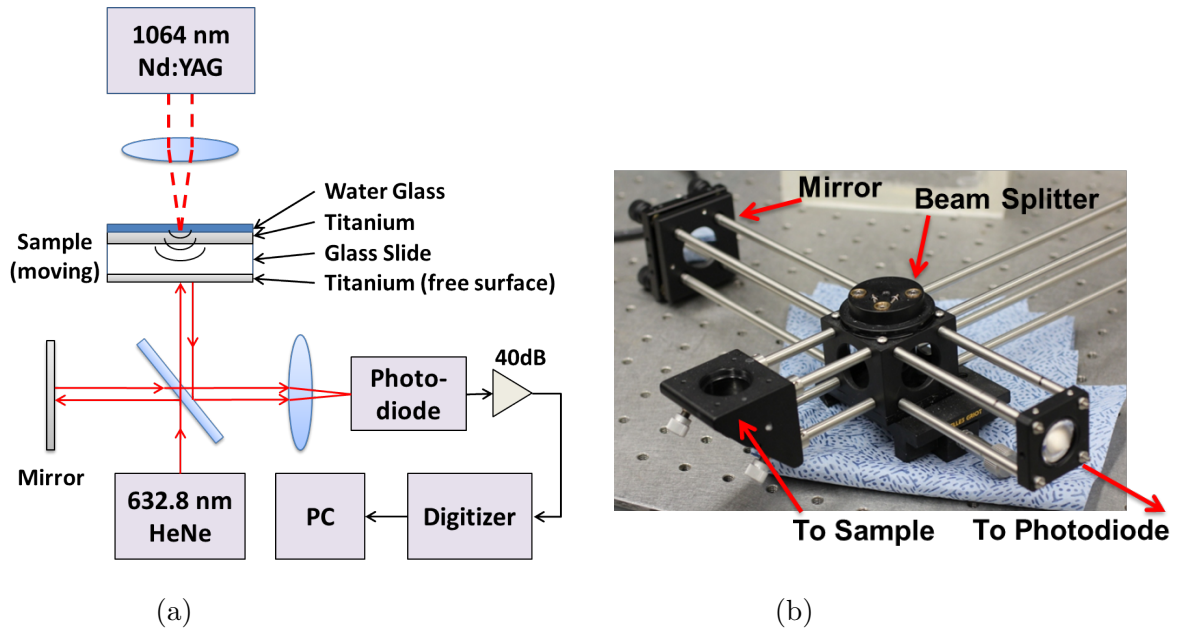
Figure 2.2: Interferometry System: (a) Diagram of Interferometer and Sample (b) Actual interferometer device.

The displacement interferometer is based on a Michelson Interferometer [107], as shown in Figure 2.2. In this newer setup, 0.5 μm Titanium (Ti) is used as a the absorbing layer for its biocompatability [108]. It is constrained with $15 - 20~\mu m$ of water glass. The reflective layer or "free surface" is coated with 0.04 μm Ti and acts as the "sample arm" of the displacement interferometer. On the free-surface end a 632.8 nm frequency stabilized laser goes through a 50/50 beam splitter, separating one arm of the interferometer toward a reference mirror and the other arm towards the sample. The beams then recombine and are focused by a lens onto an ultra high-speed photodector (Hamamatsu $MSM-64178$). As the laser ablates the absorbing layer, a compressive wave is generated and propagates toward the free surface and as a result, the surface displacement offsets the sample arm, causing a varying phase shift in the measured signal. The signal is recorded by a high speed waveform digitizer (Tektronix SCD1000) in single-shot mode with a 0.2 ns in temporal resolution and dynamic rise times of up to 5 ps. The typical signal is an oscillating pattern, with the peaks corresponding to constructive interference and troughs corresponding to destructive interference. The resulting waveform measures the output voltage and time from the photodetector. The photodetector outputs the voltage

amplitude $A_0(t)$ recorded by the digitizer and can be expressed in terms of the free surface displacement $u_0(t)$.

$$A_0(t) = \frac{A_{max} + A_{min}}{2} + \frac{A_{max} - A_{min}}{2} sin(\frac{4\pi}{\lambda} u_0(t) + \delta) \tag{2.1}$$

Where t is the time, the A_{max} and A_{min} are the global maximum and minimum fringe amplitudes, respectively, λ is the wavelength of frequency stabilized laser (632.8 nm) and δ is the a phase angle in radians. The free surface velocity can be calculated by differentiating the free surface displacement, $u_0(t)$.

2.5.2 1-D Wave Propagation Theory

The generated stress pulse with respect to laser energy can be theoretically calculated by experimentally measuring the transient displacement history of the substrate free surface as shown in Figure 2.2a. According to the longitudinal wave propagation theory, the particle displacement and velocity of any point in the substrate can be assumed as:

$$u(x,t) = u_s(t + \frac{x}{c}) + u_s(t - \frac{x}{c}) \tag{2.2}$$

$$v(x,t) = v_s(t + \frac{x}{c}) + v_s(t - \frac{x}{c}) \tag{2.3}$$

where the subscript s represents the substrate and c is longitudinal wave velocity in the substrate and is assumed to be constant. Under plane strain and one dimensional wave propagation assumptions, the strain and stress along x-axis can be presented as:

$$\epsilon(x,t) = \frac{\partial u}{\partial x} = \frac{1}{c}\left[v_s(t + \frac{x}{c}) + v_s(t - \frac{x}{c})\right] \tag{2.4}$$

$$\sigma(x,t) = (\lambda + 2\mu)\frac{\partial u}{\partial x} = \rho c\left[v_s(t + \frac{x}{c}) + v_s(t - \frac{x}{c})\right] \tag{2.5}$$

where λ and μ are the Lamé constants and ρ is the density of the substrate. Using the boundary condition at the free surface:

$$\sigma(0,t) = 0 \tag{2.6}$$

$$v_0(t) = v(0,t) = 2v_s(t) \tag{2.7}$$

where $v_0(t)$ is the transient velocity of the free surface obtained by the interferometry. Finally, the compressive stress generated can be derived and expressed as:

$$\sigma_i = \sigma(h, t - \Delta t) = -\frac{1}{2}\rho c v_0(t) \tag{2.8}$$

19

The stress wave is generated and propagates as a one-dimensional planar wave over a circular cylindrical region, by keeping the ratio of the diameter of the laser heating spot to the total pulse propagation distance to be at least 3 [109]. Under lateral constraints, the stress pulse propagates under uniaxial strain conditions and the wave velocity c in can be related to the Lamé constants λ and μ by:

$$c = \sqrt{\frac{\lambda + 2\mu}{\rho}} \tag{2.9}$$

where λ can be related to the Young's modulus E and the shear modulus μ to Poisson's ratio ν.

The free surface displacement function u_0 from Equation 2.1 and corresponding free surface velocity can be expressed as:

$$u_0(t) = \gamma \left\{ -\alpha[e^{-t/\alpha} - 1] + \beta[e^{-t/\beta} - 1] \right\} \tag{2.10}$$

$$v_0(t) = \gamma \left\{ \alpha e^{-t/\alpha} + \beta e^{-t/\beta} \right\} \tag{2.11}$$

Therefore, the generalized expression to fit the raw waveform from the photodector can be determined by combining equation 2.1 and equation 2.11 to get:

$$A_0(t) = \frac{A_{max} + A_{min}}{2} + \frac{A_{max} - A_{min}}{2} sin(\frac{4\pi}{\lambda} \gamma \left\{ -\alpha[e^{-t/\alpha} - 1] + \beta[e^{-t/\beta}) - 1] \right\} + \delta) \tag{2.12}$$

The function 2.12 is the complete function in order to fit the raw waveform from the photodetector. Six constants α, β, γ, A_{max}, A_{min}, δ must be determined and fitted to the data in order to have a unique solution. However, this is very difficult and a different strategy is implemented to determine the surface displacement. From the raw data the time points of the peaks and troughs of the fringes could be obtained. Each peak to trough is separated by a distance of $\lambda/4$, where λ again is equal to the wavelength of the HeNe frequency stabilized laser of 632.8 nm. After obtaining the displacement vs time values, OriginPro 8 was used to fit the displacement function 2.10 vs. time plot to obtain the constants α, β, γ. The stress generated in the substrate can be directly calculated by combining equations A.11 and equations 2.11 and the fitted constants as:

$$\sigma_i = -\frac{1}{2}\rho c \gamma \left\{ \alpha e^{-t/\alpha} + \beta e^{-t/\beta} \right\} \tag{2.13}$$

Once the generated input stresses is calculated, a $1-D$ Analytical Wave Propagation Model (Appendix A) is used to find the interface stress history of the different layers used in the experimental model. It is difficult to do any interferometric measurements off biological samples since the sample-arm of the system must have a reflective surface.

CHAPTER 3

Adhesion strength studies of *S. epidermidis* biofilms using glass-modified shockwaves

3.1 Introduction

Chapter 2 provided strong evidence to support the use of laser-generated shockwaves to disrupt bacterial biofilms. In order to develop methodologies to rid biofilms off surfaces, whether biotic or abiotic, a fundamental understanding of how strongly biofilms attach is imperative. This chapter will implement the modified Laser Spallation Technique (LST) to determine adhesion strengths of *S. epidermidis* biofilms grown of polymeric surfaces. More specifically, bacterial biofilms will be grown on untreated polystyrene petridishes. Microscope slides (soda-lime glass) are explored for its ability to generate very high compressive stress and also for its ability to generate rarefaction shocks under higher stress loading [107], thereby allowing for the adhesion strength measurements of very thin interfaces.

3.2 *Staphylococcus epidermidis*

The microorganism used in this studies is *S. epidermidis*. It is a Gram-positive cocci ("spherical-shaped"), coagulase-negative, organism that is part of the *Staphylococcus* genus. It has previously been thought of as a harmless microorganism as it was commonly found on human skin. Currently, *S. epidermidis* is regarded as an opportunistic pathogen that cause nosocomial ("hospital-acquired") infections [110].

3.3   Materials and Methods

This section will provide the reader the necessary biological laboratory preparation of properly growing bacteria and storing bacterial samples.

3.3.1   Sample Preparation: Bacterial Stock

S. epidermidis (ATCC #35984, Designation: $RP62A$) is used as the bacterial sample for its ability to produce the polysaccharides adhesin. A bacterial raw sample is delivered by the American Type Culture Collection ("ATTC") in freeze-dried form. It is necessary to develop vials of bacterial stock that can be stored for years in a deep freezer ($-80°C$) in a gylceral solution. If the cells were directly stored in water, the crystallization of the water can pierce and damage the bacterial cell wall and effectively kill them. The procedure to develop a stock of bacteria is as follows:

1. Prepare food medium by placing 30 g Tryptic Soy Broth ("TSB"; BD Bacto # 211825) into 1000 mL of deionized (DI) water and autoclave at $121°C$

2. Place 40 mL of TSB into a 50 mL conical centrifuge tube (BD Falcon #352070)

3. Use a pipette tip to scrape off frozen bacteria from the a sample delivered by ATTC into the 50 mL test tube with TSB

4. Vortex to evenly mix then place into an incubator ($37°C$ & 5% CO_2) for 24 hrs

5. After overnight growth, the 50 mL test tube is centrifuged at 3000 rpm for 15 minutes at room temperature to pellet the bacteria

6. Discard all supernatant and resuspend the pelleted cells with 10 mL sterile DI water

7. Aliquot 500 μl of sterile 30% glycerol solution in water to 1.7 mL microcentrifuge tubes (Eppendorf #022431081)

8. Aliquot 500 μl of overnight stock into microcentrifuge tubes

9. Vortex and store in cryogenic freezer ($-80°C$)

3.3.2 Sample Preparation: Biofilm growth on polystyrene petridish

From the stored bacterial stock, a vial is taken and a pipette tip is used to scrape off some of the ice into a 50 mL test tube containing 40 mL of TSB. The vial must not be thawed as a freeze-thaw cycle could potentially kill the cells. The test tube is then placed in an incubator at standard conditions for 24 hrs in order to increase cell population. It is then important to know the concentration of bacterial after an overall growth. A spectrometer is used to measure the optical density of a sampled suspension at a wavelength of 600 nm (*Biocompare Ultrospec 10 Cell Density Meter*). A calibration curve for the device is done and shown in Figure 3.1 where the amount of colony forming units (CFU) per 1 mL of solution is measured against the optical density (OD). The overnight suspension is then diluted if necessary to an $OD_{600\ nm} = 0.2$ corresponding to a cell density of $\sim 4.77 \times 10^7\ CFU/mL$. Then, 5 mL of the stock solution was aspirated from the stock into 100 mm x 15 mm polystyrene petri dishes and allowed to grow in a incubator chamber ($37°C$ & $5\%\ CO_2$) for 24 hours [111] under static conditions.

3.3.3 Sample Preparation: Glass-Slide Metalization

Microscope slides (soda-lime glass) with dimensions of 3 x 1 $inch$ by 1 mm thick are RF sputtered (Denton Discovery II 550) with 0.5 μm of Titanium (Ti). A uniform layer of waterglass (SiO_2) is then spin-coated on top of the Ti to achieve a uniform layer of 15-20 μm. The waterglass layer acts as the constraining layer and is transparent to the Nd:YAG laser wavelength of 1.064 μm.

3.3.4 Experimental Procedure

After 24 hour growth, the petridishes with bacterial solution were washed 5× with phosphate buffer saline (PBS) [112]. Any remaining bacteria is considered biofilm as shown in Figure 3.2a. Samples were then stained with Alcian Blue. Alcian Blue stains acidic polysaccharides which are produced by bacteria in the biofilm. The stain allows for im-
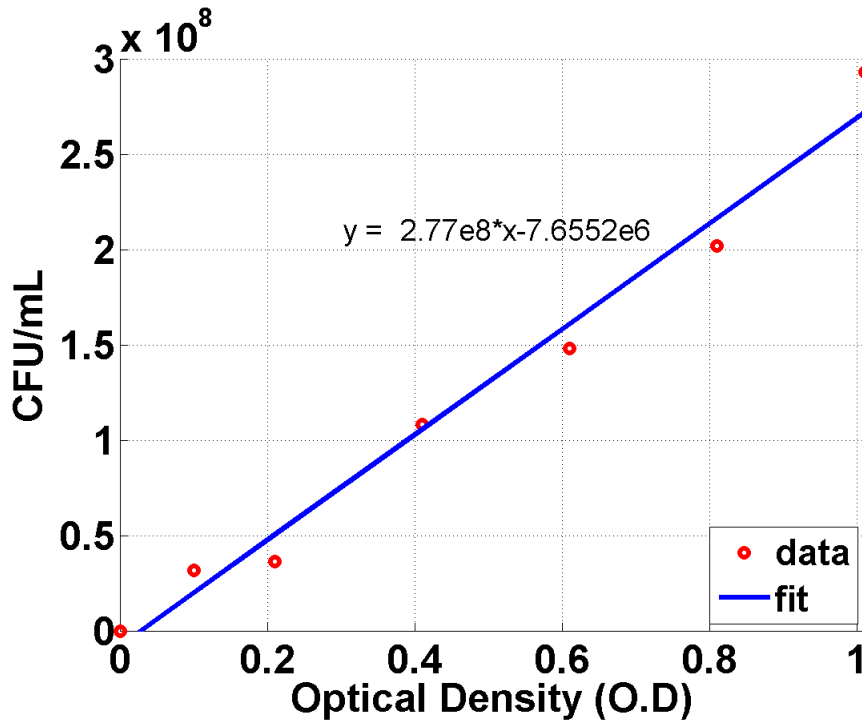
Figure 3.1: Optical Density (OD) calibration curve for Ultraspec 10 Cell Density Meter

mediate visualization of the biofilm with light microscopy. Preparation and staining of sample with Alcian Blue is as follows [113]:

1. Prepare 3% of Acetic Acid solution by volume by combining and mixing glacial acetic acid and distilled water

2. Mix 1 gram of the Alcian Blue Kit (SGX) into the 3% acetic acid until a stable pH of 2.5 is acheived

3. Apply 1 mL into each 100 mm petridish containing the 5×-washed samples

4. Allow for 30 minutes of staining

5. Wash with distilled water 3×. The stained samples are shown in Figure 3.2b.

The petridishes were then placed atop a water reservoir Figure 3.3. The Ti sputtered glass slides were introduced by two rigid tapes at the ends that allowed for a $\sim 1.0 \ mm$ coupling thickness. PBS was then applied to couple the shockwave toward the biofilm. Enough fluid was used until there was no air bubbles. This is very important as any air

25

| (a) | (b) |
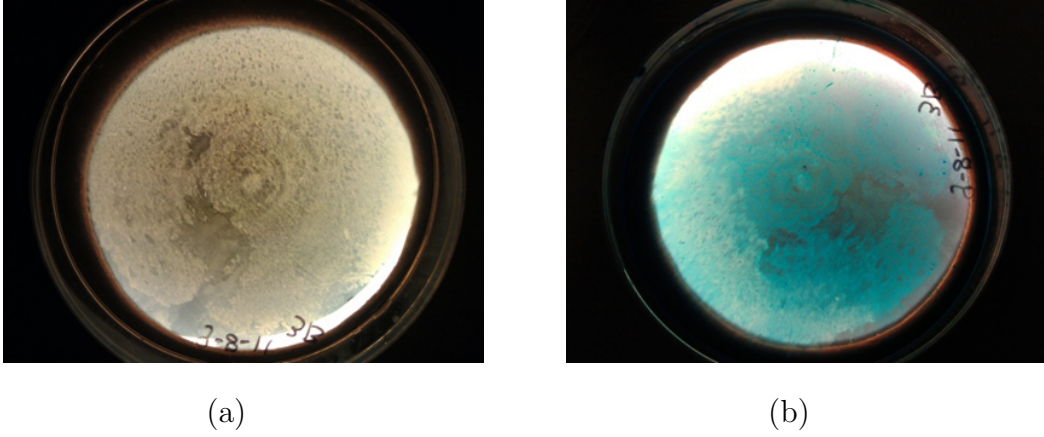
Figure 3.2: Alcian Blue staining of *S. epidermidis* grown on polystyrene. (a) Pre-staining: Washed 5× with PBS. (b) Post-staining: Excess Alcian blue stain is washed 3×.

interfaces can lead to immediate reflections of the compressive waves due to the large impedance with air. The samples were then ready for shockwave application.

A $2 \sim 6$ nanosecond long $1,064\ nm$ Nd:YAG laser pulse was made to impinge over a $\sim 3\ mm$ diameter area onto Ti surfaces and the absorbed laser energy leads to volumetric expansion due to the generated plasma and thus leading to the generation of a compressive shock wave directed toward the water and toward the biofilm. To find the amount of laser energy used per pulse, the beam first goes through a $60-40$ beam splitter where 60% of the energy goes to the actual sample and 40% is the reference energy measured by the energy meter. By calibrating the reference energy used, the actual energy to the sample can be calculated. The critical energy fluence, or the amount of laser per pulse needed to qualitatively delaminate the biofilm, is found by starting from the lowest energy output of the laser and increasing the laser energy by the minimum resolution of the laser to $2\ mJ - 5\ mJ$ per pulse. The laser energy varied from $77\ mJ - 640\ mJ$ per pulse. The spot size was fixed to a diameter of $3\ mm$. Once the critical energy threshold is achieved, several higher energies are also explored due to rarefaction shocks in glass as evidenced by Gupta et al. [107]. Shocked samples are then viewed by standard light microscopy methods.

(a)	(b)
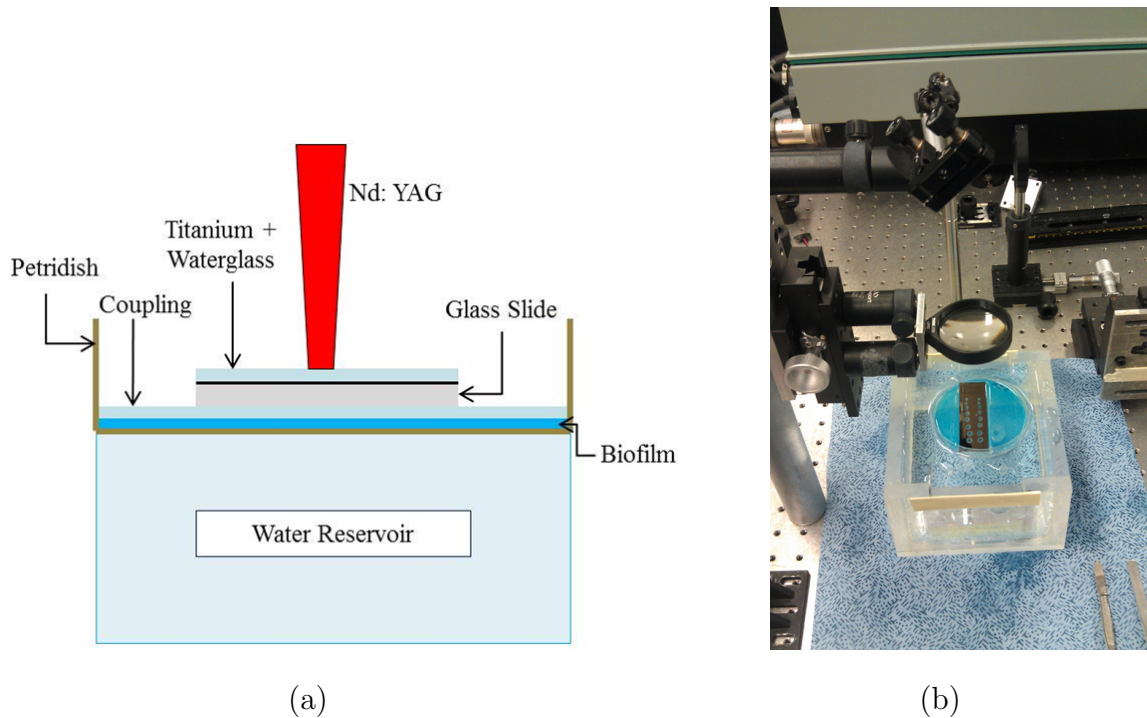
Figure 3.3: Experimental setup to apply shockwaves of *S. epidermidis* grown on polystyrene. (a) Diagram and sample. (b) Actual experimental setup.

3.4 Qualitative Results by Light Microscopy

Figure 3.4 shows the effect of the laser generated shockwaves under increasing energies. At higher energies, more of the biofilm is delaminated as more of the shocked area has enough tensile stress to cause interface failure between the biofilm and the polystyrene interface. Figure 3.5 shows the light microscopic views of the delaminations under $4\times$ magnification. Images were acquired through a color CCD camera (Motic 2.0). Figure 3.5a shows some delaminations in the upper-left side of the image. However, these were not created due to the shockwaves but due to the natural growth of the biofilm. The maximum stress is located near the center of the image. Due to the dynamic growth of the biofilm uniform layers are not achieved. There are areas of delaminations that occur during the growing stages and is difficult to control.

At the critical energy value of 30 mJ/mm^2, cavitation and delaminations are evident across 24-hour to 72-hour growths (Figures 3.5-3.7). This energy is the critical threshold energy used to measure the input stress by the displacement interferometer. Once the

input stress is determined, it is used as the input stress to the $1-D$ Analytical Wave Propagation model.

It is important to note that the stress wave propagation is a $3-D$ effect during the experiment. As a result, there are viscous forces, as the stress wave propagates, that lowers the particle displacement and ultimately stress profile that varies radially away from the center of the shocked region. This explains why even though the shocked area is $3\ mm\ dia$, there is at most $1\ mm$ diameter delaminated areas at the highest energies. However, as a measurement for adhesion strength, it is important to capture the maximum particle displacement during the interferometry.

3.4.1 Cavitation Phenomenon

Cavitation bubbles are evident during the experiment and in Figures 3.5c , 3.5d, and 3.6c. Cavitation is caused when water experiences tension failure [**?**]. Due to the large impedance between the water and glass interface, cavitation bubbles are generated but only cause biofilm delamination areas on the order the the diameter of the bubbles. The tensile component of the laser generated stress wave causes the primary mode of delamination. Chapter 5 will present a high-speed imaging system to better understand cavitation phenomenon.

3.5 Shockwave Wave Characterization by modified Laser Spallation Technique (LST)

Once the critical laser energy fluence needed to qualitatively delaminate the biofilm was obtained, the stress wave generated can be found by the modified LST to find the input stress to the glass slide. The input stress at the 7 energies levels were found and characterized and because of the modified experimental setup, it was also possible to measure the input compressive to the polystyrene to find out how much compressive stress propagated through all the mediums. Both experiments will be presented. The LST is also used to measure and average ($n = 7$) the input stresses and interface stress
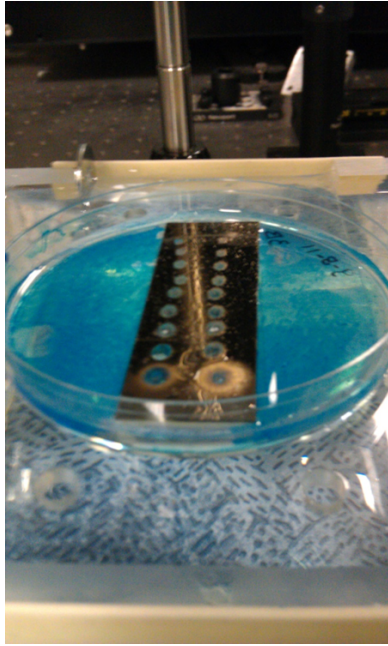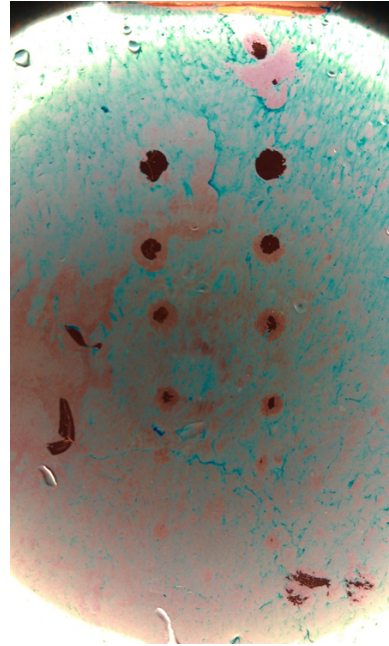
<div align="center">(a)   (b)</div>

Figure 3.4: Image of Alcian Blue stained samples after shockwaves under increasing laser energies. (a) Sample immediately after shocking showing ablated regions of Ti. (b) Focused view of sample showing delaminated areas. Higher energy fluences yielded larger areas of delamination.
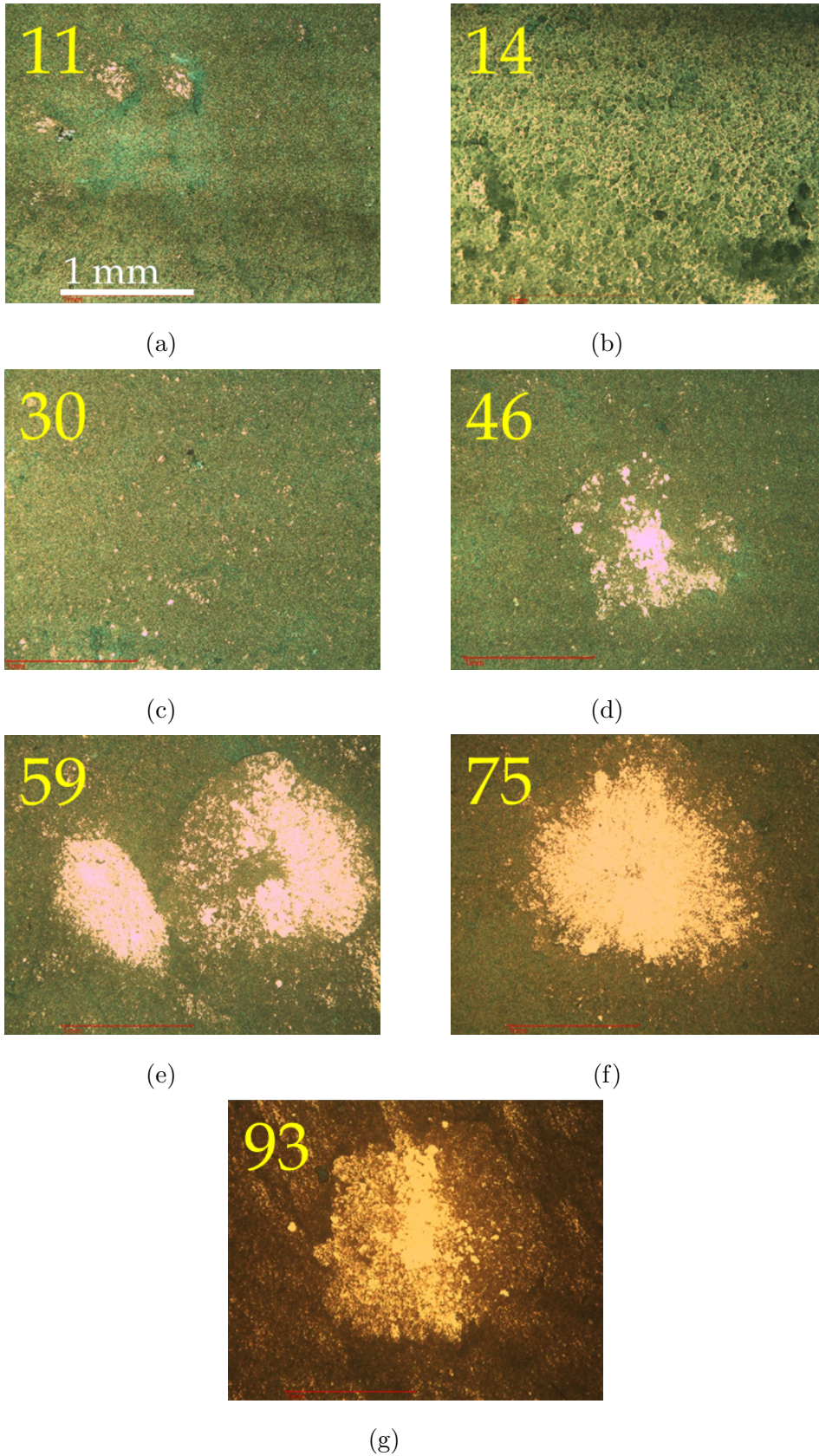
Figure 3.5: Light microscope images of locations under shockwave treatment at $4\times$ magnification after 1 day (24 hr growth). (a) 11 mJ/mm^2. (b) 14 mJ/mm^2. (c) 30 mJ/mm^2. (d) 46 mJ/mm^2. (e) 59 mJ/mm^2. (e) 75 mJ/mm^2. (e) 93 mJ/mm^2. Scale = 1 mm.
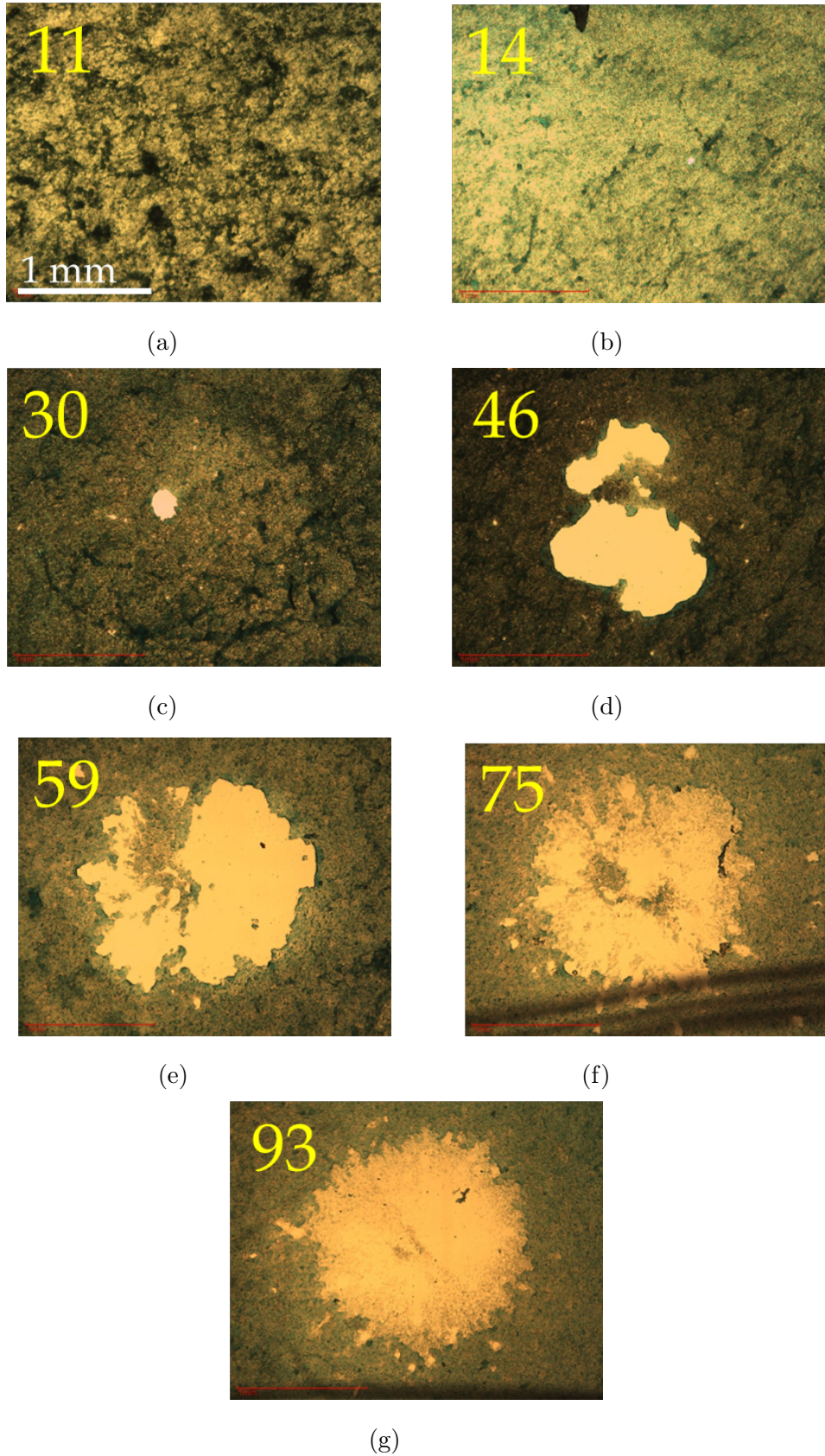
Figure 3.6: Light Microscope images of locations under shockwave treatment at 4×
magnification after 2 day (48 hr) growth. (a) 11 mJ/mm^2. (b) 14 mJ/mm^2. (c)
30 mJ/mm^2. (d) 46 mJ/mm^2. (e) 59 mJ/mm^2. (e) 75 mJ/mm^2. (e) 93 mJ/mm^2.
Scale = 1 mm.
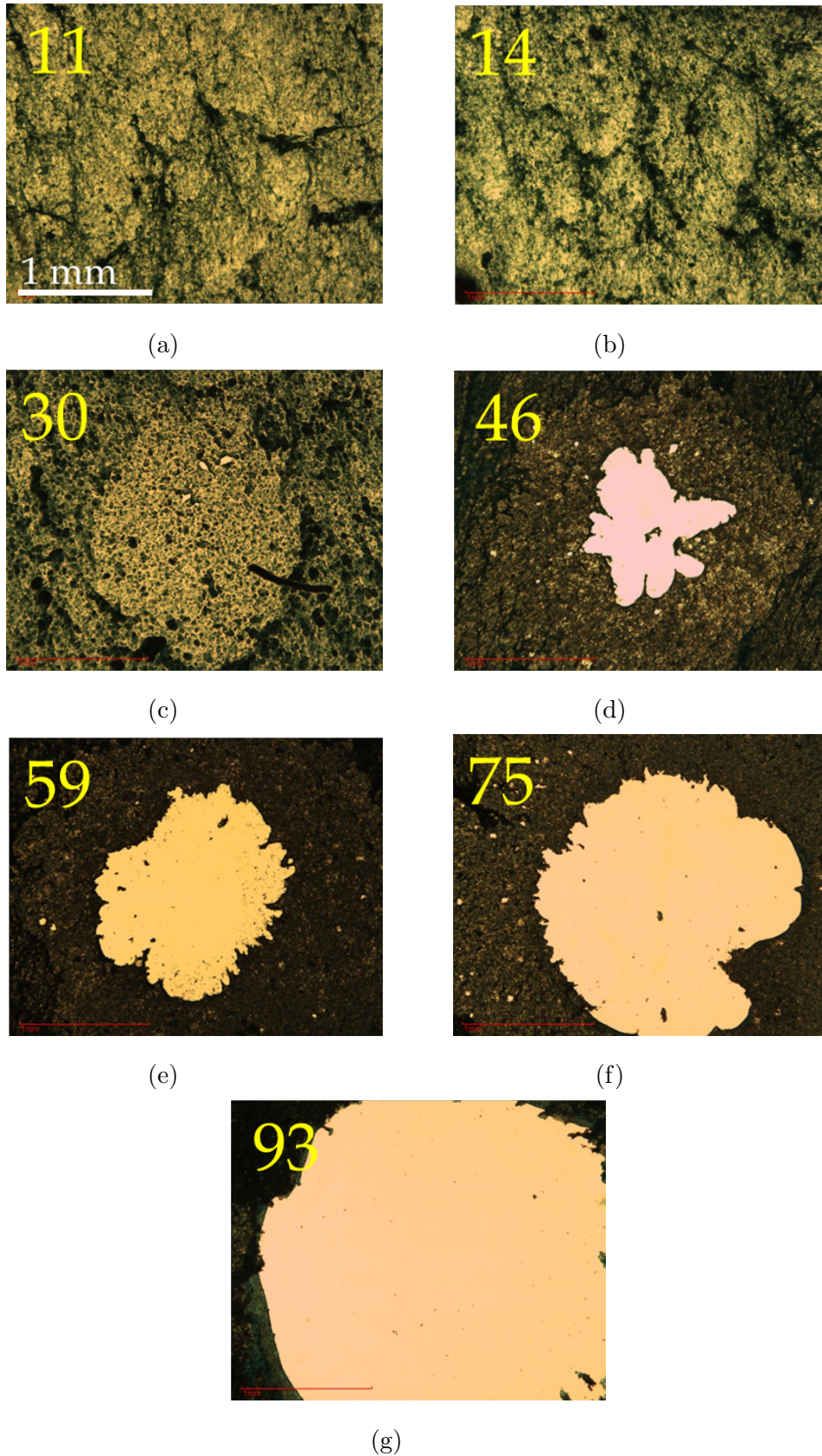
Figure 3.7: Light Microscope images of locations under shockwave treatment at 4×
magnification after 3 day (72 hr) growth. (a) 11 mJ/mm^2. (b) 14 mJ/mm^2. (c)
30 mJ/mm^2. (d) 46 mJ/mm^2. (e) 59 mJ/mm^2. (e) 75 mJ/mm^2. (e) 93 mJ/mm^2.
Scale = 1 mm.

historys causing biofilm delamination. The qualitatively results showed delaminations centered around a laser fluence of $\sim 30 \ mJ/mm^2$. The displacement fitting parameters, as discussed in Chapter 2.5.2, are used to find the input stresses that are implemented into the $1 - D$ wave model to obtain the peak interface tensile stresses.

3.5.1 Shockwave Characterization: Glass

It is necessary to experimentally find the stress generated in the glass slide by utilizing the displacement interferometer. Once this stress profile is known, it will become the input stress to the $1 - D$ stress model in order to find the interface stress history.

3.5.1.1 Materials and Methods

To characterize the stress wave generated, glass microscope slides (3 *inch* by 1 *inch* by 1 *mm* thick) are used and shown in Figure 3.8. The top side was RF sputtered with a titanium layer of 0.5 μm. A $15 - 20 \ \mu m$ water glass layer was spin-coated upon the Ti and acts as the constraining layer during ablation. At the bottom of the glass slide, a 0.04 μm layer of titanium was sputtered as the reflective layer (free surface) and acts as the sample arm in the interferometer setup. The thin layer of titanium does not affect the shockwave as its thickness is smaller than the spatial disturbance of the shockwave. In fact, the amount of time it takes for disturbance to propagate through 0.04 μm Ti is approximately 7.9 ps, which is $1,000\times$ smaller than the shockwave rise time of 2 $ns \sim 6 \ ns$. The samples were prepared similarly to the samples used in the biofilm delaminations experiments. The interferometry system was shown earlier in Figure 3.8. Due to limitations in the digitizer memory, data was acquired for 200 ns with 1024 points, corresponding to a time resolution of $\sim$ 0.2 ns. This provided enough resolution to acquire enough data points for to acquire the sharp rise time of the stress pulse. After saving the raw interferogram data in the computer, the data was transferred to other software for waveform fitting and input stress calculation.
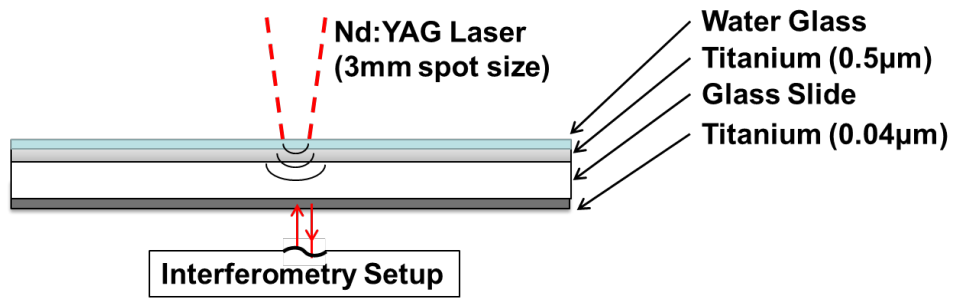
Figure 3.8: Interferometry Sample Setup: Interferometry off Glass Slide
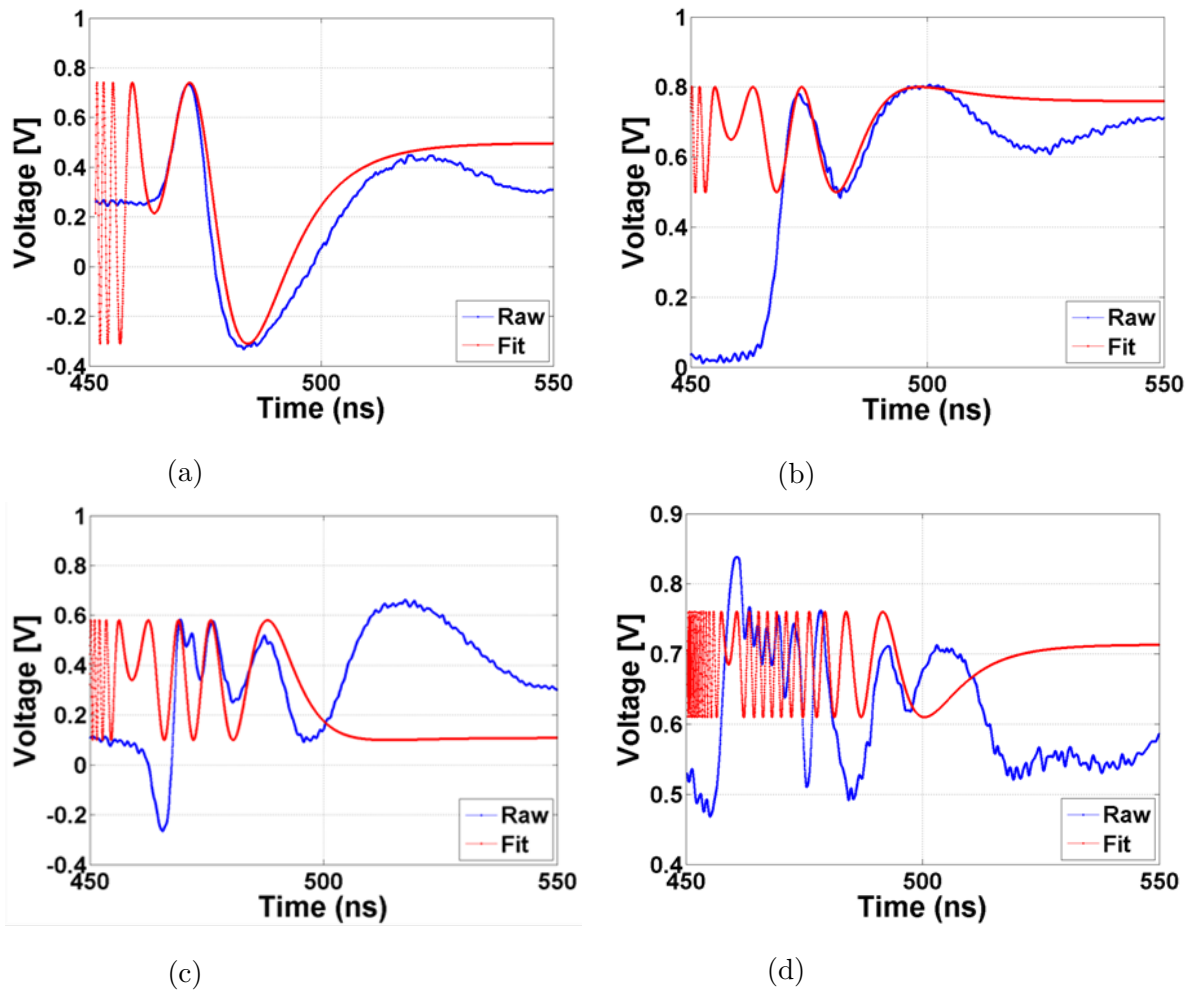
Figure 3.9: Glass raw and fitted interferograms at different fluence levels. (a) 11 mJ/mm^2. (b) 14 mJ/mm^2. (c) 30 mJ/mm^2. (d) 75 mJ/mm^2.

3.5.1.2   Interferometry Results

The interferograms, displacement, velocity, and stress profile plots were constructed from seven different fluence levels. Figure 3.9 shows interferogram fits for 4 of the 7 energy levels. The arrival of the wave is $\sim 465 \ ns$ for lower energies, and the arrival shifts earlier with increasing energy due to higher shock wave pressures. In each of those plots, the first several fringes match well to the extracted fit. Then the fit deviates from the raw data after $\sim 50 \ ns$ from the first peak. This does not affect the final results since most of the displacement information occurs within $\sim 20 \ ns$. At $46 \ mJ/mm^2$ and higher, the fringes from the interferograms start out at a lower frequency in the first fringe. Then the fringe pattern exhibits high frequency fringes for $10-15 \ ns$, and trails off (Figure 3.9d). This phenomenon is inherit in glass modified stress wave due to the fact that glass becomes more compressible at higher peak stress. As a result, the rise time tends to become longer whereby more of a rarefaction shock is developed as evidence at higher energy fluence. It is important to note that Figure 3.9d shows a fit data that does not match the raw interferogram. In an ideal case, if the interferometer system is free from vibrations in the environment and due to shock loading, the waveform amplitudes would be the same. However, this does not occur since the sample will move during the laser-

Table 3.1: Curve fitting constants 'α','β' & 'γ' off glass slide and petridish samples by the displacement interferometer. These parameters are used to define the displacement function 2.10 and to calculate the input stress function A.11.

		Energy Fluences [mJ/mm^2]						
		11	14	30	46	59	75	93
	α	8.6	8.6	8.6	8.6	8.996032	7.87	7.87
Glass Slide	β	8.3	8.3	8.3	8.3	8.35249	7.37	7.35
	γ	1150	2500	4000	5450	3244.239	7000	7400
	α	33.16	33.15806	33.16	33.16	33.16	33.16	33.16
Polystyrene	β	4.367	4.36725	4.37	4.37	4.4	4.37	4.37
	γ	26	29.8	39.5	55	58	65	68

ablation process. This does not affect the results since the phase of the fitted function is of more critical importance to maintain the correct location of the peaks. In fact, the fitted function is mostly dependent on the peak and trough time positions.

Figure 3.10 shows the total displacements and surfaces velocities measured from the

(a)   (b)
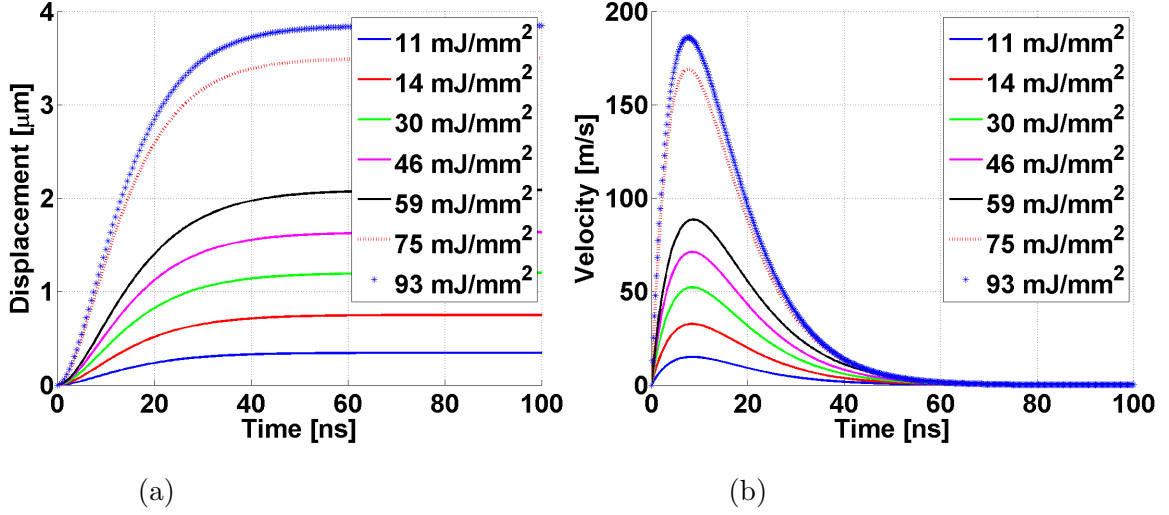
Figure 3.10: Glass displacement and velocity profiles under increasing laser fluence relationships extracted from interferometry data at seven laser fluence. (a) Total displacement profiles. (b) Surface velocity profiles.

Michelson displacement interferometer. The displacement and velocity profiles are used by plugging in the fitting parameters presented in Table 3.1 into equation 2.10 & equation 2.11, respectively. Most of the occurs 3.10a displacement occurs within $20\ ns$. Higher energy fluence ($93\ mJ/mm^2$) have total displacement ranging from $0.35\ \mu m - 3.89\ \mu m$ to peak velocities ranging $15\ m/s - 186.1\ m/s$.

Figure 3.11 shows a plot of the extracted profile stresses. From the stress plots, the rise time stays relatively consistent at $6 \sim 8\ ns$, with total pulse durations no more than $70\ ns$. The peak stress ranges from $120\ MPa$ at $11\ mJ/mm^2$ to $1.4\ GPa$ at $93 mJ/mm^2$. Peak free surface velocities of the glass range from $15\ m/s$ to $190\ m/s$. The total displacement of the glass slide has a maximum of $\sim 4\ \mu m$. The rise time to peak stress for lower energies is $\sim 6\ ns$, while at the higher energy, notably $93\ mJ/mm^2$, the peak stress occurs at $\sim 9\ ns$. The plots exhibit a sharp rise in pressure leveling off at
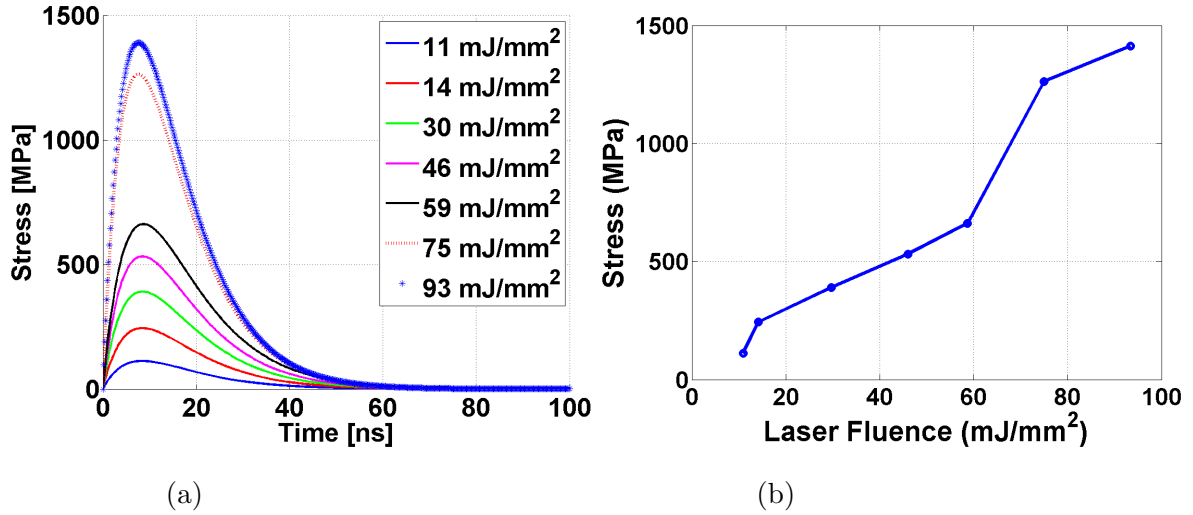
Figure 3.11: Glass input stress profiles and laser fluence relationships from interferometry data at seven laser fluences. (a) Stress profiles. (b) Peak stress for various laser fluences.

8 ns, and then a sharp drop lasting ~ 60 ns. In the study by Gupta et al. [107], the increase in fringe frequency shows an increase in velocity and stress, and the decrease in fringe frequency corresponds to a sharp decrease in velocity and stress due to rarefaction shock produced in glass. This is due to the increased compressibility of glass under higher pressure gradients. Although the interferograms display more modest increases and decreases in fringe frequency, sharp rise and drop of stresses and velocities are still observed, especially with higher laser fluence. Furthermore, Gupta et al. used aluminum as the ablation layer instead of titanium, which may explain the differences in fringe patterns. Figure 3.11b was constructed by plotting the peak stresses for all laser fluence. The fluence is calculated with an area of 7.065 mm^2 as the laser spot size (3 mm) remained fixed.

3.6   Input Stress to Analytical Model

From experimental data, an average value of the input stress is generated based on the energies used to delaminate the biofilm. To characterize the interface stress, 7 energy readings around the critical energy fluence of 30 mJ/mm^2 were used to delaminate the biofilm and also the displacement interferometer was used at each of these energies. This

energy was chosen as it is the critical energy threshold to cause biofilm delaminations. Thus as a measurement standpoint, this is the energy fluence and input stress used in the wave propagation model. An input stress used in the model is shown in Figure 3.12d. The peak stress generated is 391.6 MPa. What allows the implementation of a linearly elastic wave propagation model is the amount of displacement, or according to Figure 3.13, the amount of strain and strain rate. It can be safely assumed that the material,
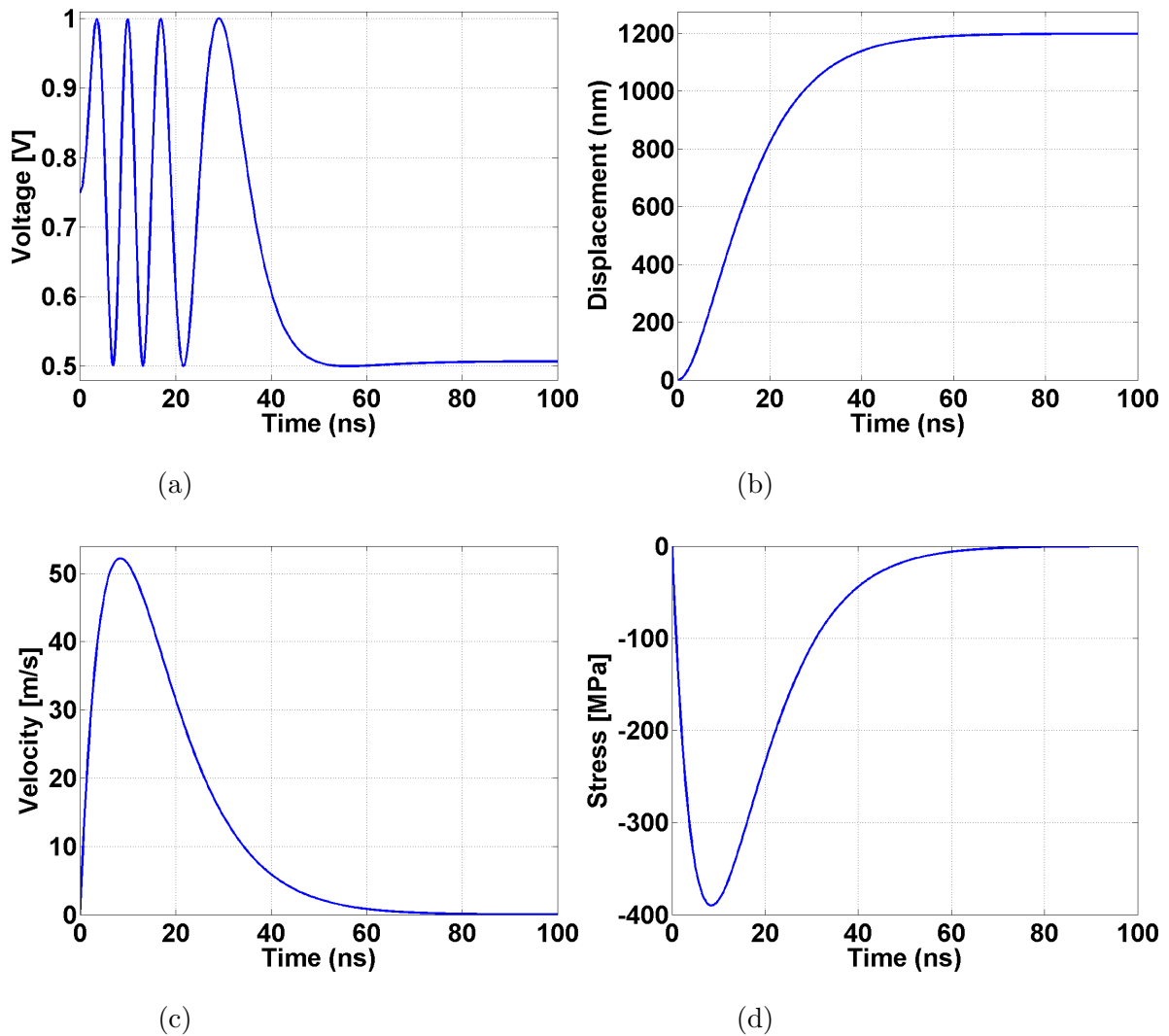
Figure 3.12: Input data used in $1-D$ Analytical Wave Model for 30 mJ/mm^2 where $\alpha = 8.6$, $\beta = 8.3$ & $\gamma = 3995$. (a) Fitted function over raw data from interferometry (b) Displacement data from interferometry. (c) Velocity profile generated from displacement data. (d) Input stress used in model.

i.e. glass slide, deforms under linearly elastic conditions. This is justified by the total strain and strain rate at which the material undergoes. The total strain and strain rate can be calculated by the following equations:

$$\varepsilon_s = \frac{2c_p}{l_s} \int_0^\tau (\varepsilon_i - \varepsilon_t) d\tau \tag{3.1}$$

$$\dot{\varepsilon}_s = \frac{2c_p}{l_s} (\varepsilon_i - \varepsilon_t) \tag{3.2}$$

where in equation 3.1, ε_s is the total strain, c_p is the p-wave speed, l_s is the thickness of the substrate, or the thickness of glass slide, ε_i is the incident strain and ε_t is the transmitted strain. The incident strain was presented before in equation 2.4. The interferometer only allows for the measurement of the incident strain and thus $\varepsilon_t = 0$.
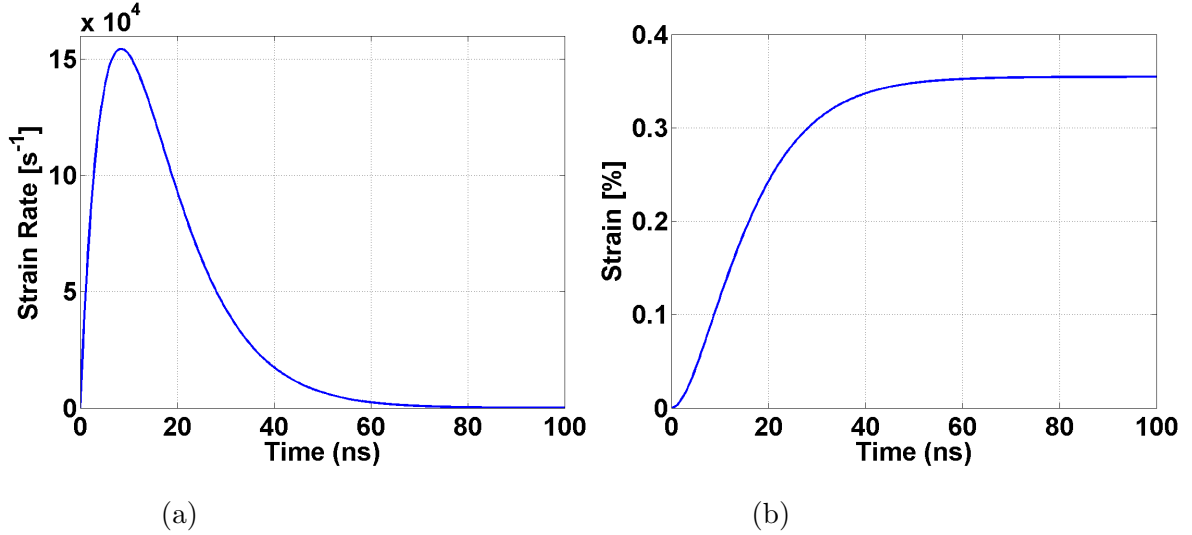
Figure 3.13: Strain rate and strain profiles due to applied input stress in Figure 3.12d in the glass slide. A peak strain rate of is measured at (a) $1.544 \times 10^5 s^{-1}$ strain rate and a (b) total strain of 0.36%.

Figure 3.13 shows the resulting strain rate (Figure 3.13a) and total strain (Figure 3.13b) in the glass slide. The total strain is less than 0.35% and the peak strain rate is $1.5 \times 10^5 \ s^{-1}$. The amount of strain is safely within the linear elastic region of the glass slide. Due to the high strain rate, it is safe to assume that any failure will be intrinsic since plastic deformation is largely suppressed [114]. It is important to note that these

loading conditions apply in the glass slide and will vary between different layers since the strain and strain rate are functions of the speed of sound of each layer and the thickness.

3.7   1-D Stress Wave Model Results

This section will present the the 1-D analytical model results. The layered models used in the analysis are shown in Figure 3.3a.

3.7.1   Mechanical Properties of Layers

The mechanical properties used in the 5-layer analytical model are presented in Table 3.2. These include the Young's modulus, Poisson's ratio and density which are all used to calculate the longitudinal wave speed in the solid. These parameters are only valid for the solid layers: polystyrene and glass slide. The PBS layer is an incompressible fluid and the Poisson's ratio is $\nu = 0.5$. This is a major issue when utilizing a solids modeling because the main parameters in a linear elastic isotropic material are Young's Modulus E and Poisson's ratio ν or *Lamé* parameters λ and μ. According to equation 3.3, as $\nu \to 0.5$, then $\lambda \to \infty$, leading to an infinite primary wave speed of sound (3.4) and infinite impedance (equation3.5). Thus the stress wave will not propagate in the model. However, this can be remedied by assuming impedance values published in literature and shown in Table 3.2 .

$$\lambda = \frac{E\nu}{(1+\nu)(1-2\nu)} \tag{3.3}$$

$$c_p = \sqrt{\frac{\lambda + 2\mu}{\rho}} \tag{3.4}$$

$$z = \rho c_p \tag{3.5}$$

The material properties for polystyrene, PBS, and glass slide are reported elsewhere [85,107]. The thicknesses of each layer, besides the biofilm, are measured by a micrometer. Biofilm wet density has been reported to be 1.00 g/cm^3 by Tsezos and Benedek [115], which is assumed to be the density of water, while Hemanowicz and Ganezarczyk reported

1.14 g/cm^3 [116]. For this model, the latter of the two is used. Longitudinal wave speeds of 1,540 m/s have been reported by Shemesh et al [117] and used in the model. Another safe assumption is to give the biofilm the properties of water whereby the speed of sound is 1,481 m/s.

Table 3.2: Mechanical properties of each material used in the 1-D Analytical Wave Propagation Model.

	Glass Slide [107]	PBS [85]	Biofilm	Polystyrene [85]
Thickness [μm]	1,000	1,000/100,000	28.49 ± 5.93	830
Young's modulus [GPa]	77.4	–	–	3
Bulks modulus [GPa]	–	2.18	–	–
Density [g/cm^3]	2.53	1.00	1.00 [115]/1.14 [116]	1004
Poisson's ratio	0.22	–	–	0.4
Longitudinal Wave Speed [m/s]	5,910	1,481	1,540 [117]	2,530

3.7.1.1 Measuring Biofilm Thickness by Confocal Laser Scanning Microscopy (CLSM)

Obtaining a measurement of biofilm thickness is difficult due to its non-uniform structure. A CLSM (Leica Confocal SP1 MP-Inverted, UCLA-CNSI) is used to measure an average biofilm thickness. The microscope allows the capability of obtaining cross-sectional images of the biofilm structure and rebuilding the images into a 3-dimensional landscape. The microscope is able to obtain depth information by utilizing a pinhole to effectively

(a)   (b)
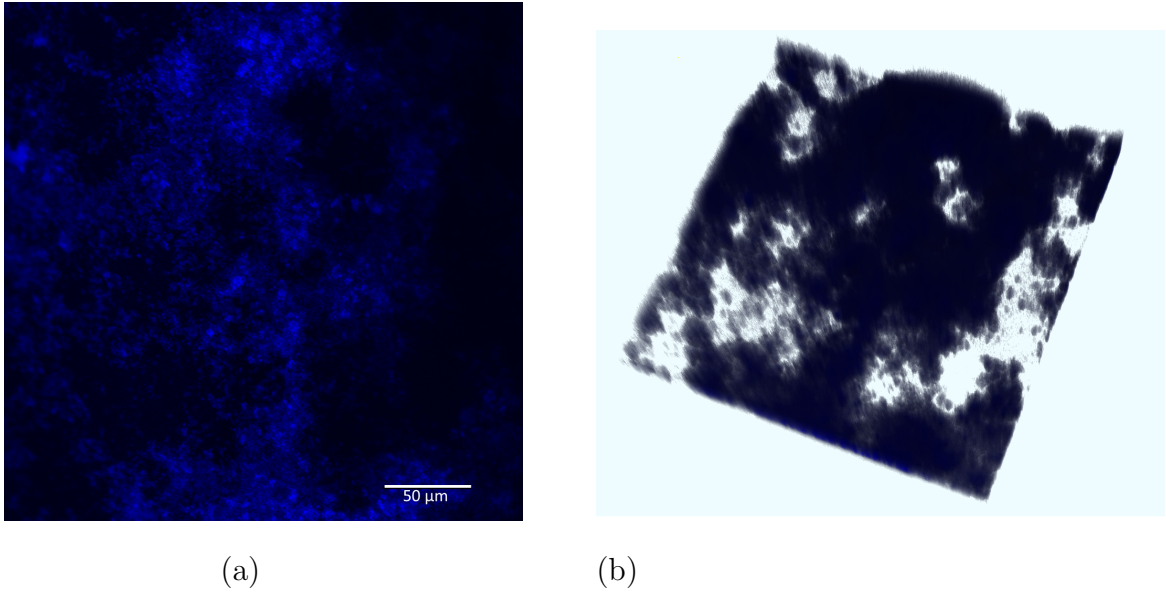
Figure 3.14: *S. epidermidis* biofilms after 24 *hr* growth. (a) A single cross section of the biofilm. (b) Rotated composite images of all z-stack cross sections.

filter out any out of plane fluorescent light.

Polystyrene coupons were cut to $3\ inch \times 1\ inch$ dimensions and placed in $100\ mm \times 15\ mm$ petri dishes. The samples were immersed in solution with *S. epidermidis* in trypticase soy broth to an Optical Density (OD) = 0.2, corresponding to a cell density of $\sim 4.77 \times 10^7\ CFU/mL$. After 24 hours of growth, samples were then stained with a fluorescent dye (WGA, Alexa Fluor® 633, Invitrogen Corp.) that binds to the polysaccharides secreted by the bacterial cells. The dye works in the infrared with an excitation wavelength of 632 *nm* and an emission wavelength of 647 *nm*. Z-stack images were taken at 10 random locations on the biofilm. The thickness of each cross section was $\sim 3\ \mu m$. Figure 3.14a shows a single z-stack slice of the biofilm cross section while Figure 3.14b shows the a composite image of all the z-stacked images. It is evident how non-uniform the biofilm structures grow. To obtain physical thickness measurements, COMSTAT v1.1 is utilized to average the biofilm thickness and results are presented in Table 3.3. The software evaluates each z-stack cross section and calculates, after manual thresholding, the fluorescent volume of pixels. Since the pixel dimensions are known from the CLSM, an overall average thickness measurement can be collected. Further details of the software are presented elsewhere [118].
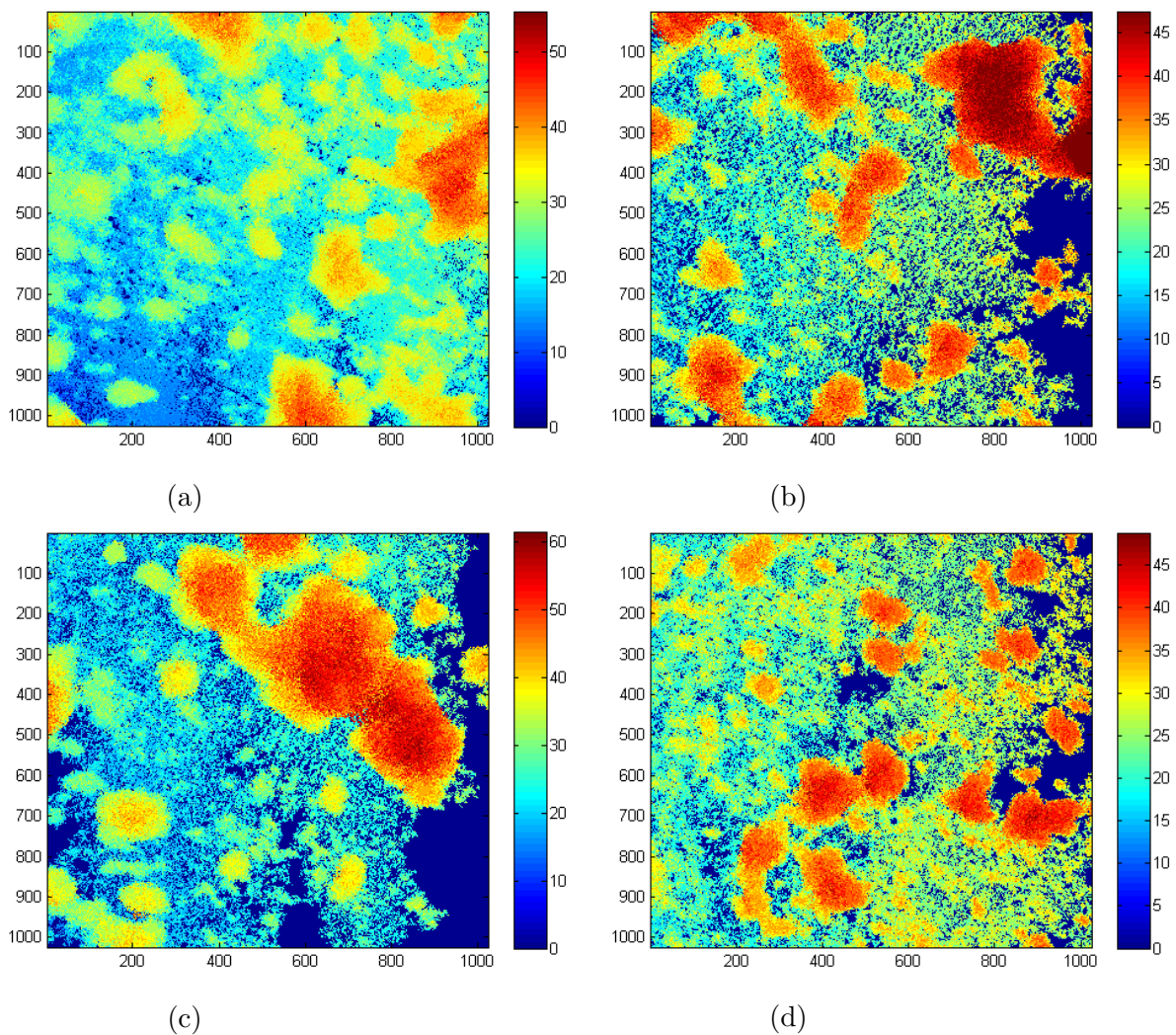
Figure 3.15: Color intensity maps showing distribution 3-dimensional biofilm structure at randomized locations as shown in Table 3.3: (a) Sample 1. (b) Sample 8. (c) Sample 9. (d) Sample 10. Color code bar is arbitrary and normalized whereby a higher intensity values corresponds to thicker biofilm biofilm and lower intensity corresponds to thinner biofilms. Scale numbers correspond to pixel location (1024×1024 pixel area). Pixel size is $0.244\mu m \times 0.244\mu m$ and a z-stack thickness of 3.25 μm and there are a total of 20 z-stack measurements.

Table 3.3: Biofilm thickness measurements from *COMSTAT v1.1*

Sample Location	Avg. Thickness [μm]
1	24.9
2	41.89
3	32.16
4	31.23
5	29.11
6	28.39
7	25.45
8	21.19
9	28.35
10	22.2
Total Avg.	$28.49 \pm 5.93 \ \mu m$

3.7.2 Interface Stress History

The stress history of the biofilm-polystyrene interface is shown in Figure 3.16 for sample 7 in Table 3.4. Because of the large impedance mismatch at the glass-water interface in Figure 3.3a, a train of pulses is generated into the model. In fact, at the first glass/water interface, there is a transmittance of 18% in stress amplitude. As a result, the input peak stress of 391.6 MPa reduces to 70.6 MPa. The first compressive peak arrives at the biofilm polystyrene interface at 871.6 ns and a stress amplitude of 82.84 MPa. Subsequent 2nd and 3rd compressive peaks arrive at peak $1,210 \ ns$ and $1,549 \ ns$ with stress amplitudes of 65.54 MPa and 43.79 MPa, respectively. The time difference in the compressive pulses is equal to $\sim 338 \ ns$, and is precisely the time it takes the stress wave to arrive at the glass/water interface and back into the input stress boundary condition.

The first tensile pulse arrives at the polystyrene and biofilm interfaces arrives at $1,528 \ ns$ with a peak tensile stress of $\sim 22.86 \ MPa$. This is precisely the amount of time it takes the 1st compressive wave to travel through all layers until reaching the polystyrene/water-bath interface and back to the polystyrene/biofilm interface. There
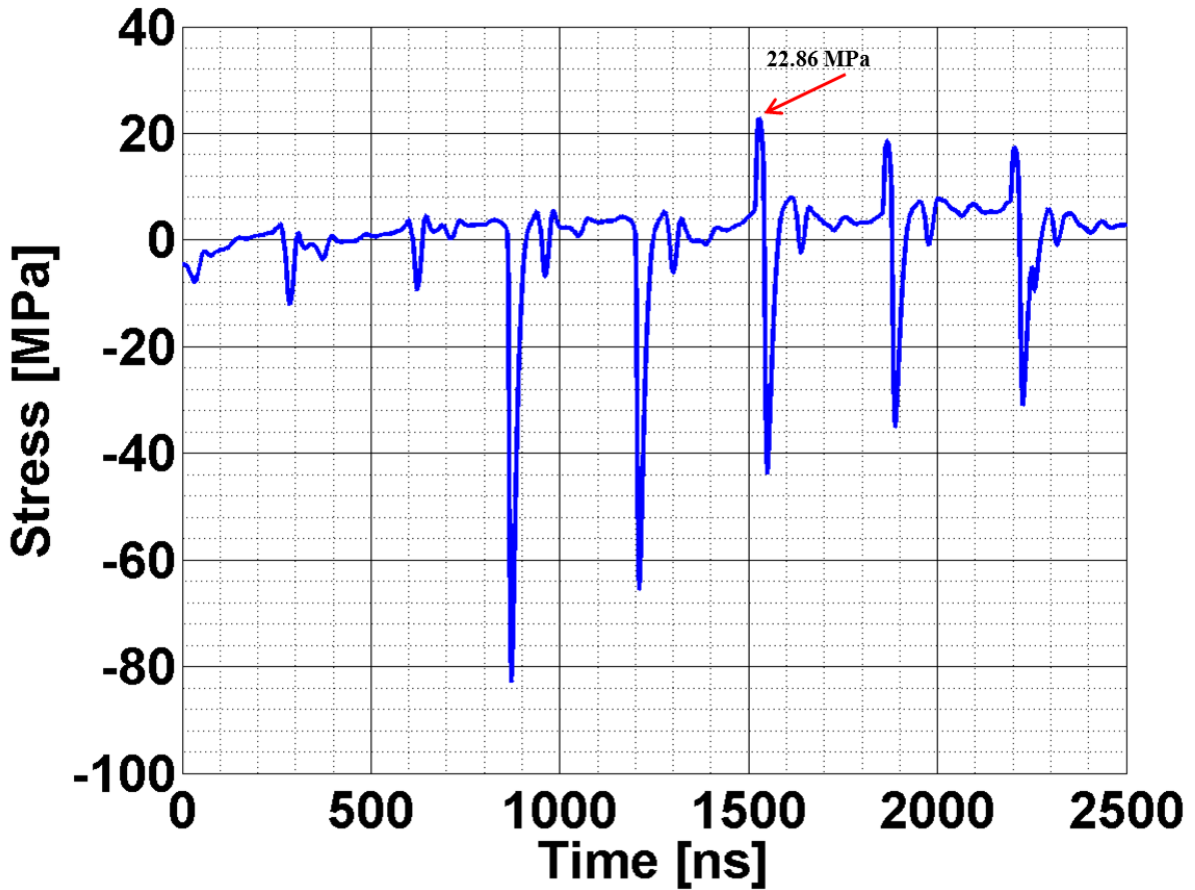
Figure 3.16: Interface stress history at the biofilm and polystyrene interface for energy fluence of 30 mJ/mm^2. Input stress to the model is shown in 3.12d. The first tensile peak is 22.86 MPa arriving at $1,528$ ns. The fitting parameters are $\alpha = 8.6$, $\beta = 8.3$ & $\gamma = 3995$.

exists a larger tensile stress component at the polystyrene/water bath layer since water layer has a lower impedance. Because the wave experiences and lesser impedance with the water-bath layer, the wave will reflect back as a tensile wave and approach the biofilm-polystyrene interface. Thus, according to the wave propagation model and the material properties used in the model, the adhesion strength of the biofilm onto the polystyrene is 22.86 MPa. This is the critical stress that caused delamination and thus it is measurement of the adhesion strength of the biofilm to the polystyrene surface. More samples were qualitatively tested and the laser fluences were used in the modified Laser Spallation Technique. Results are shown in Table 3.3. The biofilm has an average adhesion strength equal to 22.75 ± 0.16 MPa.

Table 3.4: Analytical Model results with varying experimentally acquired stress inputs. [Variance=1σ]

| Sample | α | β | γ | Peak Stress | Interface stress |
	[ns]	[ns]	[m/s]	[MPa]	[MPa]
1	8.6	8.3	3925	383.3	22.46
2	8.6	8.3	3950	385.7	22.6
3	8.6	8.3	4000	388.1	22.81
4	8.6	8.3	3975	389.6	22.75
5	8.6	8.3	4010	390.1	22.95
6	8.6	8.3	3990	390.6	22.84
7	8.6	8.3	3995	391.6	22.86
Average			3977.86 ± 2.97	388.43 ± 2.97	22.75 ± 0.16 **MPa**

3.7.3 Analytical model resolution analysis

It is important to obtain the correct tensile stress profile from the model. This is highly dependent on the input parameters to the Matlab script of the $1-D$ Analytical Stress Wave model presented in the Appendix A. It is necessary to define the time step to the analytical model in order to have enough temporal resolution to define the input stress, i.e. the maximum tensile stress must be preserved. Also, the model must run long enough to allow the stress wave to propagate through the different layers. Drawbacks to having a higher temporal resolution will not only have a higher calculation time, but it can also lead to an infinite, and non-convergent solution to the model. Table 3.5 shows the resolutions that are calculated by dividing the total run time of the code T by the number of points NP. Time resolutions $> 0.3\ ns$ had converged solutions but with poor resolution, i.e. the input peak stress was not correct. Resolution points $< 0.2\ ns$ had solutions that did not converge at all. The boxed resolution of $0.3\ ns$ corresponding to a total run time of $5\ \mu s$ provided enough temporal resolution to define the input peak stress and it also enough run time for the waves to reach the polystyrene/biofilm interface. The model yielded a convergent interface peak stress.

		No. of points, NP			
		2^{12}	2^{13}	2^{14}	2^{16}
	$\delta T = T/NP$	4096	8192	16384	65536
Total Time, T $[\mu s]$	0.5	12.2 ns	61 ps	30.05 ps	7.63 ps
	2.5	0.6 ns	0.3 ns	0.1 ns	38 ps
	5	1.22 ns	0.61 ns	0.3 ns	76.3 ps
	50	12.2 ns	6.1 ns	3.05 ns	0.763 ns
	500	122 ns	61 ns	30.05 ns	7.63 ns

Table 3.5: Analytical model time resolutions.

3.8 Shockwave Characterization: Polystyrene

The goal of this section was to find the propagated stress into the polystyrene and waterbath layer. In the second setup, a water coupling layer and a polystyrene layer were added to the original configuration. The interferometry data was taken from the polystyrene as this type of plastic was used to grow the biofilm in the biofilm disruption experiment. This setup allows estimation of the stress experienced by the biofilm in this top down phenomenology.

3.8.1 Materials and Methods

The glass slide was placed inside a polystyrene petridish. Two pieces of tape with 1 mm thickness supported the glass slide, and water was added in between the glass and the petridish for coupling. The reflective free surface was on the bottom of the Petri dish. Figure 3.17 shows the interferogram plots at selected energies. The pattern follows similarly to the interferograms for glass slides. The fringe frequencies, however, are much slower and extend much longer time before the tensile waveform takes over. For the glass interferograms, the ranges of compressive stress waveforms last from 20 ns at lower energy to 40 ns at higher energy. For polystyrene interferograms, fringes were observed to last from 50 ns at lower energy to 100 ns at higher energy. This may be the result of
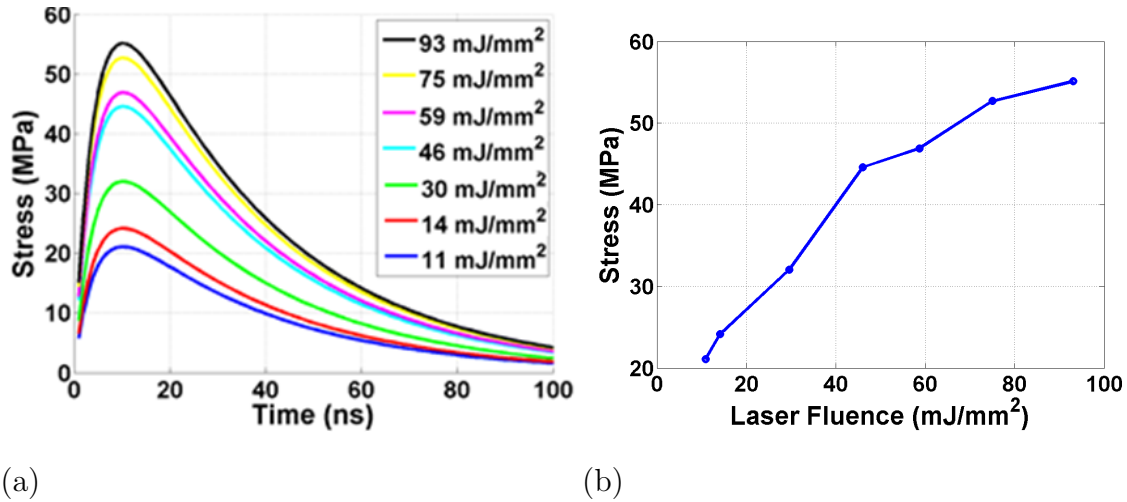
Figure 3.17: Polystyrene input stress profiles and laser fluence relationships from interferometry data at seven laser fluences. (a) Stress profiles. (b) Peak stress for various laser fluences.

the $1mm$ of water coupling, as attenuation or scattering of the acoustic wave and other effects may significantly reduce the intensity of the shock wave arriving at the polystyrene interface.

The stress plots in Figure 3.17a show the peak stresses for the laser energies used and are much lower than that of glass. Figure 3.17b again shows the peak stresses at different laser fluence. The highest energy used for the laser setting in the biofilm disruption experiments was $658\ mJ$, or $93\ mJ/mm^2$. This gives a peak stress of $55\ MPa$ at the interface of the biofilm layer. Previous studies show that the minimum pressure that causes cell damage is from $50 - 100\ MPa$ [119, 120], and our result is within the damage threshold. The profiles approximate the compressive pressure the cells are experiencing during the shock wave, and allow correlation between stress and energy used. For instance, if $50\ MPa$ is the maximum limit for cell threshold, the laser fluence must be $< 70\ mJ/mm^2$. Knowing this, if the laser spot size is changed, the laser energy can be changed also to maintain acceptable fluence ranges.

3.9 Discussion

Jaewoo et al. successfully utilized the Laser Spallation Technique (LST) to measure the adhesion strength of mammalian cells on different substrates [85, 109, 121, 122]. In fact, the LST successfully measured the adhesion strength of chondrocytes and fibroblast cells on untreated polystyrene at 27.4 $MPa \pm 2.4\%$ and 25.8 $MPa \pm 2.9\%$ [109]. The results of this chapter showed that bacterial biofilms are comparable and are $\sim 13\%$ weaker in strength at 22.75 $MPa \pm 0.16\%$ when compared to chondrocyte cells and $\sim 20\%$ weaker when compared with fibroblast cells. In this study, biofilms are structurally more like cells embedded in the extracellular polymeric substance (EPS) that essentially act as a scaffold for the cells and allows them to adhere to surfaces. Thus the mechanism of adhesion is due to the EPS and thus the adhesion strength of the *S. epidermidis* biofilm is how strongly the EPS is adhered to the polystyrene surfaces under static conditions. This adhesion mechanism has been verified by Cense et al. [1] but with a different bacterial strand.

Currently, there are no measurement techniques that intrinsically measure the adhesion strength of biofilms. As discussed Chapter in 2.4, most techniques apply loads under hydrodynamic conditions by shearing the biofilm. Thus, it is difficult to load the biofilm under uniaxial conditions. Also, due to the viscoelastic nature of the biofilm, there are discrepancies of published material properties at lower strain rates.

3.9.1 Glass-modified stress waves

Glass modified stress waves do not appear to be an ideal material to generate stress waves in order to rid biofilms off surfaces for two reasons: (1) The impedance difference between glass and water has a transmittance in stress amplitude of 18% and (2) glass is a very stiff material and is not an ideal material to use over non-planar surfaces. However, glass-modified stress are beneficial in that they sustain high compressive yield stresses. Thus the amount of coupling stress could still be potentially higher compared to materials with better acoustic impedance but lower yield stresses. Another advantage of using glass-modified stresses that a single laser pulse effectively delivers a train of pulses, albeit with

lower stress subsequent stress amplitude, toward the samples as seen in Figure 3.16. The benefit of using these types of stress waves is two-fold. One, qualitative results of Figure 3.7g show a cleaner more delaminated area under higher stress. As a result of generating higher peak stresses, more of the shocked area provides enough tensile stress to effectively delaminate the biofilm. To this end, the ensuing train of stress waves also yield enough of the tensile stress. Second, the compressive train of pulses could potentially deliver more drugs, i.e. antibiotics or across membranes macromolecules as discussed in section 2.3.4.2 of Chapter 2 [71–74, 76, 78, 81, 82].

3.9.2 Biofilm Strain and Strain Rates

The total input strain and strain rate to the biofilm layer can be found by implementing equations 3.1 and 3.2 and shown in Figure 3.18. A high peak strain rate of $1.41 \times 10^6 \ s^{-1}$ and a total strain of 3.1% are achieved. It must be noted that this is only the input strain to the biofilm layer. Transmitted strains could not be simultaneous calculated. However, the values reported are at the maximum achievable values. Körstgens et al. tested *P. aeruginosa* under uniaxial compression by utilizing a film rheometer [96]. Results show that strains below 5.0% were not measurable due to device limitations. Strains between $5\% - 15\%$ (up to cohesive failure), the biofilm follows a linear Hookean solid. A Young's modulus value of $E = 6500 \pm 500 \ Pa$ was reported. However, due to the slow loading and ultimately slow testing rates, the biofilm has enough time to respond to the applied forces since the biofilm is a viscoelastic solid [1]. This explains discrepancies observed in the mechanical properties presented in (Table 2.1). The total strain due to laser generated shockwaves achieve high strain rates, thereby effectively not allowing for a viscoelastic response of the biofilm, and the calculated strain of 3.1% is lower than the failure strain reported by Körstgens at 15% under compression, and an average 54% failure under tension by Aggarwal et al. [97]. Aggarwal did report a strain rate dependence of *S. epidermidis* biofilms. In fact, under lower strain rates $(0.01 - 1.3 \ s^{-1})$, the biofilm stiffens and the ultimate strength of cohesive failure, under tension, and Young's modulus both increase when measured by a microcantilever device. What is interesting to note is that

the biofilm structure has weaker cohesive forces when compared to the adhesion strength. Thus, it is impossible to achieve complete adhesive failure at the substrate interface since the biofilm will first approach cohesive failure. At higher strain rates, up to 9.1 s^{-1}, the elastic modulus levels off to ~ 0.01 MPa. Strain rates higher than 9.1 s^{-1} are not reported and thus material properties of biofilms under these strain rates are needed. Moreover, Klapper et al. suggested that biofilms stiffen and respond elastically under tension on short time scales while at longer time scales, viscous flow occurs [94].

(a)   (b)
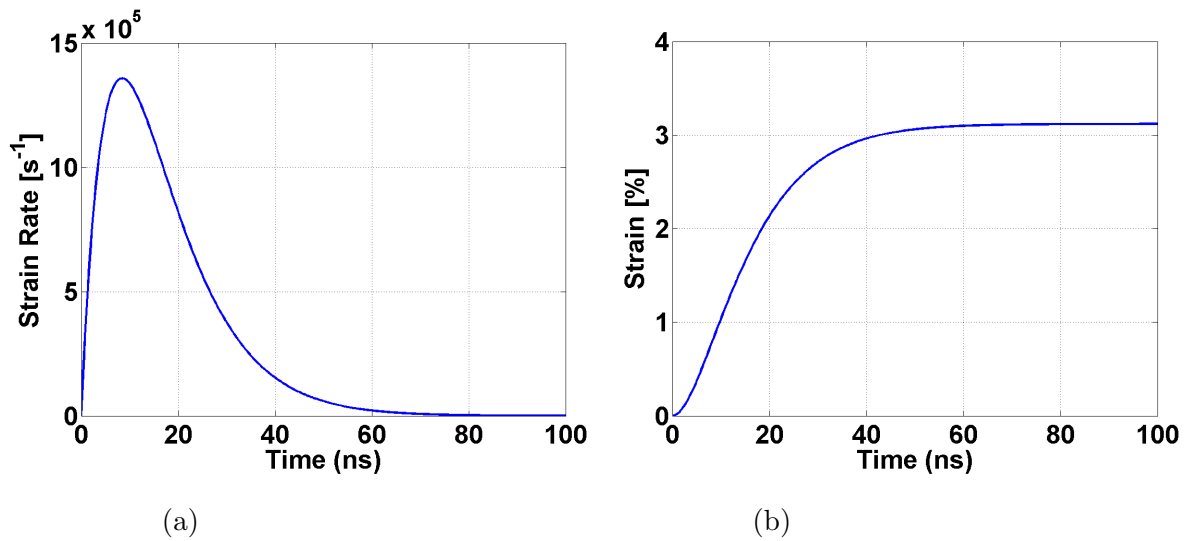
Figure 3.18: Input strain rate and strain profiles into biofilm layer. A peak strain rate of is measured at (a) 1.41×10^6 s^{-1} strain rate and a (b) Total strain of 3.1%.

3.10   Conclusions

This chapter explored the used of laser-generated schockwaves as a means to delaminate and measure the adhesion strength of *S. epidermidis* biofilms. The following conclusions are made:

1. A modified version of the Laser Spallation Technique was built and successfully used to quantify the adhesion strength of *S. epidermidis* biofilms on polystyrene under static conditions. The adhesion strength of was measured using glass modified stress waves were successfully generated and measured by a displacement interferometer.

2. A laser fluence of 30 mJ/mm^2 is needed to achieve delamination of *S. epidermidis* biofilms grown on polystyrene under static conditions. The corresponding input stress wave generated had an average peak input stress into the glass slide of $388.43 \pm 2.97\ MPa$.

3. According to the $1 - D$ analytical wave propagation model, the adhesion strength of the biofilm is calculated to be $22.75\ MPa \pm 0.16\%$

4. Higher energy fluences lead to higher peak stresses and rarefaction shocks. This lead to more of the shocked area to have the critical tensile stress to cause more delaminations

5. High strain rates of $1.544 \times 10^5\ s^{-1}$ and $1.41 \times 10^6\ s^{-1}$ in glass and in biofilm, respectively were measured. Total strains of 0.3 % in glass and 3 % in the *S. epidermidis* biofilm are measured, thereby safely loading the material in the linear elastic region. The high strain rate loading suppresses any plastic deformation and since there is pure tensile loading, the decohesive failure is a purely intrinsic measurement and independent of the geometry of the biofilm being tested.

CHAPTER 4

The effect of glass-modified shockwaves on porcine tissue

Chapter 3 presented the use of laser generated shockwaves to not only rid biofilms off polymeric surfaces, but also characterize the adhesion strength of biofilms *in vitro*. By increasing the energy fluence, more of the shock loaded area achieves the critical stress threshold. However, higher generated peak stresses must be well characterized since materials can undergo compressive or tensile failure. As a treatment modality, laser generated shockwaves prove to be beneficial as described in detail in Chapter 2.3.4.2. A more improved *ex vivo* model would be to see the effect of laser-generated shockwaves of biofilms grown on biotic surfaces, i.e. skin or wound surfaces. The skin *ex vivo* model is more difficult to implement since bacteria need an incubation period, a process that can potentially denature and affect the skin's properties. As a result, the wave propagation will be affected. Infected wound models prove to be more ideal. However, the laser delivery systems are bulky and can not be translated to surgical operation rooms.

The purpose of this chapter is to explore the direct mechanical effect of the glass modified stresses on the structural changes in porcine tissue *ex vivo*. It is important to establish damage thresholds of the shockwaves on tissue. Ultimately, the laser generated shockwaves will be implemented as a technique to treat infected wounds. Typically in infected wounds, bacterial biofilms reside on the surface of not only necrotic but also healthy underlying tissue. Thus it is of critical importance to deliver mechanical shockwaves that would target and disrupt the biofilm, i.e. by either delamination and/or deliver drugs, while at the same time not damaging underlying healthy tissue. Preliminary studies will explore the direct mechanical effect of shockwaves on tissue.

4.1 Introduction

The use of laser-generated shockwaves as a technique to rid biofilms off of biotic and abiotic surfaces is of critical importance. The goal of this study is to understand the direct effect of shockwaves on fresh porcine tissue. As discussed in the Chapter 2.3 chapter, laser generated shockwaves have been shown to permeabilize cells [71–74] and deliver macromolecules, permeabilize skin and even permeabilize biofilms [75, 76, 80]. When antibiotics are coupled with shockwaves, a killing effect of bacteria within the biofilm structure is achieved [81, 82]. The underlying structures that biofilms reside on have been shown to not be damaged [79] under the stress waves. In fact, Doukas and Kollias showed effective drug delivery through the stratum corneum and the propagating wave did not create any pain due to the spatial time scales of the stress disturbance [123]. This chapter will present the purely compressive mechanical effect of using glass-modified shockwaves.

4.2 Current state of knowledge

Physiologically and anatomically, porcine skin is very similar to human skin and have been used as models for drug delivery across skin [124–126]. The role of skin is of vital importance to protect humans from any physical and chemical hazards and even preserves internal body water loss [126]. Skin has been shown to be a vital pathway of drug delivery and in fact, is a better localized drug delivery and avoiding the gastrointestinal tract [123, 126] Porcine skin generally consists of 3 dermal layers: (i) epidermis, (ii) dermis, and (iii) hypodermis and shown in Figure 4.3. The outermost layer of the epidermis is the statrum corneum (SC) and is the primary line of defense to molecular transport. It is composed of corneocytes (dead cells) that lack nuclei and cytoplasmic organelles and are filled with keratin. Corneocyte dimensions are typically 30 μm in length and $0.5 - 0.8$ μm in thickness [123]. There are about $10 - 50$ of theses cell layers that make up the SC and with typical spacing of 20 nm between cells.
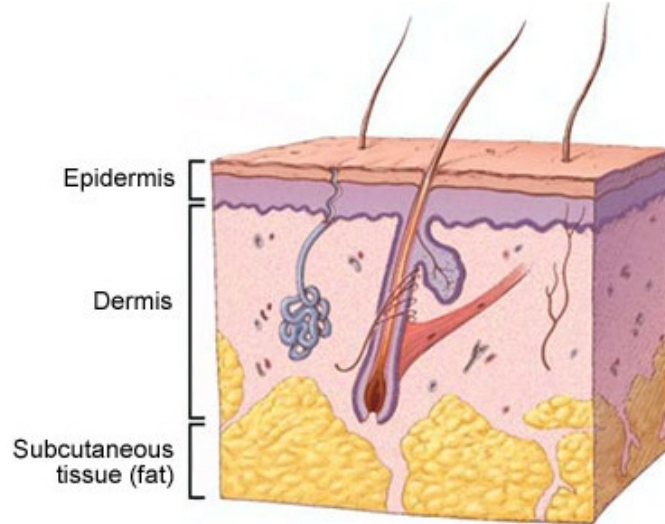
Figure 4.1: Cross-section view of basic layers in human skin. Image inspired by [127]

4.2.1 Porcine tissue mechanics under dynamic loading

Porcine tissue behaves as an orthotropic, non-linear and hyperelastic material [128]. To date, there only exists published work on the dynamic testing of porcine belly tissue in 2 of the 3 orthotropic directions: tissue tested perpendicular to the porcine spine and parallel to the spine. Lim et al. utilized a split Hopkinson Tension Bar (SHTB) under uniaxial tensile loading in two directions [128]. Maximum high strain rates up to $3.5 \times 10^3 \ s^{-1}$ were achieved. Results show that pig skin is strain-rate sensitive and the mechanical response of the tissue along the spine direction stiffens at lower strain rates while there is strain rate independence of the tissue along the perpendicular direction. Shergold et al. [129] studied the porcine tissue response under dynamic uniaxial compression. Strain rates between $1.5 \times 10^3 - 4 \times 10^3 \ s^{-1}$ were reported. Results show that porcine tissue has greater strain rate dependence parallel to spine.

It must be noted that there does not exist any published information regarding the dynamic behavior of pigskin tissue along the third orthonormal direction that is perpendicular to the belly tissue or to the epidermis layer. This is partly due to the limitation of measuring devices that need to load and test these samples. Also, it must achieve high strain rate loading. To understand the mechanical behavior in this study, a testing device capable of generating and measuring at very high strain rates up to $10^6 \ s^{-1}$

is required.

4.3 Materials and Methods

4.3.1 Porcine Sample Preparation

Fresh porcine skin (belly) samples were immediately taken postmortem from a local abattoir and transported to the testing laboratory within 40 minutes. The samples were held in a temperature controlled container with ice. Once the samples arrived at the testing facility, the porcine samples were shaved down using standard disposable shavers to rid of any hair follicles on the skin surface. The porcine samples were cut to a 10 mm × 10 mm cross sectional area and to a uniform thickness of ∼ 1 cm. To maintain uniform thickness, cuts were made by removing the fat tissue while preserving the epidermis and dermis layers. The shocked regions were treated perpendicular from the epidermis region. Each pigskin sample was then placed atop a 100 mm × 15 mm

Figure 4.2: Fresh porcine skin delivered from abattoir prior to sectioning samples. Hair follicles were removed by standard shaving methods.

petridish that rested on a water reservoir. The purpose of the petridish served to hold the pigskin and also as a container for phosphate buffered saline (PBS) as shown in Figure 4.3b. The PBS acted as a coupling layer from the glass slide to the pigskin with a clearance of ∼ 1 mm and the water reservoir served to lower the transmission energy
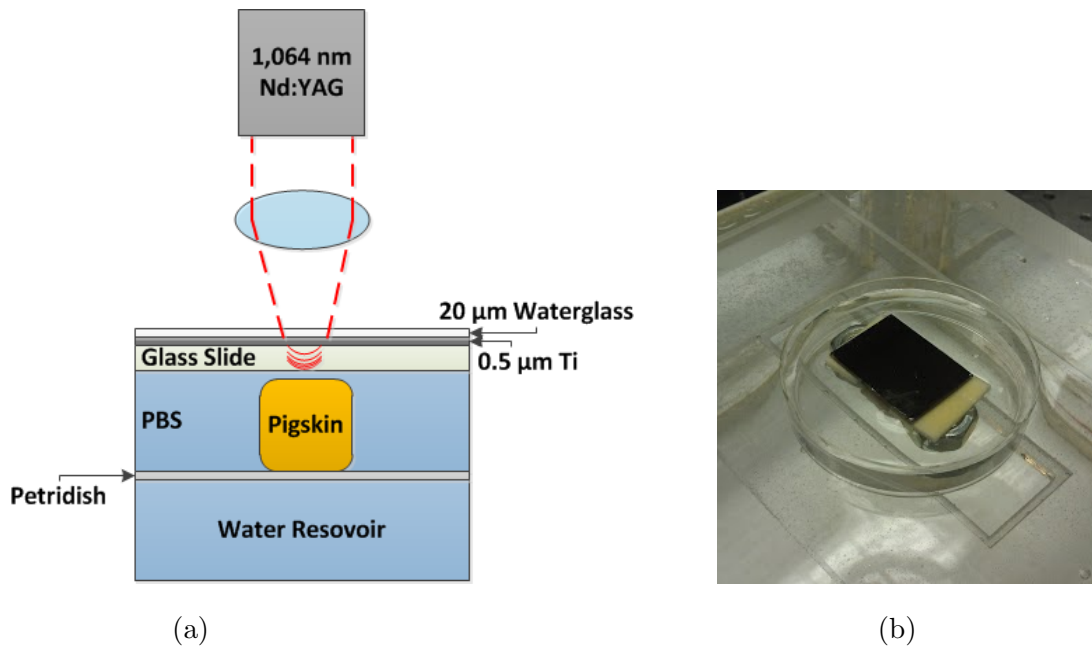
Figure 4.3: Experimental setup for shocking of pigskin device: (a) Cross-section of layers. (b) Actual experimental setup.

of the stresswave toward the tissue in tension.

The same energy fluences used to delaminate biofilms in *Chapter 3* were used to shock the tissue samples. The samples were shocked over a 3 *mm* spot size at the center of each pigskin sample. After shocking, each sample was fixed in 10% formalin, embedded in paraffin and sectioned (4 *μm* thickness) from the center of the shocked region, perpendicular to the skin surface and stained using H&E & Masson's Trichrome stains. These stains are used to differentiate between three different kinds of structures; the nucleolus of the cells, the increase in collagen in diseases as cirrhosis of the liver and the increase of muscle (smooth or skeletal) in tumors. Sectioning and staining was performed at the UCLA Department of Pathology and Laboratory Medicine. Tissue sections 4 *μm* in thickness and are taken from the center of the tissue pigskin sample, the center location of where shockwaves were applied. Keratin, muscle fibers and cytoplasm are stained red, collagen and mucin are stained blue and nuclei are dark purple.
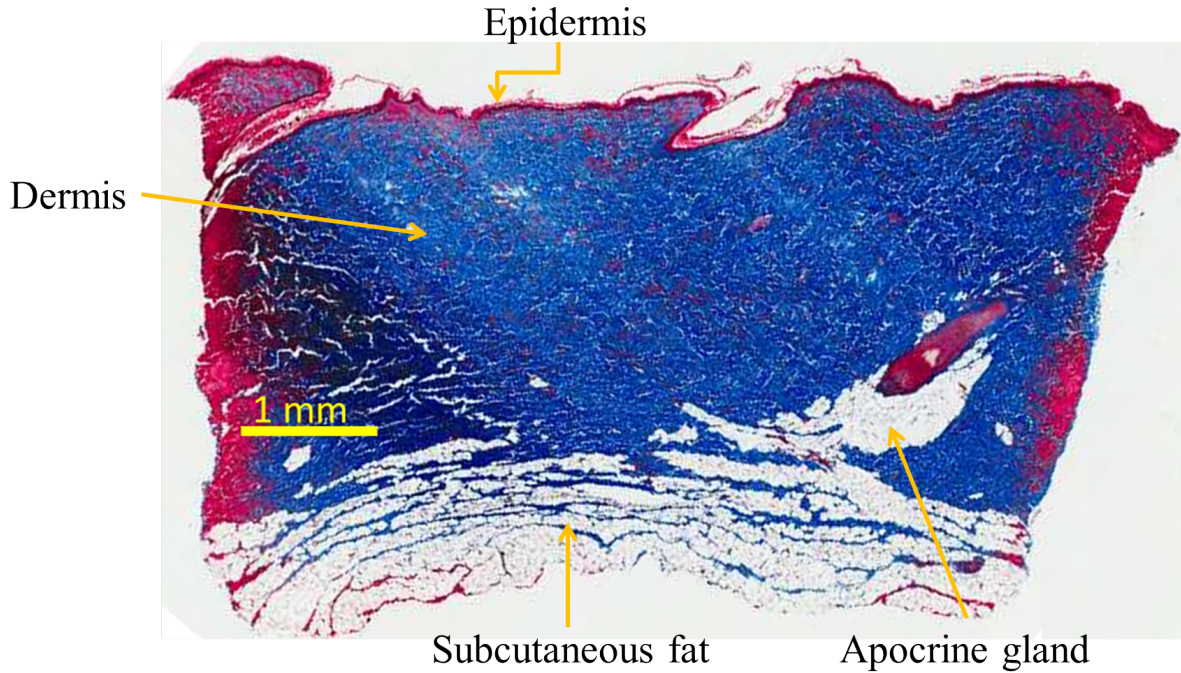
Figure 4.4: Control porcine tissue sample stained with Massons Trichrome stains. Figure show's the 3 main components of tissue. Apocrine gland is also evident and is responsible for sweat and is located between the dermis and subcutaneous fat layers.

4.4 Results

The tissue sections, including control, were viewed by an experienced pathologist in a comparative blind study. The pathologist observed no significant damage to the stratum corneum, epidermal, dermal regions and the epidermal-dermal junction. In addition, the collagen structure and orientation remains intact and no differences appear when compared to control section shown in Figure 4.4. The goal was to study the effect of our treatment on tissue structure. The physiological and inflammatory response could not be studied because only *ex vivo* samples were used. This is evident by the dead corneocytes shown in Figure 4.6. Qualitative results from the pathologists are shown in Table 4.1.

The input stresses are generated in the glass-slide are shown in Figure 4.5. However, these are not the actual stresses that propagate into the pigskin layer. The three layers involved are the glass-slide layer, the water coupling layer and finally the thick pigskin
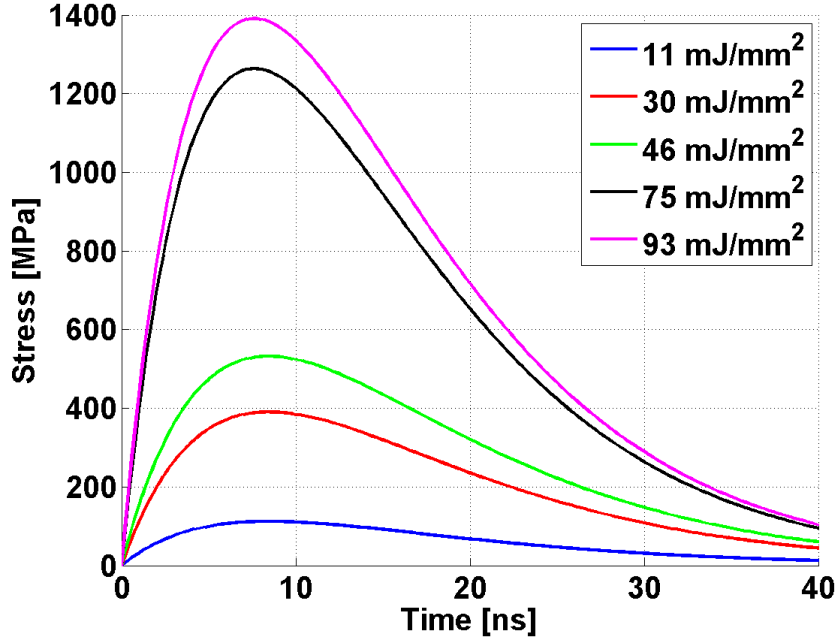
Figure 4.5: Input stresses to the glass slides.

layer and shown in Figure 4.9. Since the goal is to find the arrive of the stress into the porcine skin, it is not necessary to implement a $1-D$ analytical wave propagation model to find interface stress. This is true as long as the spatial dimensions of the layers are larger to the spatial disturbance of the stress wave. The input stress into the glass-slide can be multiplied by transmission constants as shown in equation 4.1 to ultimately obtain the input stress to the pigskin [130].

$$\sigma_3(t) = T_{12}T_{23}\sigma_1(t) \tag{4.1}$$

where

$$T_{12} = \frac{2\rho_2 c_2}{\rho_1 c_1 + \rho_2 c_2} \tag{4.2}$$

and

$$T_{23} = \frac{2\rho_3 c_3}{\rho_2 c_2 + \rho_3 c_3} \tag{4.3}$$

$\sigma_1(t)$, $\sigma_2(t)$, and $\sigma_3(t)$ are the stresses in the glass slide, water layer, and porcine skin, respectively. T_{12} and T_{23} are the transmittance coefficients from the the glass slide/water and water/tissue interfaces. $\rho_{i=1,2,3}$ is the density of each layer and $c_{i=1,2,3}$ is the speed of sound of each layer.
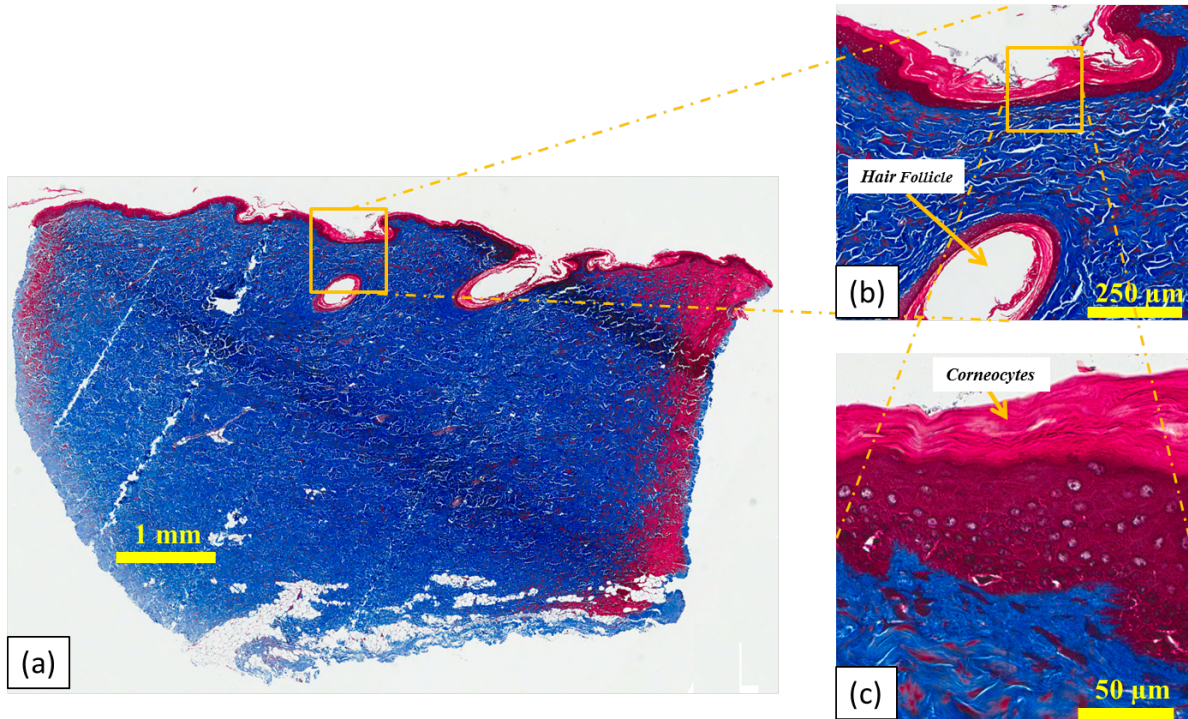
Figure 4.6: Mason's Trichrome stained pigskin at lowest laser energy 11 $\frac{mJ}{mm}$. (a) Section of pigskin at 1.4× magnification. (b) Section of pigskin at 7.6× magnification focused at epidermis (top of image), dermis (blue area), and hair follicle (hole in center). (c) Epidermis area at 7.6× magnification.

The tissue samples were subjected to the same stress waves presented in *Chapter* 2 under the varying energy fluences as shown again in Figure 4.5. The stress levels were measured by the Michelson displacement interferometer. The material properties used to find the transmitted stress waves are presented in Table 4.2. The peak compressive stresses that arrive toward the pigskin at each energy fluence are summarized in Table 4.3. The $1-D$ analytical wave propagation propagation model is also implemented to find the stress history of the water/pigskin layer to show the train of compressive waves and shown in Figures 4.10 & 4.11.

Figure 4.10 & 4.11 show the interface stress history of the glass modified stress waves after the implementation of the $1-D$ analytical wave propagation model. Due to the high impedance mismatch between the glass/water interface, a pulse train of stresses is
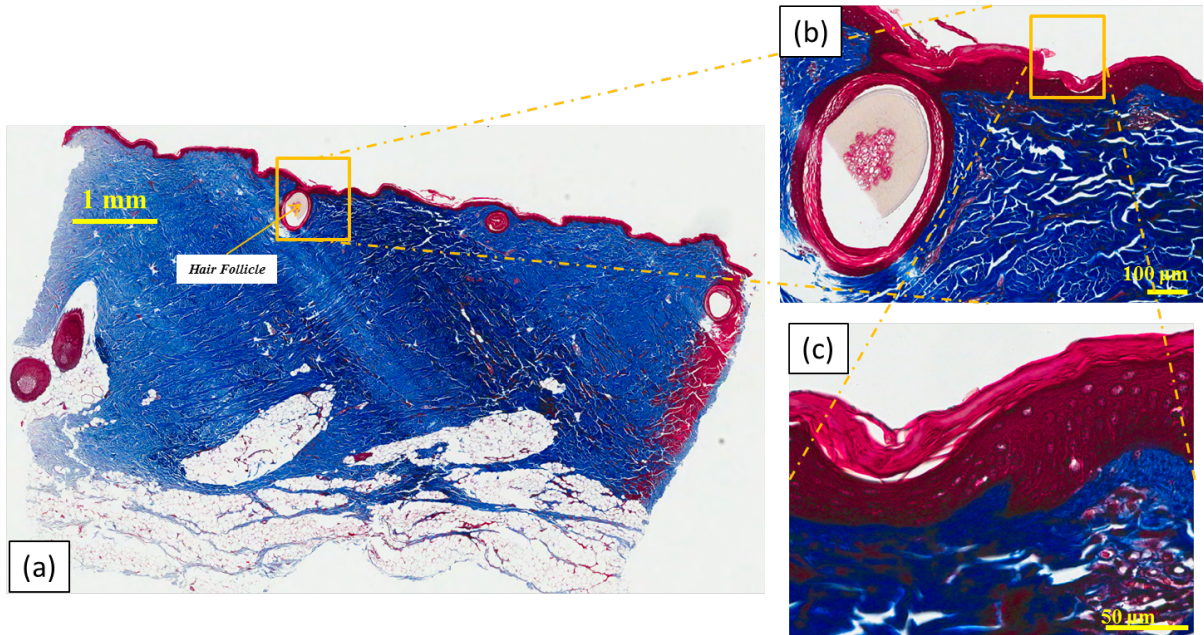
Figure 4.7: Mason's Trichrome stained pigskin at lowest laser energy 93 $\frac{mJ}{mm}$. (a) Section of pigskin at 1.2× magnification. (b) Section of pigskin at 8.8× magnification focused at epidermis (top of image), dermis (blue area), and hair follicle (hole in center). (c) Epidermis area at 40× magnification.

propagates.

4.5   Discussion

Doukas et al. showed that laser generated shockwaves (LGS) are effective in delivering drugs through the stratum corneum with only 1 mechanical stress pulse [123]. The stress profiles reported had peak stress of $35 - 100$ MPa and rise times of 100 $ns - 1$ μs. Measurement limitations of the shockwaves had minimum temporal resolution of 5 ns, a resolution not capable of measuring the $2 - 6$ ns rise time of the stress waves done in this study. Therefore the Michelson displacement interferometer is implemented. Doukas concluded that the minimum compressive stress needed to effectively deliver ~ 100 nm latex particles across the stratum corneum is 35 MPa. The effect of shockwave rise time will determine the permeability of cells. In fact, in another study by Doukas et al. [78] showed that stress wave gradient had a greater effect on cell viability than the

Table 4.1: Blind Study Results of Mason's Trichrome stained sections

Sample	Energy Fluence $[\frac{mJ}{mm^2}]$	Peak Stress [MPa]	Structural Damage?
1 (*Control*)	–	–	No
2	11	21.51	No
3	30	74.83	No
4	46	102	No
5	75	242.5	No
6	93	266.5	No
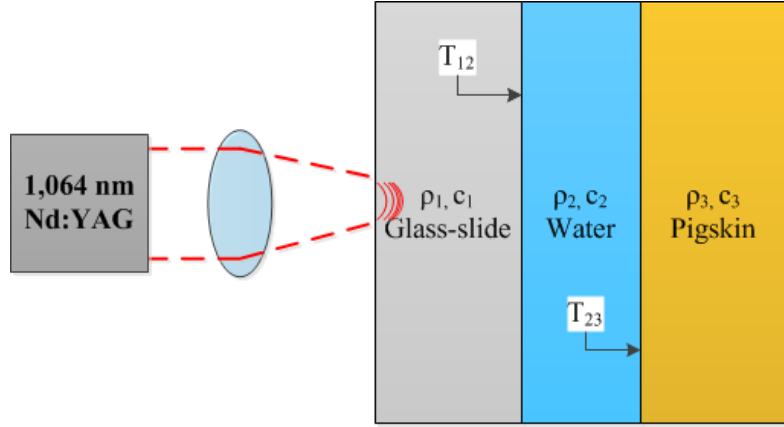
Figure 4.8: Interfaces used to calculate the transmission coefficients.

peak stress of the wave. Also, higher peak stresses and sharp rise times lead to SC permeabilization. One important thing to note is that in a study by Lee et al. explained that LGS did not cause discomfort or pain [78, 132]. Human subjects are tested by LGS. In fact, LGS with 300 ns duration did not cause any sensation where as LGS with 1 μs duration lead to sensation but not pain. LGS with 300 ns duration had no observable damage on skin while 1 μs duration LGS had some observable erethyma that was gone after $10-15$ mins. These facts prove promising to the stress waves generated in this study. The glass modified stress waves allow for sharp rise time pulses from a minimum peak stresses of 20 $MPa-266$ MPa. Also, due to the large impedance mismatch with the water coupling layer, one laser pulse on the titanium metal effectively delivers multiple pulse mechanical stresses toward the tissue. This finding will prove to
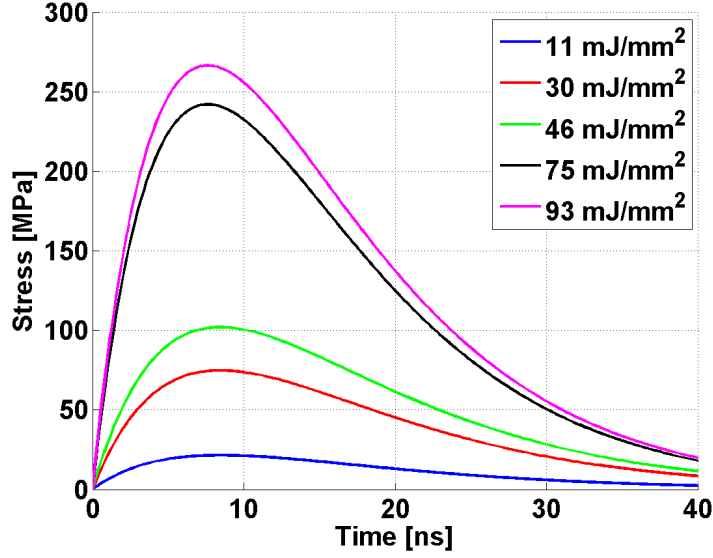
Figure 4.9: Input stresses that arrive at the water/pigskin interface according to the transmission equations.

Table 4.2: Material Properties used to calculate the transmission coefficients and stress input profiles to the pigskin.

Layer	Mat.	Dens. ρ $[\frac{kg}{m^3}]$	P-Wave Speed c $[\frac{m}{s}]$	Imped. $Z = \rho c$ $[10^3 \frac{kg}{m^2 s}]$
1	Glass [107]	2,530	5,910	14,952
2	Water [109]	1,000	1,481	1,481
3	Pigskin	–	–	1,530-1680 [123, 131]

be beneficial as a treatment modality to either deliver drugs through skin or deliver drugs into biofilms that infect wound surfaces. The effect of shockwaves on porcine tissue *ex vivo* could only be evaluated qualitatively. To date, no published material parameters of *ex vivo* porcine tissue exists under purely uniaxial tension and compression when loading is applied perpendicular to the epidermis layer. Thus in order to implement better finite-element models to understand tissue behavior under high strain rates, more information of tissue behavior have to be explored.
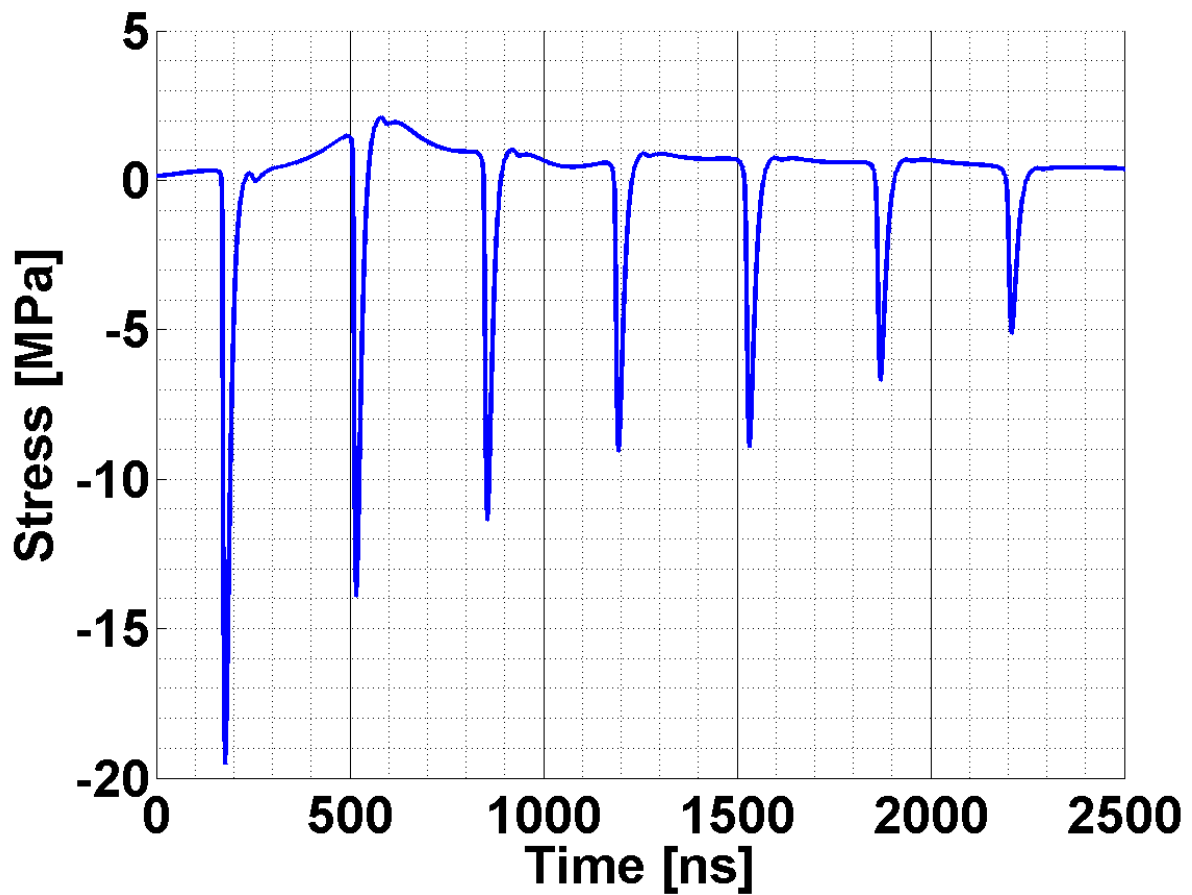
Figure 4.10: $1 - D$ Analytical Solution to the interface stress history between water and pigskin for the lowest energy fluence of 11 mJ/mm^2 as shown in Table 4.3. A train of compressive stresses is shown due to the impedance mismatch at the first interface between glass/water.
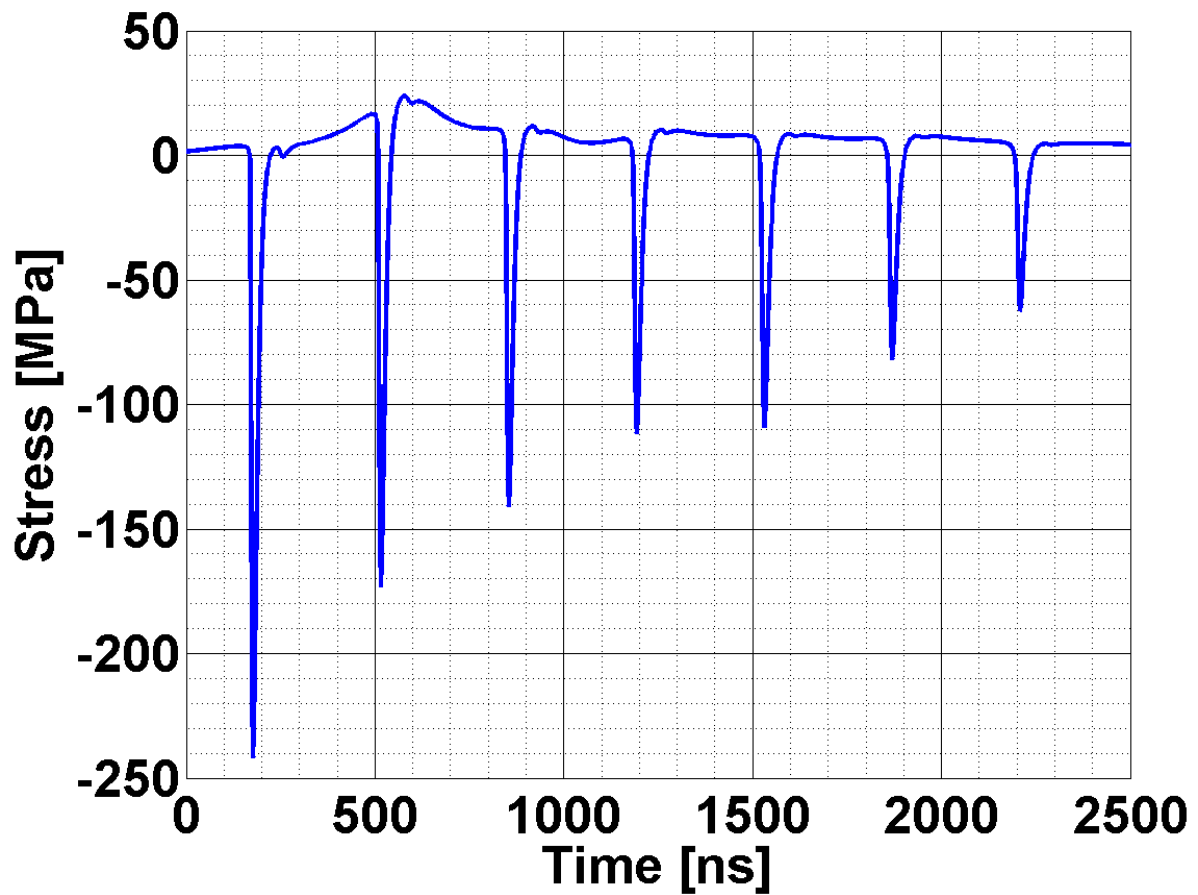
Figure 4.11: $1 - D$ Analytical Solution to the interface stress history between water and pigskin for the lowest energy fluence of 93 mJ/mm^2 as shown in Table 4.3. A train of compressive stresses is shown due to the impedance mismatch at the first interface between glass/water.

Table 4.3: Peak compressive stresses into pigskin samples. Peak stress ranges present the peak stresses at the minimum and maximum impedance values presented for pigskin in literature.

Sample	Energy Fluence $\left[\frac{mJ}{mm^2}\right]$	Peak Stress $[MPa]$
1 (Control)	–	–
2	11	20.57-21.51
3	30	71.55-74.83
4	46	97.47-102.0
5	75	231.4-242.1
6	93	255.8-266.5

4.6   Conclusion

This chapter explored the used of glass modified laser-generated schockwaves as a means to determine damage thresholds on pigskin. The following conclusions are made:

1. Glass modified stress waves were successfully generated and coupled to fresh pigskin.

2. Laser fluences from $11 - 93 \ mJ/mm^2$ generated peak stresses of $21 - 266.5 \ MPa$ that reached the water pigskin surface.

3. Due to the large impedance of glass and water, a train of compressive stress waves will propagate that vary 18% less in peak stress and spaced at 167 ns, the amount of time it takes the stress wave travels within the glass.

4. No structural damage of porcine samples were observed by a trained pathologist in a controlled blind-study of stained sections.

CHAPTER 5

High Speed Imaging System

Chapters 2 and 3 provided adhesion strength measurments of biofilms grown on polystyrene and also the effect of these shockwaves on porcine tissue. This chapter explores shockwave induced phenonmenon: cavitation. Cavitation provide secondary mechanical effects that could potentially have some affect on biofilm structures and also on tissue. In fact, cavitation bubbles were experimentally observed and caused localized areas of delamination.

5.1 Introduction

A high speed imaging system was constructed to observe shockwave effects and the extent of shockwave propagation. Since these events occurs in nanosecond to microsecond scale, a high speed imaging system is needed. High speed cameras have limitations in that the due to the longer shutter speeds, high-speed transient events become blurred. The system presented in this section allows for single-shot acquisition of shockwave phenomenon that can be compiled to generate video sequences. The limitation to the device is not due to the shutter speeds of the image systems but only in the illumination source.

High speed imaging systems can be broken into 2 distinct types. One type of system acquires a video sequence with the number of frames per second (fps) larger than $25 - 30$ hertz (Hz) rates from camcorders or webcams, producing a slow-motion event during playback at normal fps. Another type of system is to obtain frozen images of fast moving objects without image blur [133]. For the first system, frozen images of fast events are taken consecutively, which, when pieced together, may form a frame by frame process of the event. However, the images may also be taken only once per event using the second

system. If the event may be repeated, another image may be taken at another time instance during the event, and the entire event may be stitched together to form a frame by frame process, or a video sequence. The high speed method presented in this chapter is based on the second system.

The near and mid infrared region (700 $nm - 14$ μm) of light has been used to image numerous phenomenon including fluid flows, water droplets, thermal changes, and shock wave propagation [79, 134, 135]. In shock wave imaging, wave propagation photos have been acquired using shadowgraphy techniques [79]. In this work, the camera was positioned diagonally with respect to the imaging surface. The shock wave was coupled to water, and images of water surface displacement were acquired. However, instead of the shock wave traveling radially outward from the point of impact, the goal for the system in this iteration is to image the wave as it propagates toward the coupling media. Thus the camera is oriented perpendicular to the incident laser beam as displayed in Figure 5.1.

Short pulsed laser offers a desirable illumination source for high speed photography [136, 137]. However, laser systems can easily cost thousands of dollars and are often too bulky for many applications. High power light emitting diodes (LEDs), however, provide a low-cost, small footprint alternative for target illumination [134]. Patents previously filed regarding LED illumination packages [138, 139] have demonstrated the possibility of compact systems for pulsed LED based high speed imaging. The high speed imaging system in this section uses three low-cost LEDs to illuminate the target, and uses a camera coupled to a long working-distance microscope and appropriate filters to capture the reflected light.

5.2 System Assembly and Testing

5.2.1 Illumination: Diodes

The system is illuminated by three high power LEDs centered at 850 nm in a concave geometry with respect to the imaging plane. The LEDs were characterized with a contin-
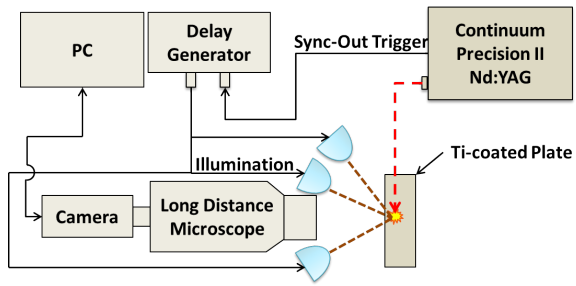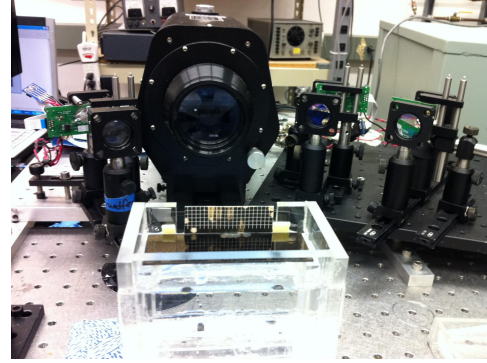
Figure 5.1: High Speed Imaging System: (a) System Diagram. (b) Image of actual system.

uous illumination at 11 ns per pulse at full with at half maximum ($FWHM$), and 9 ns for single pulse illumination, as shown in Figure 5.2. The integration time for each frame of photo is around 9 ns. Each LED has its own diode driver that requires 5 $volts$ (V) for operation. Additionally, the driver contains a feature that allows the externally controlled voltage to be specified between $0-3.8\ V$ and scales the input voltage accordingly to $0-200\ V$. This allows powerful yet efficient LED illumination. Moreover, each driver includes a trigger input, which can be activated from a delay generator controlled by a computer, thus allowing illumination control. The three LEDs are powered by a power supply and are triggered by a delay generator, with BNC cables and splitters connecting each device in parallel. Figure 5.3 shows a system block diagram of the illumination and optics. The pattern of a single LED illumination was dispersed in a rectangular shape. In order to focus the light beam, a cylindrical ($f = 20mm$) and a spherical plano-convex ($f = 20mm$) lens were placed in line with the LED. Each LED lense subsystem was mounted on a rail for easy adjustment of distances with diode, lens, and imaging plane. To increase the amount of light on the viewing plane, three identical setups were used. The light patterns on the target were overlapped for maximum illumination.
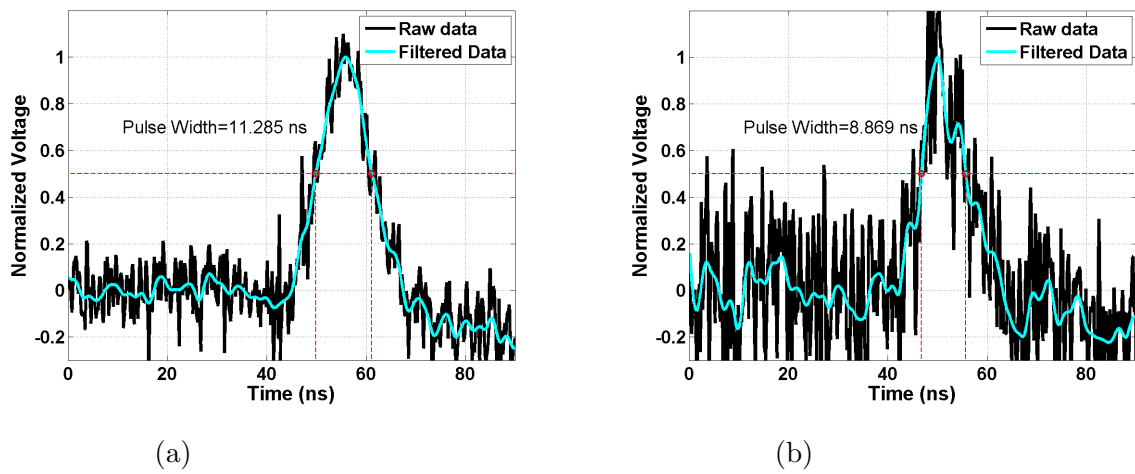
Figure 5.2: LED Pulse Width: (a) Continuous and (b) Single pulse.
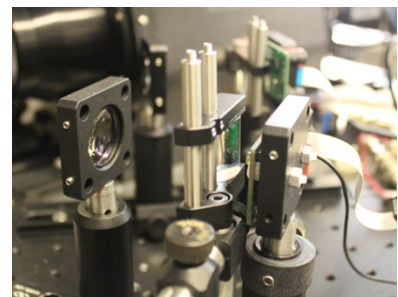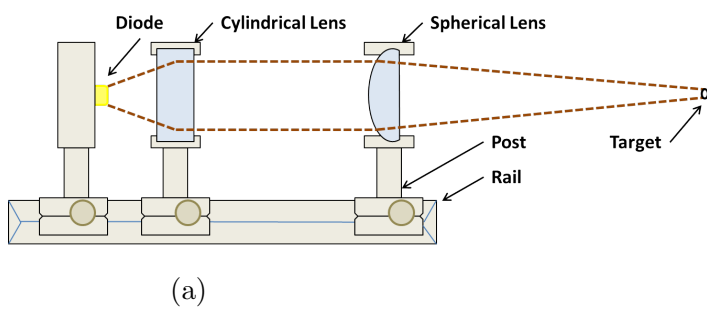
Figure 5.3: Optics Setup. (a) Illumination and optics diagram. (b) One of three illumination used.

5.2.2 Image Capture: Microscope and CCD Camera

To image the target, a long working-distance microscope (Questar $QM-100$) was used with standoffs between $15-30\ cm$. In the presented experimental setup, the microscope was positioned $\sim 23cm$ from the imaging plane. The microscopes output was a CCD camera (Sony $XCG-5005E$), and the camera was attached to the computer via a gigabit ethernet connection. This allows for large amounts of data to be transferred since the images acquired were high-resolution images. Mounted in front of the CCD camera were two optical filters: a low-pass filter at $945\ nm$ and a band-pass filter at $850\ nm$. Their transmission spectrum are shown in Figure 5.4. The $945\ nm$ filter prevents the high powered Nd:Yag laser beam at $1064\ nm$ from passing into the CCD, thus avoiding laser damage. This is the beam that ablates the metal, causing the compressive shockwave that propagates through all medium. The $850\ nm$ band-pass filter allows only the reflected illumination source from the diode to enter the CCD and prevents ambient light pollution that exist at other wavelengths. The camera was a high resolution black-and-white CCD camera with 2448×2048 pixel resolution and with a peak shutter speed of $10\ ms$. The camera shutter speed, however, is a lot slower than the illumination diodes. This issue can be resolved by manually triggering the camera shutter and trigger the LEDs with a delay generator, thereby allowing an equivalent shutter speed of $\sim 9\ ns$. A $1.41\ mm \times 1.18\ mm$ viewing frame was achieved with the imaging apparatus positioned $23\ cm$ away from the imaging plane. The camera resolution of 2448×2048 pixels and pixel size was $0.58\ \mu m$.

5.2.3 Software

The system was initially designed to implement software consisting of MATLAB which controlled the digital delay generator ($DG-645$ Stanford Research Systems), which in turn controlled the camera shutter, triggering event and LED pulse. Image acquisition was done through the Active Gig-E software supplied by the manufacturer. 8-bit gray Tagged Image File Format (TIFF) picture formatting was selected due to limited computer memory. Through MATLAB, the camera shutter was programmed to open at the 0-second mark at the start of the trigger for a duration of time. At the same trigger time
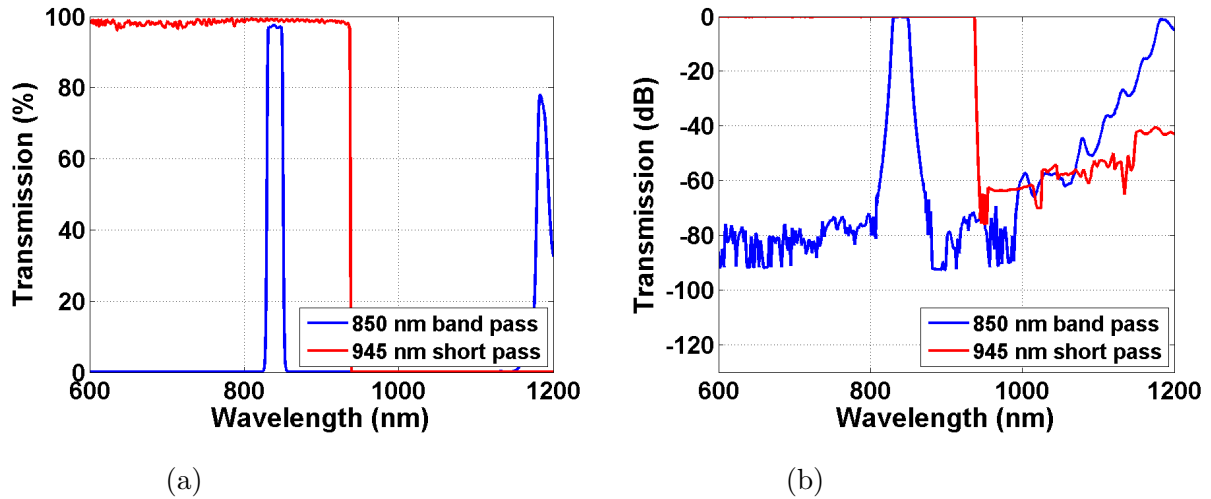
Figure 5.4: Filters. (a) 850 *nm* band-pass and 945 *nm* short pass filter transmission spectrum. (b) Transmission spectrum at 1064 *nm*.

point the delay generator would externally trigger the high-power laser to fire. While the camera shutter was open, the LEDs are pulsed onto the targeting plane and the reflected light would be captured by the microscope and the camera. MATLAB was used to delay the time of LED illumination to capture the event at a different time instance.

For experiments in shockwave imaging, the trigger signal from the delay generator to the laser could not be successfully implemented. Thus, a reconfiguration of the timing mechanisms and trigger processes was done. Since the delay generator could only trigger the laser in the continuous laser output mode whereas the single-shot mode was desired, the laser was instead used to trigger the delay generator using the external sync-out port. The control for the laser, delay generator, and LEDs was thus fixed. Since the time it took to open the camera shutter was slower ($\sim$ microseconds) for the shock wave arrival (a couple of hundred nanoseconds), the shutter cannot be connected to the delay generator package. Therefore opening the shutter was done manually through the Sony XCG camera software. Once the shutter was opened, the laser was signaled to fire and would then activate the LEDs to pulse onto the target. Lastly, the shutter would then close.
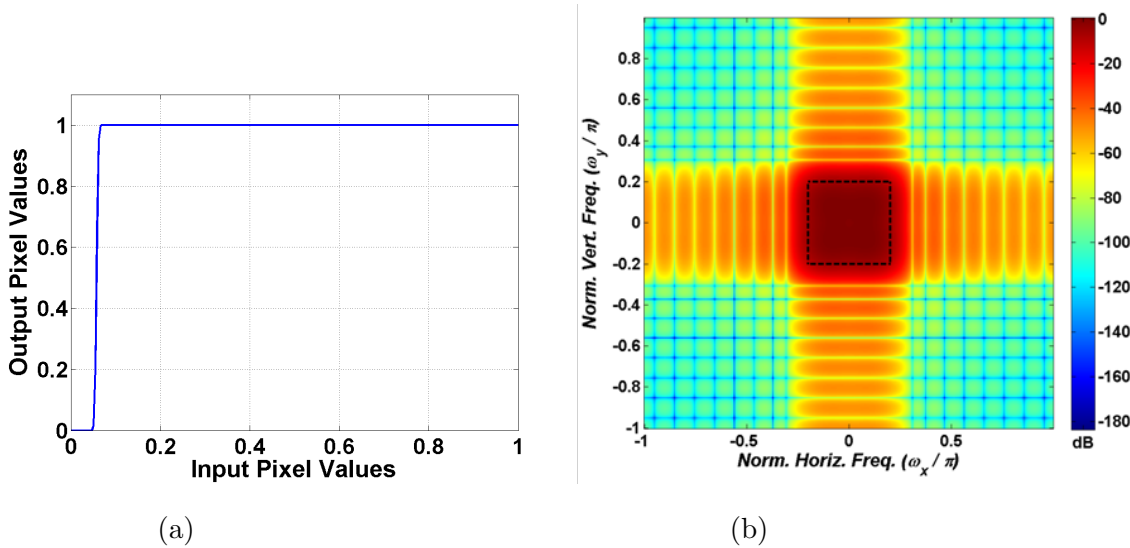
Figure 5.5: Image Processing Steps. (a) Histogram equalization mapping (b) 2-D low-pass filter frequency response after convolving two 1-D FIR low-pass filters.

5.2.4 Image Processing

Image processing was done with MATLAB's histogram equalization and 2-D filtering function. Since the shutter speed was extremely fast and the single pulse energy from the LEDs was low, the raw image was underexposed. The underexposed image had low intensity pixels values. The intensity scale range from 0 to 255 where 255 is the maximum pixel value. Histogram equalization (HE) is implemented and spreads the distribution of the pixel intensities so that values are more evenly distributed. The probability distribution function (PDF) of the input image has most values in a narrow range. The goal for the equalization is to create a transformation for a new image such that its cumulative distribution function (CDF) is linearized across the intensity value range. The transformation is shown in the non-linear mapping of pixel values (Figure5.5a). This increased image contrast, but at the cost of high frequency noise. To decrease image noise, a finite impulse response filter was used. To create a 2-D low pass filter, the filter was convolved with itself producing a blurring kernel that removed high frequency noise in Figure 5.5b, creating a smoother image. The process is explained and demonstrated using one of the high speed images, as shown in Figure 5.6.

The raw image in Figure 5.6a is too dark to discern any identifiable information
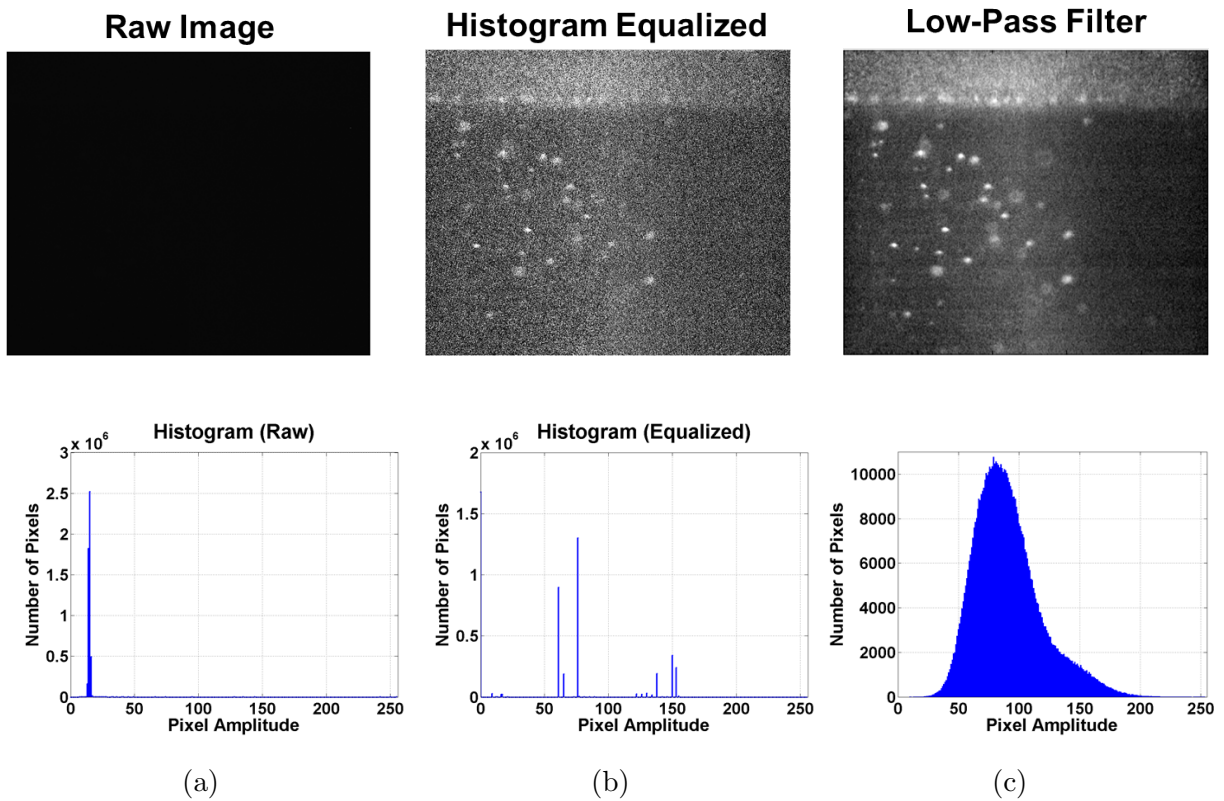
Figure 5.6: Implementation of histogram equalization and low-pass filtering (at 475 ns time point). (a) Raw image and histogram of the image. (b) Histogram equalized image and histogram representation of the image. (c) Low-pass filtered image and histogram representation of the image.

and the histogram shows most pixels lying in a narrow intensity range. With histogram equalization, fine features were enhanced with pixel intensities at all levels (0 to 255) being represented more evenly (Figure 5.6b). Noise was also increased. The low pass filter described earlier was employed to remove high frequency noise. The resulting photo in Figure 5.6c appears to have a smoother surface, whereas in the histogram equalized photo the image is shown to have a mix of very low and very high intensity pixels. Despite the presence of noise, the image becomes more detailed at the cost of spatial resolution. The increase in the number of LED illumination may eliminate the need for this extensive image processing, but this image processing technique in low light levels is valid in this setup.

After image processing and resizing, the pixel size was 2.13 μm per pixel, and this would be used in the analysis of the images.

5.2.5   Performance Test: Optical Power Measurement

The optical power of the three LED light was measured by a power meter (Ophir Orion/TH) set to the YAG setting. The LEDs were aimed in continuous pulsed mode at 3 kHz onto the power meter to ascertain the average power. Average power was converted to peak power by the following equation:

$$P_{peak} = \frac{P_{avg}}{\tau f} \tag{5.1}$$

where τ is the pulse width at 10 ns and f is frequency at 3 kHz. The relationship between power and number of photons is:

$$N_{photon} = \frac{P\lambda}{hc} \tag{5.2}$$

where P is the peak power, λ is the illumination wavelength, h is Planck's constant, and c is speed of light. The average power measured with the three continuously pulsed LEDs shining onto the power meter was calculated to be 2.4 mW. Using equation 5.1, 80 watts of peak power was calculated. To convert this to the amount that actually arrived onto the camera, the ratio of the semi-spherical surface area with radius 23 cm (reflected light from the target) to the area of the microscope aperture was found, and this ratio was

combined with the optical train throughput. The filters have a total attenuation of 2 dB (37% loss). The resulting power arriving at the camera was $\sim 0.0102\ mW$, and using equation 5.2, the amount of photons arriving at the image was $\sim 394,000$ photons per image.

5.3 High Speed Imaging Experiments

Preliminary experiments were performed to verify that image capture of shock wave propagation is feasible, and verify that cavitation effects occur at glass-water interface. In the first set of experiment the laser was applied to the titanium-coated glass slide without any coupling below. In the second set of experiments, the glass slide was coupled to water to image cavitation bubbles at the interface.

5.3.1 Shock Wave Displacement Imaging

5.3.1.1 Sample Preparation

The medium in which the shock wave propagated through was soda-lime glass. Standard 3 inch by 1 inch microscope slides (Corning Inc.), with measured thickness between 0.96 mm to 1.06 mm were used. The top side of the glass slide was coated with a thin 0.5 μm layer of titanium using an RF sputterer. Then, a thin layer or water glass was spin-coated with a thickness of $15 - 20\ \mu m$. The water glass acts as a constraining medium for the shock wave propagation.

5.3.1.2 Imaging Platform

The glass slide was placed on a platform with adjustable x, y, and z-axes. The height of the platform was adjusted such that part of the glass slide is positioned within the view frame of the camera.
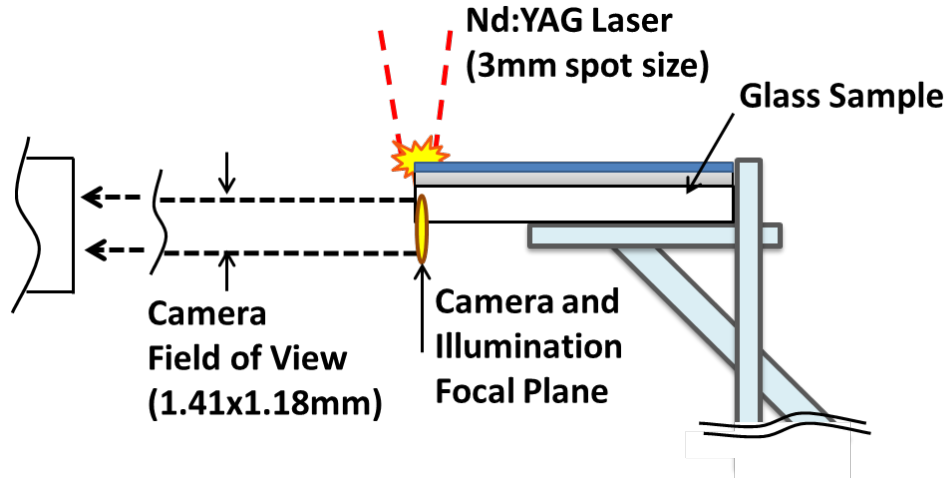
Figure 5.7: Imaging platform and sample setup diagram.

5.3.1.3 Imaging Platform

The laser was set to trigger the delay generator, and the camera shutter is triggered manually instead of connecting to the delay generator. The reason for the manual shutter trigger is that the shutter could not respond fast enough from the delay generator to capture shock wave arrival. From previous tests, the delay between triggering the laser pulse to the mechanical pulse arriving at the titanium layer was measured at $\sim 370\ ns$. The wave traveled through the glass slide in $\sim 169\ ns$. This is calculated from the speed of sound in glass slide ($\sim 5,910\ m/s$) and the thickness of the glass slide ($1\ mm$). Thus to image the shock wave as it exited the glass slide, the delay generator was set to signal the LED at $\sim 460\ ns$ following the laser sync signal. For the camera shutter, the Sony XCG software was used and set for 15 frames per second, with the shutter speed at $66.57\ ms$. The multiple snapshots feature in the software allowed the user to enter the number of frames for capture, and was set to 10. Once the shutter button was pressed, the laser was immediately triggered to fire. Since the LEDs illuminated $\sim 9\ ns$ in duration, only 1 of the 10 captured frames captured the image.

The laser spot size was focused to $3\ mm$ in diameter. The spot was targeted on the edge of the glass slide so that $\sim 3/4$ of the beam would ablate the surface, and $\sim 1/4$ was off the glass slide to create the maximum stress at the edge.
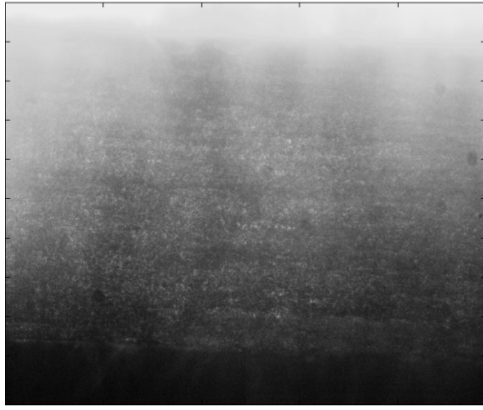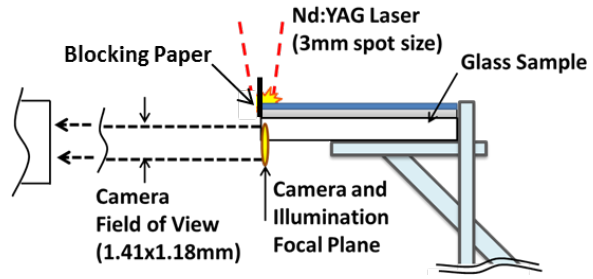
(a)   (b)

Figure 5.8: Shock wave image without blocking paper and the improved setup with blocking paper. (a) Image of shock wave event with 850 nm spark produced by titanium ablation. (b) Imaging platform with blocking paper.

5.3.1.4   Results and Discussion

Figure 5.8a shows the image of the glass slide without a blocking paper to prevent 850 nm light leakage. The ablation spark contains 850 nm light that passes to the CCD sensor. The result is an over saturation of the image. Because of this, a blocking paper was placed vertically next to the glass slide to prevent the plasma-spark from reflecting into the camera, as in Figure 5.8b. The images were successfully acquired using the high speed imaging system. In Figure 5.9b and 5.9e, there are bright regions near the top of the images. This is likely 850 nm emission from the plasma. From the displacement interferometer results, the maximum displacement this type of shockwave can induce in the glass slide is $\sim 4\mu m$ at 93 mJ/mm^2 (660 mJ/pulse), as shown in Figure 19. Since the system resolution is ~ 2.13 μm per pixel, this displacement of 4 μm would result in a maximum displacement of ~ 1.9 pixels in the image; a value that is difficult to discern between vibrational displacement and actual shockwave displacement. However, in Figure 5.9b, the shock wave does generate localized displacement that is observable when compared to Figure 5.9a. Although compressive waves propagating through the medium are not being captured at this moment, transient events of the glass material fracturing can be seen in Figure 5.9e. This occurs due to the absence of coupling medium
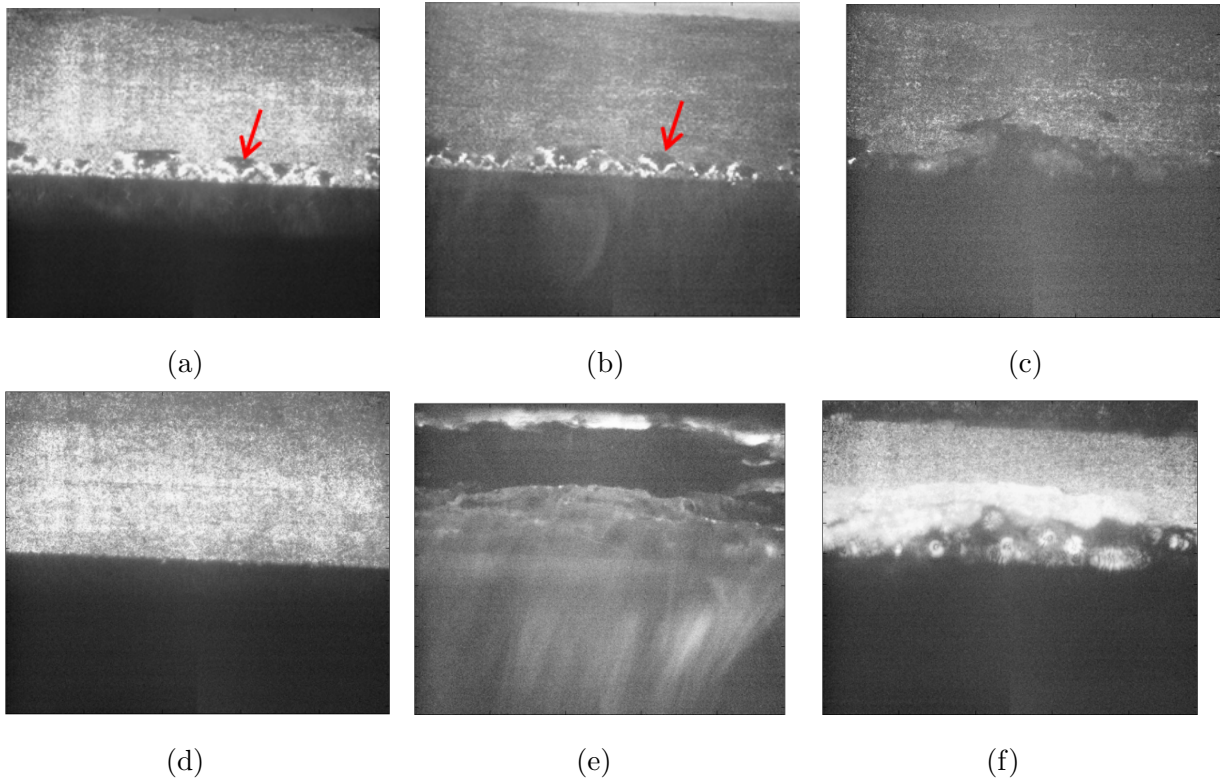
Figure 5.9: Series of images before, during, and after the shock wave event for two spots. (a) Before laser firing. (b) During shock wave at 460 ns. (c) After effect. (d) Before laser firing. (e) During shockwave at 530 ns. (c) After effect. Images a, b, and c are of spot 1. Images d, e, and f are of spot 2. Red arrows indicate area with glass displacement due to the shockwave.
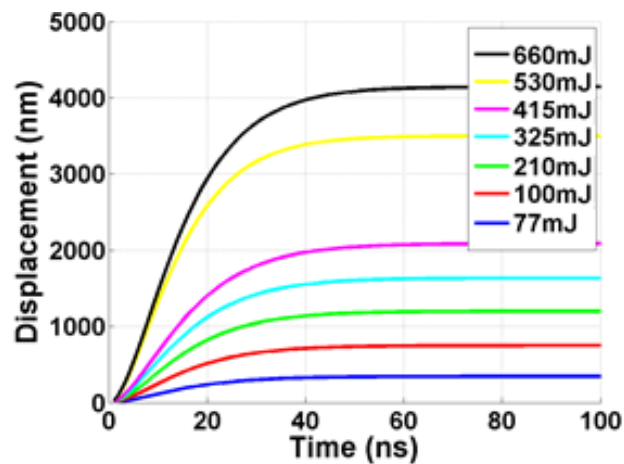
Figure 5.10: Displacement profile for glass interferometry. Energy values correspond to the total amount of laser energy per pulse that is focused over a 3 mm spot size.

at the second surface of the glass slide. Once the shock-wave travels to the glass-air interface, it reflects back as a tensile wave due to a large impedance mismatch with air. This process exceeds failure level of the glass at the bottom surface. Adding a coupling medium such as water allows the wave to propagate from the glass slide to the water medium without significant reflection.

5.4 Shock Wave Cavitation Bubble Imaging

5.4.1 Sample Preparation

From previous experiments, there exists emission of light during ablation of the titanium in the 850 nm range. This causes light pollution in the acquired images. To prevent this, the bottom of the glass slide was coated with a layer of black ink to prevent light from shining through the glass slide once the titanium was ablated. Additionally, a thin blocking paper was placed vertically on top of the edge of the glass slide to prevent excess light from entering the camera. The laser energy was fixed at 530 mJ/pulse.

The process of coating the titanium on the glass slide is the same as the process described in the previous experiments. 0.5 μm of titanium was sputtered onto the glass slide, and $15 - 20$ μm of water glass was spin-coated onto the titanium.

5.4.2 Imaging Platform

A glass slide holder was specifically designed for this experiment, and is shown in Figure 5.11. It contains a well for water and a side window with a thin microscope coverslip covering it. The glass slide was placed horizontally next to the microscope coverslip, and water was added until there was no air below the glass slide. The blocking paper described earlier was placed on top of the edge (that is facing the coverslip) of the glass slide, with the blocking papers surface parallel and adhered to the coverslip. The field of view of the camera was set below the glass side (Figure 5.11b), with the edge of the glass slide protruding down $\sim$ 0.2 mm from the top of the viewing frame. The vertical focusing plane was $\sim$ 1 mm into the glass slide, so the edge of the glass slide was out of

(a)   (b)
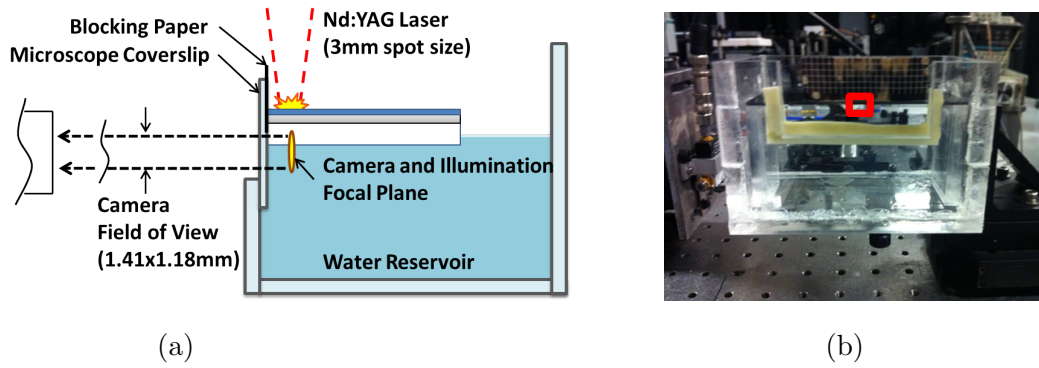
Figure 5.11: Imaging Platform. (a) Diagram of side view cut-through of platform. (b) Actual setup of the platform in the POV of the camera. Red box shows the approximate field of view
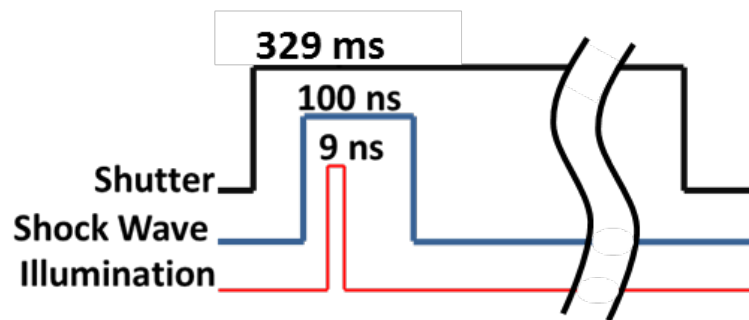
Figure 5.12: Timing mechanism for illumination and capture.

focus.

5.4.3 Timing Mechanism

The software utilized to capture images was the Sony XCG manufacture software. The timings are shown in Figure 5.12. The software trigger for capturing images was triggered manually. With each trigger the camera took three frames, with each frame lasting 329.42 ms. The laser sync-out controlled the delay generator, and controlled the timing of the LED pulse. This ensured that the event was captured within the three frames.

(a)	(b)	(c)
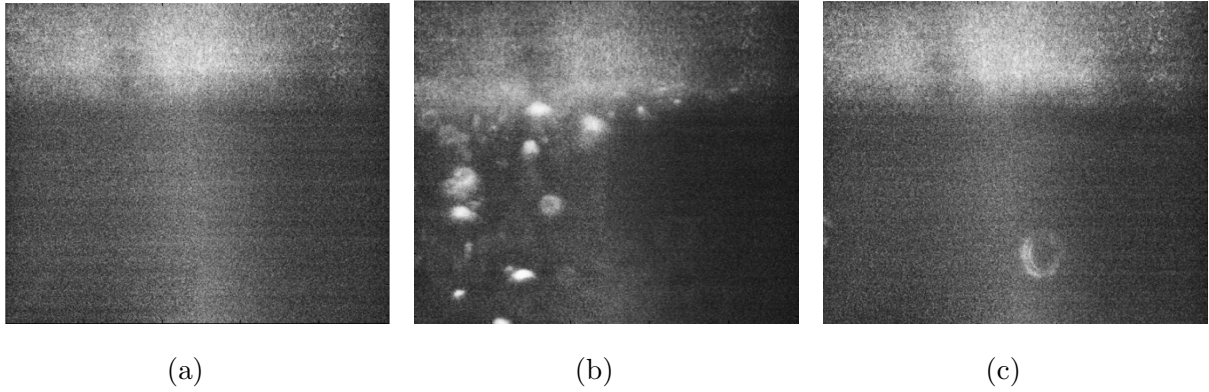
Figure 5.13: Images of the same spot before, during, and after the shock wave event. (a) Before firing the laser. (b) During the laser shock wave taken at 475 ns after the laser firing. (c) After the shock wave event. Two bubbles adhered to the microscope coverslip are visible.

5.4.4 Results and Discussion

Figure 5.13 shows the series of images taken before, during, and after the shock wave. The image during the shockwave event, Figure 5.13b, was taken at the 475 ns time point. The bright horizontal slab at the top of the images is the bottom portion of the glass slide in which shock wave is generated. The glass slide is out of focus since the focusing plane is $\sim 1\ mm$ into the glass slide instead of on the edge. There is no cavitation before the shock wave arrives as expected, and after the shock wave event there are two bubbles evident. The bubbles are adhered to the microscope coverslip that is located in front of the horizontal glass slide. Results show that the cavitation bubbles are due to the propagated shockwave at the glass/water interface. Images shown are generated by processed data. There exists a camera CCD defect when operating with long shutter times. With a shutter length of 60 ms and longer, there exists a vertical edge that separates the image into two panels. This is observed with both single shot images and after image processing. The left panel has one corner with darker pixels than the rest of the pixel intensity, as shown in Figure 5.14a. This phenomenon may be the result of several factors. One, the dark noise level may be different at different regions of the CCD. Thus, the sensitivity of each well of the CCD varies. During long shutter exposures, certain regions acquire
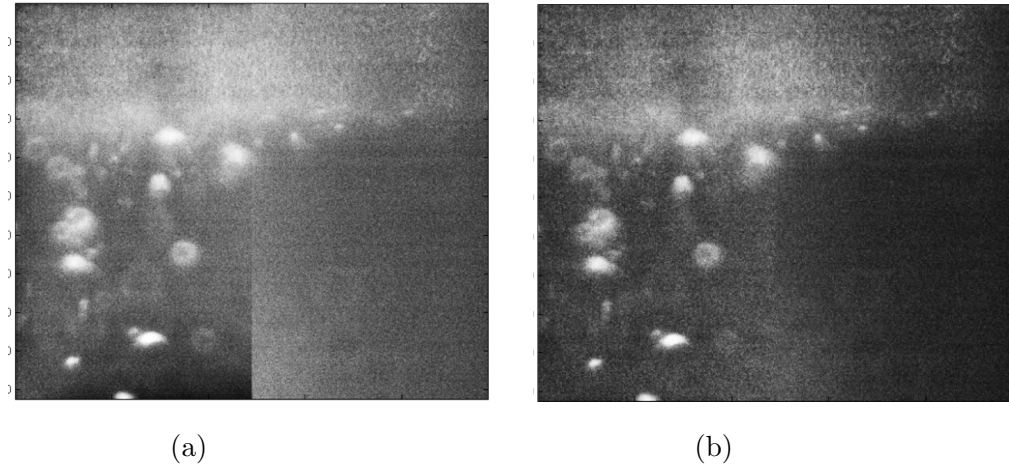
Figure 5.14: Camera CCD defect correction. (a) Image with defect in CCD array. (b) Corrected image using image processing.

more photons than others resulting in pixel intensity differences. These factors could not be adjusted using the Sony software. Thus, MATLAB image processing was used to improve the quality of the images without sacrificing image content. Since the defect is observable in all the images, a blank reference image with just the defect was made by covering the microscope. The blank image was split into two halves. The matrix of the right half was flipped horizontally and is subtracted by the left half. This left half of the blank reference image was the image added to the left half of the actual cavitation image to eliminate the center defect. Figure 5.14b shows noticeable improvement over the original processed image.

Cavitation in tissues induced by shockwaves causes tissue damage [140]. But propagating bubbles created by cavitations may also have an effect on bacteria biofilm delamination and potential death. The images have shown that microbubbles exist in the coupling medium that exist at the glass-slide water interface.. The bubbles travel down at least 1 mm, which is enough to reach and interact with the biofilm. Xu et al. found that individual bubbles merge to form clusters of bubbles [141], and used lithotripters to produce shockwaves in kidney stones. Qualitative results show that the shockwave produces a collection of microbubbles traveling at least 1 mm. The distance that the bubbles travel may be more than 1 mm since the bubbles may extend out of the viewing window. Nevertheless, the existence of bubbles shows that cavitation occurs near the

interface.

Cavitation effects at different time instances are shown in Figure 5.15. The shock-wave reaches the glass-water interface at $\sim 460\ ns$. At $465\ ns$, clusters of bubble formation are seen (Figure 5.15a). From $495 - 535\ ns$ the shapes and sizes of the bubbles remain relatively constant. And from $1000 - 2000\ ns$, there are significantly less bubbles. Because the cavitations were in a 3-dimensional space, out-of-focus bubbles were also observed. The time frame for bubble formation and collapse is several microseconds [142]. From our images, the time frame is $2\ \mu s$. After $2\ \mu s$ there are fewer bubbles since they may have collapsed or migrated to other regions out of view.

The sizes and number of bubbles in the images change with different time points. ImageJ software was used to investigate cavitation bubble sizes with respect to time by outlining the clearest bubbles for each image using the blind automated cell counting feature. Four of the outlined images are shown in Figure 5.16). The shockwave leaves the glass slide at $\sim 460\ ns$. Figure 5.17 shows the bar graph for the amount of bubbles counted for each image. Figure 5.18 shows the average diameters of the bubbles found for each image. Because the camera field of view is 1.41 x 1.18 mm, there is high probability that bubbles migrate outside the field of view. Thus the amount of bubbles is inconsistent according to Figure 5.17. The average diameter for the first 60 ns of the images is 39 μm. The average diameter for later time points (from 600 ns to 2000 ns) increases up to 71 μm. In the time interval of 2000 ns, the overall cavitation sizes increase. Taking the number of cavitation into consideration, the images from 515 ns to 535 ns have the highest number of bubbles. In addition, their diameters are the smallest. In the biofilm disruption experiment described in Chapter 3, the medium between the shock wave generation plate and the biofilm sample was 1 mm. Thus there is enough distance for the microbubbles to interact with the biofilm. In addition, from experiments in biofilm delamination using glass modified shockwaves, small localized areas of delamination are evident and shown in Figure 5.19. The small pores of empty biofilm surround the central delamination spot, due to the purely tensile effect of the shockwave.
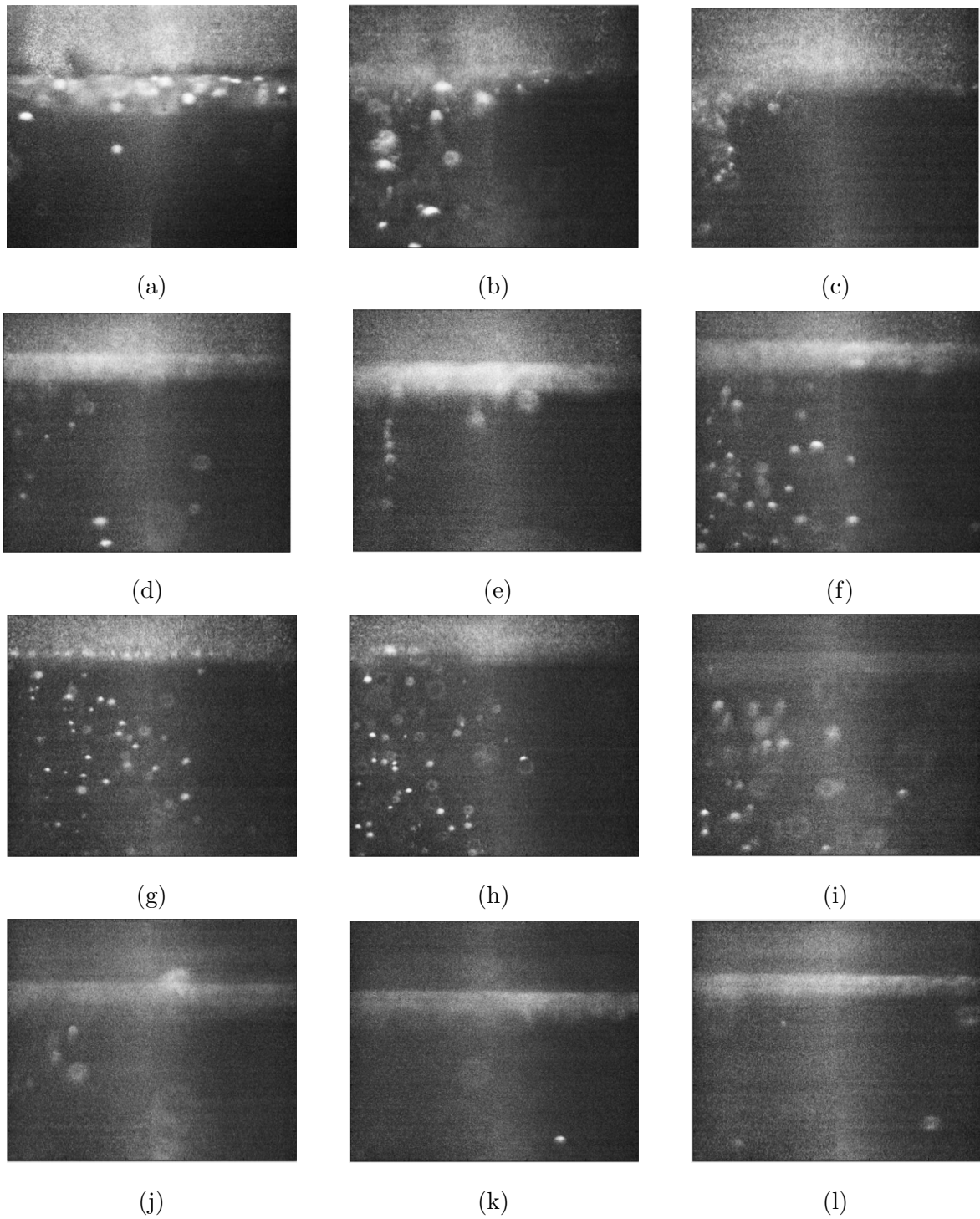
Figure 5.15: Cavitation images from 475 ns to 2000 ns. (a) 465 ns, (b) 475 ns, (c) 485 ns, (d) 495 ns, (e) 505 ns, (f) 515 ns, (g) 525 ns, (h) 535 ns, (i) 800 ns, (j) 1000 ns, (k) 1500 ns, (l) 2000 ns.
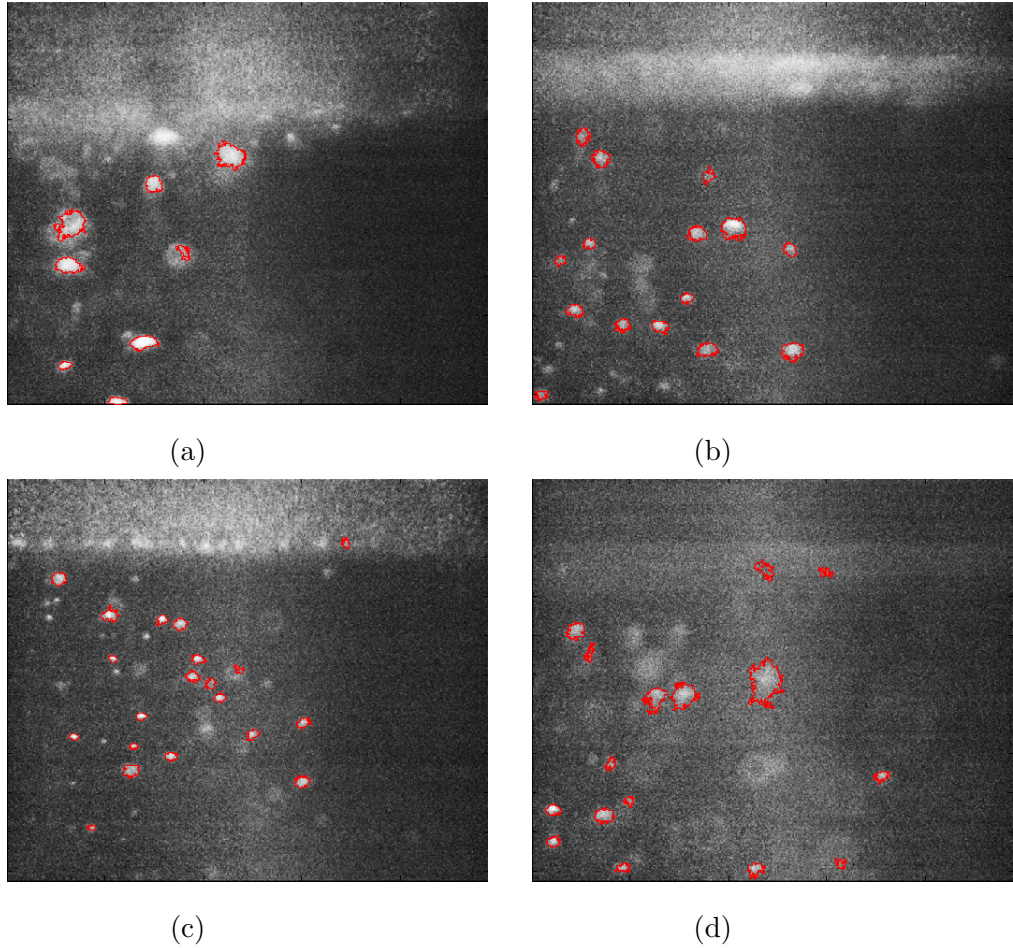
Figure 5.16: Outlined cavitation images at different time points. (a) 475 ns. (b) 515 ns. (c) 525 ns. (d) 800 ns. The red outlines show most of the clearest bubbles. They are incorporated in bubble diameter calculations.

(a)　　　　　　　　　　　(b)
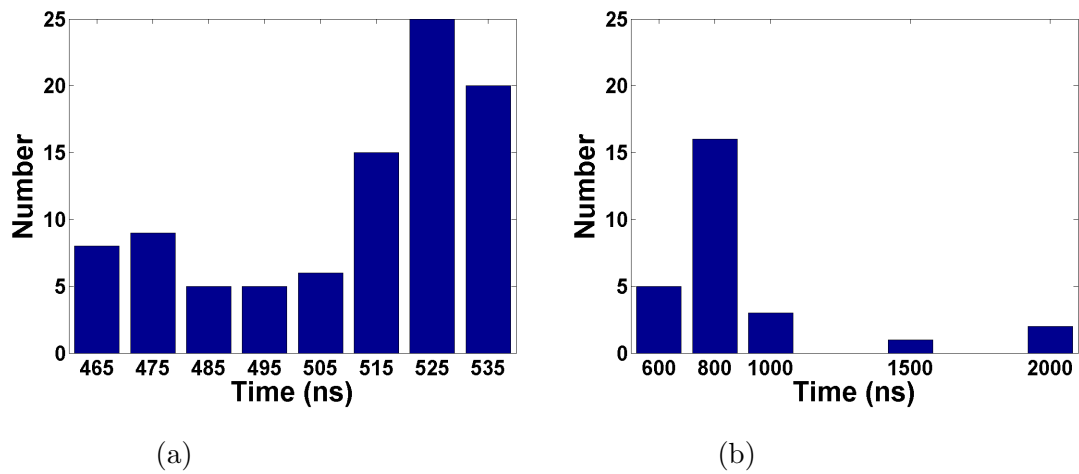
Figure 5.17: Amount of bubbles counted for each time point. (a) Time points from 465 ns to 535 ns. (b) Time points from 600 ns to 2000 ns.

(a)　　　　　　　　　　　(b)
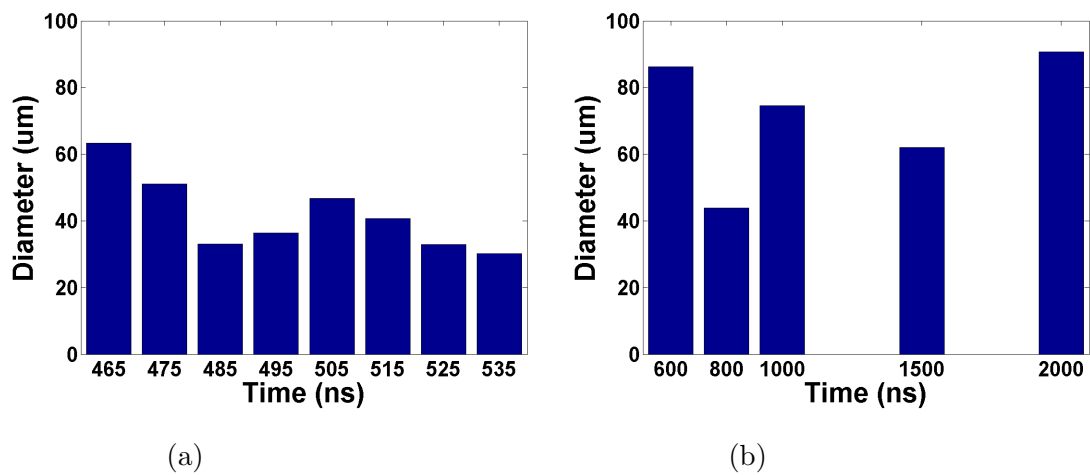
Figure 5.18: Diameter of bubbles for each time point. (a) Time points from 465 ns to 535 ns. (b) Time points from 600 ns to 2000 ns.
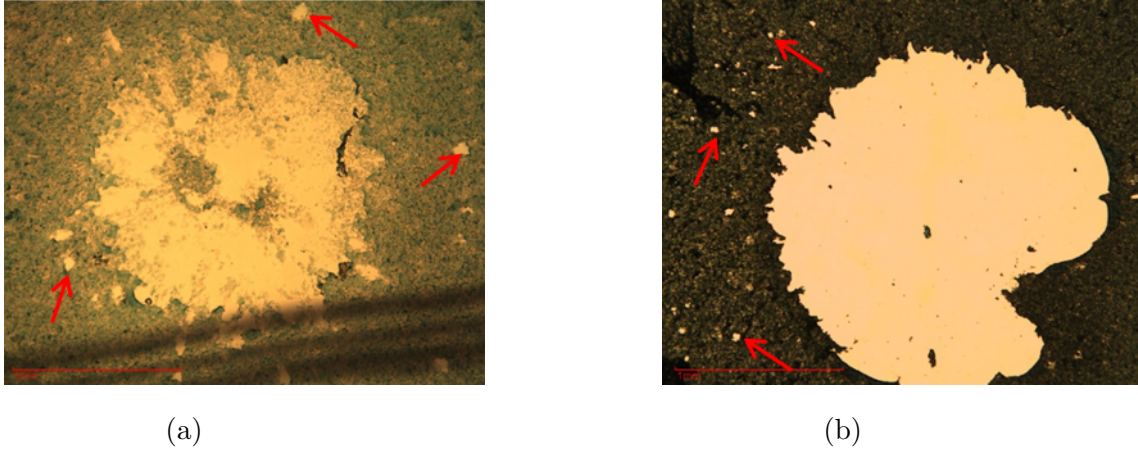
Figure 5.19: Biofilm delamination at 75 mJ/mm^2 for (a) Two-day growth and (b) three-day growth. Red arrows show localized areas of delamination due to bubble cavitation.

5.5 Conclusions

A system to capture fast events, such as shock waves, without image blur requires fast shutter speed. Using a camera, long-distance microscope, and pulsed LED, nanosecond illumination was produced to capture shockwave-induced phenomenon. Images of clear bubbles without blur were captured, showing the existence of cavitation microbubbles. The cavitations propagated at least 1 mm, enough to reach the biofilm layer. During this process, the microbubbles may collapse and produce secondary or further waves to facilitate biofilm delamination. However, in this study, the main contributor to biofilm delamination is due to the purely tensile component of the shockwave. In addition to being an inexpensive system, the high speed imaging system gives several advantages. One, the long-distance microscope provides a larger aperture, allowing some apparatus to be closer to the field of view of the lens without blocking light from entering the camera. Second, the microscope allows the target to be at a distance preventing potential lens damage caused by during the ablation of the titanium metal. Third, 850 nm illumination and band-pass filtering prevents light pollution from other wavelengths, and allow the system to be placed in normal lighting condition instead of dark room. With further improvements in size packaging, the system may become more portable and convenient to image high speed events of various kinds in multiple applications.

CHAPTER 6

Conclusion and Future Work

6.1 Conclusions

A modified version of the Laser Spallation Technique (LST) was built and successfully used to quantify the adhesion strength of *S. epidermidis* biofilms ($RP62A$) on polystyrene under static conditions. According to a $1 - D$ analytical wave propagation model, the adhesion strength of the biofilm is calculated to be 22.75 $MPa \pm 0.16\%$. This is comparable to studies that also used LST to quantify the adhesion strength of mammalian cells. Higher energy fluences lead to higher peak stresses and rarefaction shocks. This lead to more of the shocked area to have the critical tensile stress to cause more delaminations. High strain rates of 1.544×10^5 s^{-1} and 1.41×10^6 s^{-1} in glass and in biofilm, respectively, were calculated and total strains of 0.3 % in glass and 3 % in the *S. epidermidis* biofilm are measured, thereby safely loading the material in the linear elastic region. The high strain rate loading suppresses any plastic deformation and since there is pure tensile loading, the decohesive failure is a purely intrinsic measurement and independent of the geometry of the biofilm being tested.

Glass-modified laser-generated shockwaves were explored to study the affect on porcine skin. Shockwaves with sharp rise times $\sim 2 - 6$ ns and peak stresses ranging from $21 - 266.5$ MPa were coupled toward pigskin and yielded no structure damage after staining and observation by a trained pathologist in a blind study. A large impedance match existing between glass and water lead to a train of compressive stresses that are 18% in peak stress. This is a quite powerful effect as one pulse from the laser source could effectively generated multiple mechanical pulses that could prove to be beneficial in drug delivery to biofilm structures residing on biotic or abiotic surfaces. Also, in a

wound model, these shockwaves could potentially target the biofilm without causing any damage to underlying tissue.

A low cost, highspeed imaging system was built and optimized to capture shockwave-induced phenonmen, i.e. cavitation. Results show cavitation bubbles were generated between glass and water due to the a transition into tensile stress. The cavitation bubbles traveled toward the biofilm and caused localized areas of delamination as these bubbles imploded.

6.2 Recommendations

This study only explored the use of a specific species of bacteria, *S. epidermidis* grown on polystyrene under static conditions. The Laser Spallation Technique proved to be an effective tool in measuring the adhesion strengths of these biofilms and the adhesion strength of other mammalian cells. Future studies should include studying how the adhesion strengths of biofilms differ while undergoing dynamic growth conditions. Also, the substrates in which biofilms grow must also be studied to understand the difference in adhesion strength.

Studies on the effect of the glass-modified stress waves on porcine samples, ex vivo, should extend to delivery of molecules, whether dyes or drugs, to the skin and study the extent of propagation through the skin. Glass-modified stress waves should be explored due to its ability to not only generate rarefaction shock fronts under high stresses but when coupled to water, these mechanical pulses can generate a train of compressive forces that can prove beneficial in drug delivery. One draw back to glass is its rigidity. Thus it is not ideal to use glass slides as a treatment modality on wound surfaces due to the non uniformity of the wounds. Other materials should be explored and the resulting stress waves should characterized. On a cellular level, viability studies should be done on both bacteria and mammalian cells in order to study the direct effect of the shockwaves on cell structures.

Finally, the high-speed imaging should be improved by adding more illumination diodes to enhance to trigger the already photon-starved CCD. More illumination will

lead to less filtering, an effect that causes blurring of pixels and thus loss of spatial resolution. The high speed imaging system should be extended to capture shockwave induced phenomenon at different layers in the experimental model and also try to capture the biofilm as it is being delaminated.

APPENDIX A

Analytical 1-D Wave Propagation Model: Matrix Method

Mal et al. [143] developed a 1-D, multi-layered wave propagation that finds the interfacial stress between layers and the model has been applied to the understanding adhesion strengths of mammalian cells on different materials [85, 121]. Once the input stress is determined by the Laser Spallation Technique, this stress will be an applied stress boundary condition to the analytical model. The model will then be implemented to calculate the interfacial stresses history in order to determine the peak tensile stress that causes spallation or interface failure between interfaces.

A.0.1 Problem Statement

A one dimensional plane wave propagation problem in a multilayered plate is considered (Figure A.1) and consists of N layers of homogeneous isotropic and elastic material. The plate is defined from region $x_0 < x < x_N$, where the thickness of the nth layer defined between $x_{n-1} < x < x_n$ is h_n. The input stressed is applied at the top surface where $x = x_0 = 0$, while it is traction free at the bottom surface, $x = x_N$. The longitudinal wave travels along the x-axis while particle motion is in the x-direction. It is assumed that the layers in the plate are perfectly bonded such that the displacement and stresses between the layers are shared and equal to each other and thus maintaning continuity.

The material for the nth layer can me characterized by its its physical density ρ_n, and by its longitudinal speed of sound, α_n. The longitudinal speed of sound can be solved for
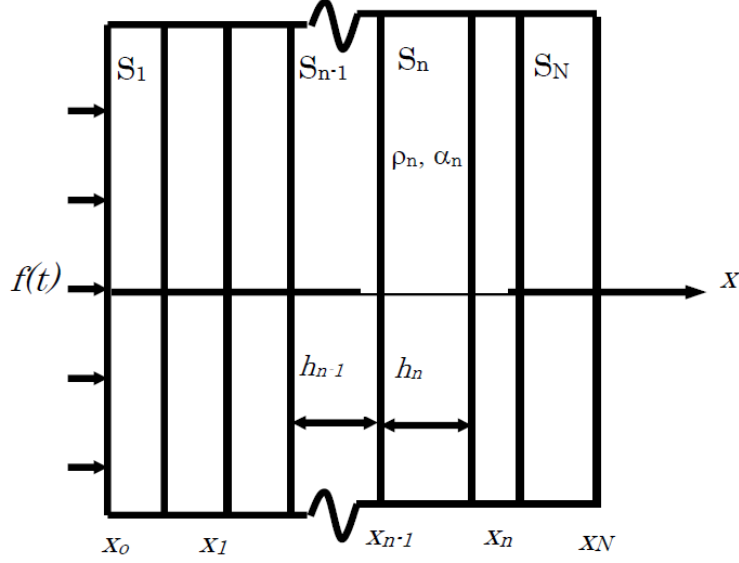
Figure A.1: Idealized wave propagation model.

by knowing the elastic constants E, or Young's Modulus, and ν or Poisson's ratio by

$$\alpha_n = \sqrt{\frac{E_n(1-\nu)}{\rho_n(1+\nu_n)(1-2\nu_n)}} \tag{A.1}$$

or they can be related to the Lamé constants λ_n and μ_n by 3.4

A.0.2 Governing Equations

Since it can be assumed that the wave propagates in one dimensional multilayered medium, the displacement field and stress fields can be expressed as $u_n(x,t)$ and $\sigma_n(x,t)$ for each sublayer and must satisfy Navier's Equations:

$$\frac{\partial^2 u_n(x,t)}{\partial x^2} = \frac{1}{\alpha^2}\frac{\partial^2 u_n(x,t)}{\partial t^2}, \qquad x_{n-1} \leq x \leq x_n \tag{A.2}$$

and

$$\sigma_n(x,t) = \frac{1}{\alpha_n^2}\frac{\partial^2 u_n(x,t)}{\partial t^2} \tag{A.3}$$

The next step is to convert the governing equations into the frequency domain by

93

finding the Fourier transform. Equations A.2 can be transformed to

$$\frac{\partial^2 u_n(x,\omega)}{\partial x^2} + k_n^2 u_n(x,\omega) = 0 \tag{A.4}$$

where

$$k_n^2 = \frac{\omega}{\alpha_n} \tag{A.5}$$

such that k is known as the wave number and ω is the circular frequency. The solution to A.4 can be shown to be

$$u_n(x,\omega) = A_n e^{ik_n(x-x_{n-1})} + B_n e^{-ik_n(x-x_{n-1})} \tag{A.6}$$

where A_n and B_n are constants that need to be determined by interface continue conditions and boundary conditions in order to have a unique solution.

The stress field can be obtained by pluggin in equation A.6 into equation A.3 and obtaining

$$\sigma_n(x,\omega) = i\omega z_n [A_n e^{ik_n(x-x_{n-1})} - B_n e^{-ik_n(x-x_{n-1})}] \tag{A.7}$$

where

$$z_n = \rho_n \alpha_n \tag{A.8}$$

is known as the impedance for the $n-th$ layer. Note that the first component in u_n and σ_n are the waves propagating along the positive x-direction while the second term accounts for the waves traveling in the negative x-direction.

All ω arguments are omitted for further discussion. A two-dimensional "stress-displacement vector" $\{\hat{S}_n\}$, in the frequency domain is defined as

$$\{\hat{\mathbf{S}}_n\} = \begin{Bmatrix} u_n(x) \\ \sigma_n(x) \end{Bmatrix} = \tag{A.9}$$

$$= \begin{bmatrix} 1 & 1 \\ i\omega z_n & -i\omega z_n \end{bmatrix} \begin{bmatrix} e^{ik_n(x-x_{n-1})} & 0 \\ 0 & e^{-ik_n(x-x_{n-1})} \end{bmatrix} \begin{Bmatrix} A_n \\ B_n \end{Bmatrix} \tag{A.10}$$

$$= \mathbf{Q}_n^{-1}\mathbf{E}_n(x-x_{n-1})\mathbf{C}_n \tag{A.11}$$

where

$$\mathbf{Q}_n = \begin{bmatrix} 1 & 1 \\ i\omega z_n & -i\omega z_n \end{bmatrix} \implies \mathbf{Q}_n = \frac{1}{2i\omega z_n} \begin{bmatrix} i\omega z_n & 1 \\ i\omega z_n & -1 \end{bmatrix} \tag{A.12}$$

$$\mathbf{E}_n = \begin{bmatrix} e^{ik_n(x)} & 0 \\ 0 & e^{-ik_n(x)} \end{bmatrix} \implies \mathbf{E}_n(0) = \mathbf{I} \tag{A.13}$$

$$\mathbf{C}_n = \begin{Bmatrix} A_n \\ B_n \end{Bmatrix} \tag{A.14}$$

A.0.3 Continuity Conditions

When applying the interface continuity at $x = x_{n-1}$, between the nth and $n^{th} - 1$ layers, and knowing that at the stress state for the nth layer is

$$\{\hat{\mathbf{S}}_n(x_{n-1})\} = [\mathbf{Q}_n][\mathbf{E}_n(0)]\{\mathbf{C}_n\} = [\mathbf{Q}_n]\{\mathbf{C}_n\} \tag{A.15}$$

then interface continuity conditions are expressed by

$$\{\hat{\mathbf{S}}_{n-1}(x_{n-1})\} = \{\hat{\mathbf{S}}_n(x_{n-1})\} = [\mathbf{Q}_n]\{\mathbf{C}_n\} \tag{A.16}$$

From (A.11) and (A.13)

$$\{\hat{\mathbf{S}}_n(x_n)\} = [\mathbf{Q}_n][\mathbf{E}_n(h_n)]\{\mathbf{C}_n\} \tag{A.17}$$

Thus

$$\{\mathbf{C}_n(x_{n-1})\} = [\mathbf{E}_n(h_n)]^{-1}[\mathbf{Q}_n]^{-1}\{\hat{\mathbf{S}}_n(x_n)\} \tag{A.18}$$

and from (A.11)

$$\{\hat{\mathbf{S}}_{n-1}(x_{n-1})\} = [\mathbf{P}_n]\{\hat{\mathbf{S}}_n(x_n)\} \tag{A.19}$$

where

$$[\mathbf{P}_n] = [\mathbf{Q}_n][\mathbf{E}_n(h_n)]^{-1}[\mathbf{Q}_n]^{-1} = \begin{bmatrix} cosh(ik_n h_n) & -sinh(ik_n h_n/ik_n h_n) \\ -i\omega z_n sinh(ik_n h_n) & cosh(ik_n h_n) \end{bmatrix} \tag{A.20}$$

is the "propagator matrix" of the n-th layer that relates the displacements and stresses between the nth and $n^{th} - 1$ layer.

A.0.4 Boundary Conditions

By utilizing the recursive relationship in Eq. A.19 we can find the stresses and displacements at the boundary conditions by:

$$\{\hat{\mathbf{S}}_1(x_0)\} = [\mathbf{P}_1]\{\hat{\mathbf{S}}_1(x_1)\} = [\mathbf{P}_1][\mathbf{P}_2]\{\hat{\mathbf{S}}_1(x_1)\} = [\mathbf{P}_1][\mathbf{P}_2]\cdots[\mathbf{P}_N]\{\hat{\mathbf{S}}_N(x_N)\} \qquad \text{(A.21)}$$

Appplying the traction boundary conditions at the front $(x = x_0)$ and back surface $(x = x_N)$ of the plate gives

$$\{\hat{\mathbf{S}}_1(x_0)\} = \left\{ \begin{array}{c} u_1(x_0, \omega) \\ -F(\omega) \end{array} \right\} \qquad \text{(A.22)}$$

and

$$\{\hat{\mathbf{S}}_N(x_N)\} = \left\{ \begin{array}{c} u_N(x_N, \omega) \\ 0 \end{array} \right\} \qquad \text{(A.23)}$$

where $F(\omega)$ is the Fourier transform of the applied load $f(t)$. Thus we obtain

$$\left\{ \begin{array}{c} u_N(x_N, \omega) \\ 0 \end{array} \right\} = \begin{bmatrix} P_{11} & P_{12} \\ P_{21} & P_{22} \end{bmatrix} \left\{ \begin{array}{c} u_N(x_N, \omega) \\ -F(\omega) \end{array} \right\} \qquad \text{(A.24)}$$

where

$$[\mathbf{P}] = [\mathbf{P}_1][\mathbf{P}_2]\cdots[\mathbf{P}_N] \equiv= \begin{bmatrix} P_{11} & P_{12} \\ P_{21} & P_{22} \end{bmatrix} \qquad \text{(A.25)}$$

The surface displacements can now be obtained by solving Eq. (A.24) by

$$u_N(x_N, \omega) = \frac{F(\omega)}{P_{21}} \qquad \text{(A.26)}$$

$$u_1(x_0, \omega) = -\frac{P_{11}}{P_{21}} F(\omega) \qquad \text{(A.27)}$$

To obtain the time domain response of the material under an applied load, the inverse Fourier transform can be performed. The velocity of at $x = x_N$ can be expressed as:

$$v_N(x_N, \omega) = -i\omega u_N(x_N, \omega) = \frac{i\omega F(\omega)}{P_{21}} \qquad \text{(A.28)}$$

Since no closed form solution for a plate with more than 2 layers can be obtained, a Matlab script is used to solve for the stresses at the interfaces. Details of the script are found in Appendix A.

APPENDIX B

Matrix Method Matlab Script

```matlab
%%%%%%%%%%%%%%%%%%%%%%%%%%%%%%%%%%%%%%%%%%%%%
%%%% Matrix Method Script
clc; close all; clear all;
tic;
N=5; % Number of layers
c1=5909.947;c2=1481;c3=1540;c4=2530.47;c5=1481; %P-Wave Speeds from
rho1=2530; rho2=1000; rho3=1140; rho4=1004;rho5=1000;   %rho= Densities
h1=1e-3; h2=1e-3; h3=0.02849e-3; h4=0.830e-3; h5=100e-3;  % Layer ...
    Thickness
% h4=1e-3;
Q=1000; % for damping, 100-1000, to remove singularity
for m=1:N
    if(mod(m,5)==0)
        rho(m)=rho5;
        h(m)=h5;
        c(m)=c5;
    elseif(mod(m,5)==4)
        rho(m)=rho4;
        h(m)=h4;
        c(m)=c4;
    elseif(mod(m,5)==3)
        rho(m)=rho3;
        h(m)=h3;
        c(m)=c3;
    elseif(mod(m,5)==2)
        rho(m)=rho2;
```

```matlab
26          h(m)=h2;
27          c(m)=c2;
28      elseif(mod(m,5)==1)
29          rho(m)=rho1;
30          h(m)=h1;
31          c(m)=c1;
32      end
33      z(m)=rho(m)*c(m);
34  end
35  T=5e-6; % TOTAL RUN TIME
36  NP=2^14; % Number of data points
37  dt=T/NP; % Time Step
38  t=0:dt:T; % Time vector
39  p0=3995;   %for 11 mj/mm^2. Gamma constant
40  b0=8.6;    % alpha constant
41  c0=8.3;   % beta constant
42  p=0.5*rho1*c1*p0*(exp(-t*10^9/b0)-exp(-t*10^9/c0)); %Input Stress
43
44  W=2*pi/(T)*(0:NP/2);   %Frequencies
45  FP=fft(p,NP);    %Fourier transform of source
46
47  Pn=inline('[cosh(i*kn*hn) ...
        -sinh(i*kn*hn)/(i*w*zn);-i*w*zn*sinh(i*kn*hn) cosh(i*kn*hn)]');
48  for m=1:NP/2+1
49  P=eye(2);
50  w=W(m);
51  if(w~=0)
52      for n=1:N
53          kn=w/c(n)*(1+0.5*i/Q);
54          hn=h(n);
55          zn=z(n);
56          P=P*Pn(kn,hn,w,zn); %P=P(1)P(2)...P(N)
57
58      end
59  end
60  if(w==0)
```

```
61        u(1,m)=0;
62        u(N+1,m)=0;
63  else
64        u(1,m)=-P(1,1)/P(2,1);
65        u(N+1,m)=-1/P(2,1);
66  end
67  v(1,m)=-i*w*u(1,m);
68  s(1,m)=-1.0;
69  v(N+1,m)=-i*w*u(N+1,m);
70  s(N+1,m)=0.0;
71  if(w≠0)
72        for n=2:N
73            D=eye(2);
74            for k=n:N
75                kn=w/c(k)*(1+0.5*i/Q);
76                hn=h(k);
77                zn=z(k);
78                D=D*Pn(kn,hn,w,zn);  %D=P(n+1)P(n+2)...P(N)
79            end
80            u(n,m)=-D(1,1)/P(2,1);
81            v(n,m)=-i*w*u(n,m);
82            s(n,m)=-D(2,1)/P(2,1);
83        end
84  else
85        for n=2:N
86            u(n,m)=0.0;
87            v(n,m)=0.0;
88            s(n,m)=0.0;
89        end
90  end
91  end
92  for k=1:N+1
93        for m=NP:-1:NP/2+2
94            u(k,m)=conj(u(k,NP-m+2));
95            v(k,m)=conj(v(k,NP-m+2));
96            s(k,m)=conj(s(k,NP-m+2));
```

```matlab
 97        end
 98   end
 99   u=conj(u);
100   v=conj(v);
101   s=conj(s);
102   for k=1:N+1
103       for m=1:NP
104           uu(k,m)=u(k,m)*FP(m);
105           vv(k,m)=v(k,m)*FP(m);
106           ss(k,m)=s(k,m)*FP(m);
107       end
108   end
109   tt=dt*(0:NP/2);
110   for k=1:N+1
111       ut(k,:)=ifft(uu(k,:),NP);
112       vt(k,:)=ifft(vv(k,:),NP);
113       st(k,:)=ifft(ss(k,:),NP);
114       figure(3*k+1);
115
116   time=tt(1:NP/2+1);
117   stress=st(k,1:NP/2+1);
118
119       plot(time*10^9,stress*10^-6,'-b','LineWidth',2)
120
121       grid on;
122       xlim([0 10^9*T/2])
123       xlabel('Time(\mus)','fontsize',16,'fontweight','bold');
124       set(gca,'fontsize',16,'fontweight','bold')
125       if k==1
126       ylabel('Stress at glass surface (MPa)');
127       elseif k==2
128       ylabel('Stress glass/water interface (MPa)');
129       elseif k==3
130       title('Water/Biofilm','Fontsize',16,'fontweight','bold');
131       ylabel('Stress(MPa)');
132       elseif k==4
```

```matlab
133     ylabel('Stress(MPa)','fontsize',16,'fontweight','bold');
134     title('Stress at Biofilm/Polystyrene Interface ...
            (MPa)','Fontsize',16,'fontweight','bold');
135     elseif k==5
136     ylabel('Stress at Polystyrene/Water Reservoir Interface (MPa)');
137     elseif k==6
138     ylabel('Stress at bottom of Water Reservoir surface (MPa)');
139     end
140
141 end
142 toc;
143 % close all;
144 ptf=0;
145 ca = 'brgcmyk';
146 sa = 'so';
147 FS=24; % Fontsize
148
149 %%%%%%%%%%%%%%%%%%%%%%%%%%%%%%%%%%%%%%%%
150 % INPUT STRESS
151 figure;
152 hold on;
153 time1=tt(1:NP/2+1);
154 stress1=st(1,1:NP/2+1);
155 plot(time1*10^9,stress1*10^-6,'b-','Linewidth',2);
156 xlabel('Time [ns]','fontsize',FS,'fontweight','bold');
157 ylabel('Stress [MPa]','fontsize',FS,'fontweight','bold');
158 % title('Input Stress Profile for ...
        Glass/Ti','fontsize',FS,'fontweight','bold');
159 set(gca,'fontsize',FS,'fontweight','bold');grid on;
160 grid minor;
161 xlim([0 80]);
162 ylim([-400 10]);
163 hold off;
164 if(ptf);print('-dpng',['inputstress_1.png']);close all;end
165 %%%%%%%%%%%%%%%%%%%%%
166 %% Stress History at Biofilm /Polystyrene Interface
```

```matlab
167  figure;
168  hold on;
169  time1=tt(1:NP/2+1);
170  stress1=st(4,1:NP/2+1);
171  plot(time1*10^9,stress1*10^-6,'b-','Linewidth',2);
172  xlabel('Time [ns]','fontsize',FS,'fontweight','bold');
173  ylabel('Stress [MPa]','fontsize',FS,'fontweight','bold');
174  % title('Input Stress Profile for ...
         Glass/Ti','fontsize',FS,'fontweight','bold');
175  set(gca,'fontsize',FS,'fontweight','bold');grid on;
176  grid minor;
177  ylim([-100 40]);
178  hold off;
179
180  if(ptf);print('-dpng',['biofilm_polystyrene_interface_stress.png']);
181  close all;end
182  %%%%%%%%%%%%%%%%%%%%%%%%%%%%%%%%%%%%%%%%%%%%%
183  %%%%%%%%%%%%%%%%%%%%%%%%%%%%%%%%%%%%%%%%%%%%%
```

References

[1] A. Cense, E. Peeters, B. Gottenbos, F. Baaijens, A. Nuijs, and M. van Dongen, "Mechanical properties and failure of streptococcus mutans biofilms, studied using a microindentation device," *Journal of Microbiological Methods*, vol. 67, no. 3, pp. 463 – 472, 2006.

[2] J. W. Costerton, K. J. Cheng, G. G. Geesey, T. I. Ladd, J. C. Nickel, M. Dasgupta, and T. J. Marrie, "Bacterial biofilms in nature and disease," *Annual Review of Microbiology*, vol. 41, no. 1, pp. 435–464, 1987.

[3] J. W. Costerton, Z. Lewandowski, D. E. Caldwell, D. R. Korber, and H. M. Lappin-Scott, "Microbial biofilms," *Annual Review of Microbiology*, vol. 49, no. 1, pp. 711–745, 1995.

[4] R. M. Donlan, "Biofilms: microbial life on surfaces.," *Emerg Infect Dis*, vol. 8, pp. 881–890, Sep 2002.

[5] D. Lopez, H. Vlamakis, and R. Kolter, "Biofilms," *Cold Spring Harbor Perspectives in Biology*, vol. 2, no. 7, 2010.

[6] L. Hall-Stoodley and P. Stoodley, "Evolving concepts in biofilm infections," *Cellular Microbiology*, vol. 11, no. 7, pp. 1034–1043, 2009.

[7] L. Hall-Stoodley, J. W. Costerton, and P. Stoodley, "Bacterial biofilms: from the natural environment to infectious diseases.," *Nat Rev Microbiol*, vol. 2, pp. 95–108, Feb 2004.

[8] R. M. Donlan, "Biofilms on central venous catheters: is eradication possible?," *Curr Top Microbiol Immunol*, vol. 322, pp. 133–161, 2008.

[9] J. K. Hatt and P. N. Rather, "Role of bacterial biofilms in urinary tract infections.," *Curr Top Microbiol Immunol*, vol. 322, pp. 163–192, 2008.

[10] M. R. Leonardo, M. A. Rossi, L. A. Silva, I. Y. Ito, and K. C. Bonifcio, "Em evaluation of bacterial biofilm and microorganisms on the apical external root surface of human teeth," *Journal of Endodontics*, vol. 28, pp. 815–818, Dec. 2002.

[11] C. K. Hope and T. R. Bott, "Laboratory modelling of manganese biofiltration using biofilms of leptothrix discophora.," *Water Res*, vol. 38, pp. 1853–1861, Apr 2004.

[12] C. R. de Carvalho, "Biofilms: recent developments on an old battle.," *Recent Pat Biotechnol*, vol. 1, no. 1, pp. 49–57, 2007.

[13] T. F. Mah and G. A. O'Toole, "Mechanisms of biofilm resistance to antimicrobial agents.," *Trends Microbiol*, vol. 9, pp. 34–39, Jan 2001.

[14] G. G. Anderson and G. A. O'Toole, "Innate and induced resistance mechanisms of bacterial biofilms.," *Curr Top Microbiol Immunol*, vol. 322, pp. 85–105, 2008.

[15] K. Lewis, "Persister cells and the riddle of biofilm survival.," *Biochemistry (Mosc)*, vol. 70, pp. 267–274, Feb 2005.

[16] M. Potts, "Desiccation tolerance of prokaryotes.," *Microbiol Rev*, vol. 58, pp. 755–805, Dec 1994.

[17] I. W. Sutherland, "Biofilm exopolysaccharides: a strong and sticky framework," *Microbiology*, vol. 147, no. 1, pp. 3–9, 2001.

[18] H. C. Flemming and J. Wingender, "The biofilm matrix.," *Nat Rev Microbiol*, vol. 8, pp. 623–633, Sep 2010.

[19] J. W. Jana Jass, Susanne Surman, ed., *Medical Biofilms: Detection, Prevention, and Control.* Wiley, 1st ed., 2003.

[20] C. E. Edmiston, G. R. Seabrook, M. P. Goheen, C. J. Krepel, C. P. Johnson, B. D. Lewis, K. R. Brown, and J. B. Towne, "Bacterial adherence to surgical sutures: Can antibacterial-coated sutures reduce the risk of microbial contamination?," *Journal of the American College of Surgeons*, vol. 203, pp. 481–489, Oct. 2006.

[21] Y. Mu, J. R. Edwards, T. C. Horan, S. I. Berrios-Torres, and S. K. Fridkin, "Improving risk-adjusted measures of surgical site infection for the national healthcare safety network.," *Infect Control Hosp Epidemiol*, vol. 32, pp. 970–986, Oct 2011.

[22] P. S. Stewart and J. William Costerton, "Antibiotic resistance of bacteria in biofilms," *The Lancet*, vol. 358, pp. 135–138, July 2001.

[23] A. Khoury, K. Lam, B. Ellis, and J. Costerton, "Prevention and control of bacterial infections associated with medical devices.," *ASAIO J*, vol. 38, no. 3, pp. M174–8–, 1992.

[24] H. W. Boucher, G. H. Talbot, J. S. Bradley, J. E. Edwards, D. Gilbert, L. B. Rice, M. Scheld, B. Spellberg, and J. Bartlett, "Bad bugs, no drugs: no escape! an update from the infectious diseases society of america.," *Clin Infect Dis*, vol. 48, pp. 1–12, Jan 2009.

[25] M. E. Jones, J. A. Karlowsky, D. C. Draghi, C. Thornsberry, D. F. Sahm, and D. Nathwani, "Epidemiology and antibiotic susceptibility of bacteria causing skin and soft tissue infections in the usa and europe: a guide to appropriate antimicrobial therapy.," *Int J Antimicrob Agents*, vol. 22, pp. 406–419, Oct 2003.

[26] D. M. Livermore, "Introduction: the challenge of multiresistance.," *Int J Antimicrob Agents*, vol. 29 Suppl 3, pp. S1–S7, May 2007.

[27] R. N. Jones, "Resistance patterns among nosocomial pathogens: trends over the past few years.," *Chest*, vol. 119, pp. 397S–404S, Feb 2001.

[28] D. L. Paterson, "Resistance in gram-negative bacteria: Enterobacteriaceae.," *Am J Infect Control*, vol. 34, pp. S20–8; discussion S64–73, Jun 2006.

[29] L. B. Rice, "Antimicrobial resistance in gram-positive bacteria.," *Am J Med*, vol. 119, pp. S11–9; discussion S62–70, Jun 2006.

[30] B. Spellberg, R. Guidos, D. Gilbert, J. Bradley, H. W. Boucher, W. M. Scheld, J. G. Bartlett, J. Edwards, Jr, and I. D. S. o. A. , "The epidemic of antibiotic-resistant infections: a call to action for the medical community from the infectious diseases society of america.," *Clin Infect Dis*, vol. 46, pp. 155–164, Jan 2008.

[31] K. N. Cowan, L. Teague, S. C. Sue, and J. L. Mahoney, "Vacuum-assisted wound closure of deep sternal infections in high-risk patients after cardiac surgery.," *Ann Thorac Surg*, vol. 80, pp. 2205–2212, Dec 2005.

[32] J. Sjogren, R. Gustafsson, J. Nilsson, M. Malmsjo, and R. Ingemansson, "Clinical outcome after poststernotomy mediastinitis: vacuum-assisted closure versus conventional treatment.," *Ann Thorac Surg*, vol. 79, pp. 2049–2055, Jun 2005.

[33] A. A. Mehbod, J. W. Ogilvie, M. R. Pinto, J. D. Schwender, E. E. Transfeldt, K. B. Wood, J. C. Le Huec, and T. Dressel, "Postoperative deep wound infections in adults after spinal fusion: management with vacuum-assisted wound closure.," *J Spinal Disord Tech*, vol. 18, pp. 14–17, Feb 2005.

[34] B. E. Leininger, T. E. Rasmussen, D. L. Smith, D. H. Jenkins, and C. Coppola, "Experience with wound vac and delayed primary closure of contaminated soft tissue injuries in iraq.," *J Trauma*, vol. 61, pp. 1207–1211, Nov 2006.

[35] L. C. Argenta and M. J. Morykwas, "Vacuum-assisted closure: a new method for wound control and treatment: clinical experience.," *Ann Plast Surg*, vol. 38, pp. 563–76; discussion 577, Jun 1997.

[36] J. O. Kucan, M. C. Robson, J. P. Heggers, and F. Ko, "Comparison of silver sulfadiazine, povidone-iodine and physiologic saline in the treatment of chronic pressure ulcers.," *J Am Geriatr Soc*, vol. 29, pp. 232–235, May 1981.

[37] T. Bjarnsholt and M. Givskov, "Quorum-sensing blockade as a strategy for enhancing host defences against bacterial pathogens.," *Philos Trans R Soc Lond B Biol Sci*, vol. 362, pp. 1213–1222, Jul 2007.

[38] M. Habash and G. Reid, "Microbial biofilms: their development and significance for medical device-related infections.," *J Clin Pharmacol*, vol. 39, pp. 887–898, Sep 1999.

[39] A. G. Chiu, M. B. Antunes, J. N. Palmer, and N. A. Cohen, "Evaluation of the in vivo efficacy of topical tobramycin against pseudomonas sinonasal biofilms.," *J Antimicrob Chemother*, vol. 59, pp. 1130–1134, Jun 2007.

[40] K. S. Oxley, J. G. Thomas, and H. H. Ramadan, "Effect of ototopical medications on tympanostomy tube biofilms.," *Laryngoscope*, vol. 117, pp. 1819–1824, Oct 2007.

[41] M. Desrosiers, Z. Bendouah, and J. Barbeau, "Effectiveness of topical antibiotics on staphylococcus aureus biofilm in vitro.," *Am J Rhinol*, vol. 21, no. 2, pp. 149–153, 2007.

[42] M. Y. Desrosiers and M. Salas-Prato, "Treatment of chronic rhinosinusitis refractory to other treatments with topical antibiotic therapy delivered by means of a large-particle nebulizer: results of a controlled trial.," *Otolaryngol Head Neck Surg*, vol. 125, pp. 265–269, Sep 2001.

[43] M. Desrosiers, M. Myntti, and G. James, "Methods for removing bacterial biofilms: in vitro study using clinical chronic rhinosinusitis specimens.," *Am J Rhinol*, vol. 21, no. 5, pp. 527–532, 2007.

[44] T. Weed, C. Ratliff, and D. B. Drake, "Quantifying bacterial bioburden during negative pressure wound therapy: does the wound vac enhance bacterial clearance?," *Ann Plast Surg*, vol. 52, pp. 276–9; discussion 279–80, Mar 2004.

[45] A. Braakenburg, M. C. Obdeijn, R. Feitz, I. A. L. M. van Rooij, A. J. van Griethuysen, and J. H. G. Klinkenbijl, "The clinical efficacy and cost effectiveness of the vacuum-assisted closure technique in the management of acute and chronic wounds: a randomized controlled trial.," *Plast Reconstr Surg*, vol. 118, pp. 390–7; discussion 398–400, Aug 2006.

[46] C. Moues, G. van den Bemd, F. Heule, and S. Hovius, "Comparing conventional gauze therapy to vacuum-assisted closure wound therapy: A prospective randomised trial," *Journal of Plastic, Reconstructive & Aesthetic Surgery*, vol. 60, pp. 672–681, June 2007.

[47] C. M. Mous, F. Heule, and S. E. R. Hovius, "A review of topical negative pressure therapy in wound healing: sufficient evidence?," *Am J Surg*, vol. 201, pp. 544–556, Apr 2011.

[48] M. A. Dinno, M. Dyson, S. R. Young, A. J. Mortimer, J. Hart, and L. A. Crum, "The significance of membrane changes in the safe and effective use of therapeutic and diagnostic ultrasound.," *Phys Med Biol*, vol. 34, pp. 1543–1552, Nov 1989.

[49] S. R. Young and M. Dyson, "The effect of therapeutic ultrasound on angiogenesis.," *Ultrasound Med Biol*, vol. 16, no. 3, pp. 261–269, 1990.

[50] P. Reher, M. Harris, M. Whiteman, H. K. Hai, and S. Meghji, "Ultrasound stimulates nitric oxide and prostaglandin e2 production by human osteoblasts.," *Bone*, vol. 31, pp. 236–241, Jul 2002.

[51] W. J. Ennis, P. Foremann, N. Mozen, J. Massey, T. Conner-Kerr, and P. Meneses, "Ultrasound therapy for recalcitrant diabetic foot ulcers: results of a randomized, double-blind, controlled, multicenter study.," *Ostomy Wound Manage*, vol. 51, pp. 24–39, Aug 2005.

[52] W. G. Pitt and S. A. Ross, "Ultrasound increases the rate of bacterial cell growth.," *Biotechnol Prog*, vol. 19, no. 3, pp. 1038–1044, 2003.

[53] J. C. Carmen, B. L. Roeder, J. L. Nelson, B. L. Beckstead, C. M. Runyan, G. B. Schaalje, R. A. Robison, and W. G. Pitt, "Ultrasonically enhanced vancomycin activity against staphylococcus epidermidis biofilms in vivo.," *J Biomater Appl*, vol. 18, pp. 237–245, Apr 2004.

[54] Z. Qian, P. Stoodley, and W. G. Pitt, "Effect of low-intensity ultrasound upon biofilm structure from confocal scanning laser microscopy observation.," *Biomaterials*, vol. 17, pp. 1975–1980, Oct 1996.

[55] R. Gerber, U. Studer, and H. Danuser, "Is newer always better? a comparative study of 3 lithotriptor generations," *The Journal of Urology*, vol. 173, no. 6, pp. 2013 – 2016, 2005.

[56] K. F. Novak, M. Govindaswami, J. L. Ebersole, W. Schaden, N. House, and M. J. Novak, "Effects of low-energy shock waves on oral bacteria.," *J Dent Res*, vol. 87, pp. 928–931, Oct 2008.

[57] G. Delacretaz, K. Rink, G. Pittomvils, J. Lafaut, H. Vandeursen, and R. Boving, "Importance of the implosion of eswl-induced cavitation bubbles," *Ultrasound in Medicine & Biology*, vol. 21, no. 1, pp. 97 – 103, 1995.

[58] L. Wang, L. Qin, H. Lu, W. Cheung, H. Yang, W. Wong, K. Chan, and K. Leung, "Extracorporeal shock wave therapy in treatment of delayed bone-tendon healing," *The American Journal of Sports Medicine*, vol. 36, no. 2, pp. 340–347, 2008.

[59] Y. Kuo, C.-T. Wang, F. Wang, K. D. Yang, Y. Chiang, and C. Wang, "Extracorporeal shock wave treatment modulates skin fibroblast recruitment and leukocyte infiltration for enhancing extended skin-flap survival," *Wound Repair and Regeneration*, vol. 17, no. 1, pp. 80–87, 2009.

[60] W. Schaden, A. Fischer, and A. Sailler, "Extracorporeal shock wave therapy of nonunion or delayed osseous union.," *Clin Orthop Relat Res*, pp. 90–94, Jun 2001.

[61] T. Nishida, H. Shimokawa, K. Oi, H. Tatewaki, T. Uwatoku, K. Abe, Y. Matsumoto, N. Kajihara, M. Eto, T. Matsuda, H. Yasui, A. Takeshita, and K. Sunagawa, "Extracorporeal cardiac shock wave therapy markedly ameliorates ischemia-induced myocardial dysfunction in pigs in vivo," *Circulation*, vol. 110, no. 19, pp. 3055–3061, 2004.

[62] R. Meirer, F. S. Kamelger, G. M. Huemer, S. Wanner, and H. Piza-Katzer, "Extracorporal shock wave may enhance skin flap survival in an animal model.," *Br J Plast Surg*, vol. 58, pp. 53–57, Jan 2005.

[63] G. Haupt and M. Chvapil, "Effect of shock waves on the healing of partial-thickness wounds in piglets," *Journal of Surgical Research*, vol. 49, no. 1, pp. 45 – 48, 1990.

[64] L. Gerdesmeyer, C. von Eiff, C. Horn, M. Henne, M. Roessner, P. Diehl, and H. Gollwitzer, "Antibacterial effects of extracorporeal shock waves.," *Ultrasound Med Biol*, vol. 31, pp. 115–119, Jan 2005.

[65] W. Kerfoot, A. Beshai, and C. Carson, "The effect of isolated high-energy shock wave treatments on subsequent bacterial growth," *Urological Research*, vol. 20, pp. 183–186, 1992. 10.1007/BF00296536.

[66] S. Sathishkumar, A. Meka, D. Dawson, N. House, W. Schaden, M. Novak, J. L. Ebersole, and L. Kesavalu, "Extracorporeal shock wave therapy induces alveolar bone regeneration," *Journal of Dental Research*, vol. 87, no. 7, pp. 687–691, 2008.

[67] H. Gollwitzer, C. Horn, C. Von Eiff, M. Henne, and L. Gerdesmeyer, "Antibacterial effectiveness of high-energetic extracorporeal shock waves: an in vitro verification.," *Z Orthop Ihre Grenzgeb*, vol. 142, no. 4, pp. 462–466, 2004.

[68] P. Mller, B. Guggenheim, T. Attin, E. Marlinghaus, and P. R. Schmidlin, "Potential of shock waves to remove calculus and biofilm.," *Clin Oral Investig*, vol. 15, pp. 959–965, Dec 2011.

[69] J. M. Dodick and J. Christiansen, "Experimental studies on the development and propagation of shock waves created by the interaction of short nd:yag laser pulses with a titanium target. possible implications for nd:yag laser phacolysis of the cataractous human lens.," *J Cataract Refract Surg*, vol. 17, pp. 794–797, Nov 1991.

[70] E. Alzner and G. Grabner, "Dodick laser phacolysis: thermal effects.," *J Cataract Refract Surg*, vol. 25, pp. 800–803, Jun 1999.

[71] S. Lee, D. McAuliffe, H. Zhang, Z. Xu, J. Taitelbaum, T. Flotte, and A. Doukas, "Stress-wave-induced membrane permeation of red blood cells is facilitated by aquaporins," *Ultrasound in Medicine & Biology*, vol. 23, no. 7, pp. 1089 – 1094, 1997.

[72] M. Terakawa, M. Ogura, S. Sato, H. Wakisaka, H. Ashida, M. Uenoyama, Y. Masaki, and M. Obara, "Gene transfer into mammalian cells by use of a nanosecond pulsed laser-inducedstress wave," *Opt. Lett.*, vol. 29, pp. 1227–1229, Jun 2004.

[73] M. Ogura, S. Sato, K. Nakanishi, M. Uenoyama, T. Kiyozumi, D. Saitoh, T. Ikeda, H. Ashida, and M. Obara, "In vivo targeted gene transfer in skin by the use of laser-induced stress waves," *Lasers in Surgery and Medicine*, vol. 34, no. 3, pp. 242–248, 2004.

[74] S. Lee, D. J. McAuliffe, T. J. Flotte, N. Kollias, and A. G. Doukas, "Photomechanical transcutaneous delivery of macromolecules1," vol. 111, pp. 925–929, Dec. 1998.

[75] N. S. Soukos, S. S. Socransky, S. E. Mulholland, S. Lee, and A. G. Doukas, "Photomechanical drug delivery into bacterial biofilms.," *Pharm Res*, vol. 17, pp. 405–409, Apr 2000.

[76] N. S. Soukos, S. E. Mulholland, S. S. Socransky, and A. G. Doukas, "Photodestruction of human dental plaque bacteria: enhancement of the photodynamic effect by photomechanical waves in an oral biofilm model.," *Lasers Surg Med*, vol. 33, no. 3, pp. 161–168, 2003.

[77] M. Ogura, A. Abernethy, R. Blissett, K. Ruggiero, S. Som, J. Goodson, R. Kent, A. Doukas, and N. Soukos, "Photomechanical wave-assisted molecular delivery in oral biofilms," *World Journal of Microbiology and Biotechnology*, vol. 23, pp. 1637–1646, 2007. 10.1007/s11274-007-9411-x.

[78] A. G. Doukas, "Laser-generated stress waves in medicine: From tissue injury to drug delivery," in *Biomedical Optical Spectroscopy and Diagnostics / Therapeutic Laser Applications*, p. TMB2, Optical Society of America, 1998.

[79] Y. P. Krespi, P. Stoodley, and L. Hall-Stoodley, "Laser disruption of biofilm.," *Laryngoscope*, vol. 118, pp. 1168–1173, Jul 2008.

[80] V. Kizhner, Y. P. Krespi, L. Hall-Stoodley, and P. Stoodley, "Laser-generated shockwave for clearing medical device biofilms.," *Photomed Laser Surg*, vol. 29, pp. 277–282, Apr 2011.

[81] Y. P. Krespi, V. Kizhner, L. Nistico, L. Hall-Stoodley, and P. Stoodley, "Laser disruption and killing of methicillin-resistant staphylococcus aureus biofilms," *American Journal of Otolaryngology*, vol. 32, no. 3, pp. 198 – 202, 2011.

[82] S. Wanner, M. Gstttner, R. Meirer, J. Hausdorfer, M. Fille, and B. Stckl, "Low-energy shock waves enhance the susceptibility of staphylococcal biofilms to antimicrobial agents in vitro," *Journal of Bone & Joint Surgery, British Volume*, vol. 93-B, no. 6, pp. 824–827, 2011.

[83] G. R. Nigri, S. Tsai, S. Kossodo, P. Waterman, P. Fungaloi, D. C. Hooper, A. G. Doukas, and G. M. LaMuraglia, "Laser-induced shock waves enhance sterilization of infected vascular prosthetic grafts," *Lasers in Surgery and Medicine*, vol. 29, no. 5, pp. 448–454, 2001.

[84] E. Hagerman, J. Shim, V. Gupta, and B. Wu, "Evaluation of laser spallation as a technique for measurement of cell adhesion strength," *Journal of Biomedical Materials Research Part A*, vol. 82A, no. 4, pp. 852–860, 2007.

[85] J. Shim, E. Hagerman, B. Wu, and V. Gupta, "Measurement of the tensile strength of cellularbiomaterial interface using the laser spallation technique," *Acta Biomaterialia*, vol. 4, no. 6, pp. 1657 – 1668, 2008.

[86] J. N. Wilking, T. E. Angelini, A. Seminara, M. P. Brenner, and D. A. Weitz, "Biofilms as complex fluids," *MRS Bulletin*, vol. 36, no. 05, pp. 385–391, 2011.

[87] N. Aravas and C. Laspidou, "On the calculation of the elastic modulus of a biofilm streamer," *Biotechnology and Bioengineering*, vol. 101, no. 1, pp. 196–200, 2008.

[88] A. M. Vinogradov, M. Winston, C. J. Rupp, and P. Stoodley, "Rheology of biofilms formed from the dental plaque pathogen streptococcus mutans," *Biofilms*, vol. 1, pp. 49–56, 0 2004.

[89] T. Shaw, M. Winston, C. J. Rupp, I. Klapper, and P. Stoodley, "Commonality of elastic relaxation times in biofilms.," *Phys Rev Lett*, vol. 93, p. 098102, Aug 2004.

[90] J. Kreth, E. Hagerman, K. Tam, J. Merritt, D. T. W. Wong, B. M. Wu, N. V. Myung, W. Shi, and F. Qi, "Quantitative analyses of streptococcus mutans biofilms with quartz crystal microbalance, microjet impingement and confocal microscopy," *Biofilms*, vol. 1, no. 04, pp. 277–284 M3 – 10.1017/S1479050504001516, 2004.

[91] S. Bayoudh, L. Ponsonnet, H. B. Ouada, A. Bakhrouf, and A. Othmane, "Bacterial detachment from hydrophilic and hydrophobic surfaces using a microjet impingement," *Colloids and Surfaces A: Physicochemical and Engineering Aspects*, vol. 266, pp. 160–167, Sept. 2005.

[92] R. Richards, I. ap Gwynn, K. J. Bundy, and B. A. Rahn, "Microjet impingement followed by scanning electron microscopy as a qualitative technique to compare cellular adhesion to various biomaterials," *Cell Biology International*, vol. 19, pp. 1015–1024, Dec. 1995.

[93] P. Stoodley, Z. Lewandowski, J. D. Boyle, and H. M. Lappin-Scott, "Structural deformation of bacterial biofilms caused by short-term fluctuations in fluid shear: an in situ investigation of biofilm rheology.," *Biotechnol Bioeng*, vol. 65, pp. 83–92, Oct 1999.

[94] I. Klapper, C. J. Rupp, R. Cargo, B. Purvedorj, and P. Stoodley, "Viscoelastic fluid description of bacterial biofilm material properties.," *Biotechnol Bioeng*, vol. 80, pp. 289–296, Nov 2002.

[95] B. W. Towler, C. J. Rupp, A. B. Cunningham, and P. Stoodley, "Viscoelastic properties of a mixed culture biofilm from rheometer creep analysis.," *Biofouling*, vol. 19, pp. 279–285, Oct 2003.

[96] V. Korstgens, H. C. Flemming, J. Wingender, and W. Borchard, "Uniaxial compression measurement device for investigation of the mechanical stability of biofilms.," *J Microbiol Methods*, vol. 46, pp. 9–17, Jul 2001.

[97] S. Aggarwal and R. M. Hozalski, "Effect of strain rate on the mechanical properties of staphylococcus epidermidis biofilms," *Langmuir*, vol. 28, no. 5, pp. 2812–2816, 2012.

[98] V. Gupta, A. Argon, J. Cornie, and D. Parks, "Measurement of interface strength by laser-pulse-induced spallation," *Materials Science and Engineering: A*, vol. 126, no. 1-2, pp. 105 – 117, 1990.

[99] V. Gupta, A. Argon, D. Parks, and J. Cornie, "Measurement of interface strength by a laser spallation technique," *Journal of the Mechanics and Physics of Solids*, vol. 40, no. 1, pp. 141 – 180, 1992.

[100] J. Yuan and V. Gupta, "Measurement of interface strength by the modified laser spallation technique. i. experiment and simulation of the spallation process," *Journal of Applied Physics*, vol. 74, no. 4, pp. 2388–2396, 1993.

[101] V. Gupta and J. Yuan, "Measurement of interface strength by the modified laser spallation technique. ii. applications to metal/ceramic interfaces," *Journal of Applied Physics*, vol. 74, no. 4, pp. 2397–2404, 1993.

[102] J. Yuan, V. Gupta, and A. Pronin, "Measurement of interface strength by the modified laser spallation technique. iii. experimental optimization of the stress pulse," *Journal of Applied Physics*, vol. 74, no. 4, pp. 2405–2410, 1993.

[103] V. Gupta, J. Yuan, and A. Pronin, "Recent developments in the laser spallation technique to measure the interface strength and its relationship to interface toughness with applications to metal/ceramic, ceramic/ceramic and ceramic/polymer interfaces," *Journal of Adhesion Science and Technology*, vol. 8, no. 6, pp. 713–747, 1994.

[104] J. Yuan and V. Gupta, "The effect of microstructure and chemistry on the tensile strength of nb/sapphire interfaces with and without interlayers of sb and cr," *Acta Metallurgica et Materialia*, vol. 43, no. 2, pp. 781 – 794, 1995.

[105] J. Yuan, V. Gupta, and M. Kim, "Structure and chemistry of nb/sapphire interfaces, with and without interlayers of sb and cr," *Acta Metallurgica et Materialia*, vol. 43, no. 2, pp. 769 – 779, 1995.

[106] V. Gupta, J. Wu, and A. N. Pronin, "Effect of substrate orientation, roughness, and film deposition mode on the tensile strength and toughness of niobium-sapphire interfaces," *Journal of the American Ceramic Society*, vol. 80, no. 12, pp. 3172–3180, 1997.

[107] V. Gupta, V. Kireev, J. Tian, H. Yoshida, and H. Akahoshi, "Glass-modified stress waves for adhesion measurement of ultra thin films for device applications," *Journal of the Mechanics and Physics of Solids*, vol. 51, no. 8, pp. 1395 – 1412, 2003.

[108] M. Niinomi, "Mechanical properties of biomedical titanium alloys," *Materials Science and Engineering: A*, vol. 243, no. 12, pp. 231 – 236, 1998.

[109] J. Shim, *The Laser Spallation Technique for measurement of tensile strength of cell/tissue-biomaterial interface and its applications*. PhD thesis, University of California, Los Angeles, 2005.

[110] R. J. Gordon, M. Miragaia, A. D. Weinberg, C. J. Lee, J. Rolo, J. C. Giacalone, M. S. Slaughter, P. Pappas, Y. Naka, A. J. Tector, H. de Lencastre, and F. D. Lowy, "Staphylococcus epidermidis colonization is highly clonal across us cardiac centers," *Journal of Infectious Diseases*, vol. 205, no. 9, pp. 1391–1398, 2012.

[111] V. M. HOl V., Ruzicka F., "The dynamics of staphylococcus epidermis biofilm formation in relation to nutrition, temperature, and time," *Scripta Medica Facultatis Medicae Universitatis Brunensis Masarykianae*, vol. 79, no. 3, pp. 169–174, 2006.

[112] Y. H. An and R. J. Friedman, "Laboratory methods for studies of bacterial adhesion," *Journal of Microbiological Methods*, vol. 30, no. 2, pp. 141 – 152, 1997.

[113] J. Rayner, R. Veeh, and J. Flood, "Prevalence of microbial biofilms on selected fresh produce and household surfaces," *International Journal of Food Microbiology*, vol. 95, no. 1, pp. 29 – 39, 2004.

[114] H. Kim, *In-Situ Measurement of Intrinsic Interface strength and Moisture-Effected Interfacial Fracture Energy*. PhD thesis, University of California, Los Angeles, 2008.

[115] M. Tsezos and A. Benedek, "A method for the calculation of biological film volume in a fluidized bed biological reactor," *Water Research*, vol. 14, no. 6, pp. 689–693, 1980.

[116] S. W. Hermanowicz and J. J. Ganczarczyk, "Some fluidization characteristics of biological beds.," *Biotechnol Bioeng*, vol. 25, pp. 1321–1330, May 1983.

[117] H. Shemesh, D. E. Goertz, L. W. M. van der Sluis, N. de Jong, M. K. Wu, and P. R. Wesselink, "High frequency ultrasound imaging of a single-species biofilm.," *J Dent*, vol. 35, pp. 673–678, Aug 2007.

[118] A. Heydorn, A. T. Nielsen, M. Hentzer, C. Sternberg, M. Givskov, B. K. Ersbll, and S. Molin, "Quantification of biofilm structures by the novel computer program comstat.," *Microbiology*, vol. 146 (Pt 10), pp. 2395–2407, Oct 2000.

[119] A. G. Doukas, D. J. McAuliffe, and T. J. Flotte, "Biological effects of laser-induced shock waves: Structural and functional cell damage in vitro," *Ultrasound Med Biol*, vol. 19, pp. 137–146, Jan. 1993.

[120] A. Vogel, S. Busch, and U. Parlitz, "Shock wave emission and cavitation bubble generation by picosecond and nanosecond optical breakdown in water," *The Journal of the Acoustical Society of America*, vol. 100, no. 1, pp. 148–165, 1996.

[121] J. Shim, E. Hagerman, B. Wu, and V. Gupta, "Measurement of the tensile strength of cell-biomaterial interface using the laser spallation technique," *Acta Biomaterialia*, vol. 4, no. 6, pp. 1657 – 1668, 2008.

[122] J. Shim, H. Nakamura, T. Ogawa, and V. Gupta, "An understanding of the mechanism that promotes adhesion between roughened titanium implants and mineralized tissue," *Journal of Biomechanical Engineering*, vol. 131, no. 5, p. 054503, 2009.

[123] A. G. Doukas and N. Kollias, "Transdermal drug delivery with a pressure wave.," *Adv Drug Deliv Rev*, vol. 56, pp. 559–579, Mar 2004.

[124] T. P. Sullivan, W. H. Eaglstein, S. C. Davis, and P. Mertz, "The pig as a model for human wound healing.," *Wound Repair Regen*, vol. 9, no. 2, pp. 66–76, 2001.

[125] M. M. Swindle and A. Smith, "Comparative anatomy and physiology of the pig," *Scand J Lab Anim Sci*, vol. 25, no. Suppl 1, pp. 1–10, 1998.

[126] R. Kong and R. Bhargava, "Characterization of porcine skin as a model for human skin studies using infrared spectroscopic imaging," *Analyst*, vol. 136, no. 11, pp. 2359–2366, 2011.

[127] M. Clinic, "Basic layers of the skin." http://www.mayoclinic.com/.

[128] J. Lim, J. Hong, W. W. Chen, and T. Weerasooriya, "Mechanical response of pig skin under dynamic tensile loading," *International Journal of Impact Engineering*, vol. 38, pp. 130–135, Feb. 2011.

[129] O. A. Shergold, N. A. Fleck, and D. Radford, "The uniaxial stress versus strain response of pig skin and silicone rubber at low and high strain rates," *International Journal of Impact Engineering*, vol. 32, pp. 1384–1402, Sept. 2006.

[130] A. Kim, *In-Situ Measurement of Intrinsic Interface strength and Moisture-Effected Interfacial Fracture Energy*. PhD thesis, University of California, Los Angeles, 2008.

[131] C. Kuhn, F. Angehrn, O. Sonnabend, and A. Voss, "Impact of extracorporeal shock waves on the human skin with cellulite: a case study of an unique instance.," *Clin Interv Aging*, vol. 3, no. 1, pp. 201–210, 2008.

[132] S. Lee, N. Kollias, D. J. McAuliffe, T. J. Flotte, and A. G. Doukas, "Topical drug delivery in humans with a single photomechanical wave.," *Pharm Res*, vol. 16, pp. 1717–1721, Nov 1999.

[133] M. Vollmer and K.-P. Mllmann, "High speed and slow motion: the technology of modern high speed cameras," *Physics Education*, vol. 46, no. 2, p. 191, 2011.

[134] C. Willert, B. Stasicki, J. Klinner, and S. Moessner, "Pulsed operation of high-power light emitting diodes for imaging flow velocimetry," *Measurement Science and Technology*, vol. 21, no. 7, p. 075402, 2010.

[135] F. Y. Testik, A. P. Barros, and L. F. Bliven, "Field observations of multimode raindrop oscillations by high-speed imaging," *J. Atmos. Sci.*, vol. 63, pp. 2663–2668, Oct. 2006.

[136] A. Whybrew, *Handbook of Laser Technology and Applications: Applications*, vol. 3. London: Institute of Physics Publishing, 2004.

[137] W. Hiller, H. M. Lent, G. E. A. Meier, and B. Stasicki, "A pulsed light generator for high speed photography," *Experiments in Fluids*, vol. 5, pp. 141–144, Mar. 1987.

[138] A. Brandorff and J. W. Sussmeier, "Method and apparatus for illumination and imaging of a surface using 2-d led array," 1995. Patent.

[139] M. Yuyama and Y. Kato, "Illumination apparatus, imaging apparatus and irradiation method for an imaging apparatus comprising light emitting diodes which are duty-driven during an imaging period of a frame period," June 2010.

[140] Y. A. Pishchalnikov, O. A. Sapozhnikov, M. R. Bailey, J. C. Williams, Jr, R. O. Cleveland, T. Colonius, L. A. Crum, A. P. Evan, and J. A. McAteer, "Cavitation bubble cluster activity in the breakage of kidney stones by lithotripter shockwaves.," *J Endourol*, vol. 17, pp. 435–446, Sep 2003.

[141] Z. Xu, M. Raghavan, T. Hall, C.-W. Chang, M.-A. Mycek, J. Fowlkes, and C. Cain, "High speed imaging of bubble clouds generated in pulsed ultrasound cavitational therapy - histotripsy," *Ultrasonics, Ferroelectrics and Frequency Control, IEEE Transactions on*, vol. 54, pp. 2091 –2101, October 2007.

[142] J. G. Fujimoto, W. Z. Lin, E. P. Ippen, C. A. Puliafito, and R. F. Steinert, "Time-resolved studies of nd:yag laser-induced breakdown. plasma formation, acoustic wave generation, and cavitation.," *Invest Ophthalmol Vis Sci*, vol. 26, pp. 1771–1777, Dec 1985.

[143] A. K. Mal, S. Banerjee, and V. Gupta, "Measurement of thin film interfacial properties using nanosecond laser source," vol. 6177, p. 61770Y, SPIE, 2006.